UNIVERSITÀ DEGLI STUDI DI MILANO
FACOLTÀ DI SCIENZE AGRARIE E ALIMENTARI
Department of Food, Environmental and Nutritional Sciences (DeFENS)

Graduate School in Molecular Sciences and Plant, Food and Environmental Biotechnology

PhD programme in Food Science, Technology and Biotechnology

XXVI cycle

AN ENGINEERING APPROACH TO DESIGN FOOD STRUCTURES FOR THE DELIVERY OF TARGETED FUNCTIONALITY: APPLICATION TO BIOACTIVES ENCAPSULTION

Scientific field AGR/15

TOMMASO ROVERSI

Tutor: Prof. Laura Piazza

Co-tutor: Prof. Marisa Porrini

PhD Coordinator: Prof. Maria Grazia Fortina

2012/2013

Contents

Contents

ABSTRACT

The food industry is constantly challenged to meet consumer demands for new food products that are safe, convenient, affordable, pleasurable and healthy. An understanding of fundamental structure and function relationships of food components is a key to stimulate and accelerate the development of innovative, complex and highly structured products and suitable production processes. The goal of the Thesis is the design of health supporting food functions with development of food structure/health benefits relationships based on fundamental soft material concepts. New capsules for bioactive controlled release to be used as ingredient for new formulated foods have been designed and developed. Food material science, engineering process and soft matter's basic principles are here linked to deliver new real products that could improve health and well-being.

A first step of our research, described in *chapter 1*, was focused on the selection of the most appropriate shell material to be used in capsules manufacturing. A number of studies were performed regarding the gelation kinetics and the rheological properties of alginate, a natural biopolymer having unique properties that have enabled it to be used as a matrix for the entrapment and/or delivery of a variety of biological agents. The kinetics of alginate gelation has been investigated by means of photon correlation imaging (collaboration with POLIMI) and large deformation rheology. Our results showed that the alginate gelling kinetics displays a peculiar non-diffusive behavior, and the subsequent restructuring of the gel structure shares several features in common with the aging of colloidal gels, in particular for what concerns the occurrence of heterogeneous dynamics effects. A comparative analysis of the gel macroscopic mechanical properties at different aging stages further highlights distinctive effects arising from the non-permanent nature of the bonds.

In addition to the selection of an appropriate shell material, the challenges in developing commercially viable microcapsules rely on the selection of the most appropriate process to provide the desired morphology and stability. Thus a second step of our work, described in *chapter 2* of the thesis, was focused on the realization of a batch coaxial encapsulation unit on lab scale for the production of alginate microbeads. A dual jet of liquid core and liquid shell material was pumped through concentric extrusion nozzles and droplets were formed by jet cutting technology. The shell of the bead was then hardened in a cross-linking solution. After process optimization, microcapsules containing a liquid core of bioactive with a narrow size distribution and mean diameter of 0.73±0.03 mm were produced.

As third step (see *chapter 3*), different types of microcapsules were produced and tested for engineered release of bioactive. Alginate microspheres containing a liquid core of cyanocobalamin, in presence or not of a double coating polymer, were tested for vitamin release under simulated intestinal peristaltic flow conditions of the lumen content. The small intestine model, designed and implemented at the University of Birmingham, mimics the peristaltic flow patterns by means of a pneumatic mechanism that reproduces the characteristic segmentation movements responsible for the flow and mixing. Diffusional experiment showed a good retention of the carried vitamin under simulated intestinal condition, and an overall mass transfer was calculated. Diffusivity seems to be directly related to the wall material solubility. Microbeads containing a modified luminescent *Bifidobacterium longum* were also efficiently used to protect bacteria's vitality under simulated gastric condition.

While designing a functional ingredient, a prerequisite is that it could accomplish a specific function whilst being palatable enough to be eaten. The engineering of these properties is necessary and extremely challenging and clearly can be obtained at multiple length scales. Thus, the last research topic faced in this thesis and here reported in chapter 4 was aimed to increase knowledge on the influence of size-scale of the structures designed for bioactive release. In particular the investigation, developed in collaboration with the Food and Soft Material Group at ETH of Zurich, focused on exploring the potential of using a physical inspired (solvent shifting) production process of biopolymer-based nanoparticles. Specifically, we clearly demonstrated the possibility to produce

Abstract

nanospheres with a diameter as much as small as 20 nanometers without using any kind of mixing energy. Nanoparticles were studied by using advanced optical techniques, such as dynamic light scattering and depolarized dynamic light scattering, and finally used in preliminary experiments to increase the stability of a spontaneous food emulsion.

A main deliverable of this thesis is a contribution in increasing knowledge on the influence of structure and physical properties of food materials on the nutritional and health inducing properties, an essential step which is needed in the studies of bio-physical and gastro intestinal engineering aspects of nutrient absorption. An innovative approach has been followed that explores the relationship: material properties-processing-destructurization behavior in the gut, aimed to food properties generation, preservation and delivery. It relies on the concepts of multiscale structure dynamics and on biophysics-driven strategies for structure design.

RIASSUNTO

L'industria alimentare è costantemente stimolata ad incontrare le esigenze del consumatore, il quale richiede nuovi prodotti che siano sicuri, convenienti, piacevoli e salutari. Una maggiore comprensione della relazione fondamentale tra struttura e proprietà dell'alimento è indispensabile per stimolare e accelerare lo sviluppo di prodotti innovativi, complessi e altamente strutturati ed i loro processi di produzione. L'obiettivo di questa tesi di dottorato è la progettazione di funzionalità a sostegno della salute, da ottenere attraverso lo sviluppo della relazione struttura dell'alimento/benefici salutari e attraverso i concetti fondamentali della materia soffice. In particolare, sono state progettate nuove capsule per il rilascio controllato di composti bioattivi, che potranno essere utilizzate come ingrediente per nuovi alimenti funzionali. Lo sviluppo di un prodotto realmente innovativo per la salute e il benessere ha richiesto la sovrapposizione di conoscenze specifiche nel campo della scienza dei materiali alimentari, dell'ingegneria dei processi e dei principi base della fisica della materia soffice.

La prima parte del lavoro, descritta nel *capitolo 1*, è finalizzata alla selezione di un appropriato materiale da utilizzare come parete per le capsule. A riguardo sono stati condotti numerosi esperimenti volti allo studio delle cinetiche di gelazione e delle proprietà reologiche dell'alginato, un biopolimero naturale caratterizzato da proprietà particolari che lo hanno reso negli ultimi anni matrice ideale per l'incapsulamento e il rilascio di numerosi bioattivi. Nello specifico, le cinetiche di gelazione dell'alginato sono state investigate tramite *Photon Correlation Imaging* (in collaborazione con il Politecnico di Milano) e attraverso analisi reologiche a grandi deformazioni. I risultati ottenuti evidenziano il comportamento non-diffusivo del fronte di gelazione e l'esistenza di dinamiche di ristrutturazione eterogenee simili a quelle esistenti in altri gel colloidali. Un'analisi comparativa delle proprietà meccaniche dei gel ottenuti a diversi stadi di gelazione ha evidenziato con successo le peculiarità dei gel alginici, che derivano principalmente dalla natura non-permanente dei suoi legami.

Dopo aver definito un appropriato materiale di parete, la sfida maggiore per lo sviluppo di microcapsule commercializzabili consiste nella messa a punto di un processo di produzione appropriato in grado di conferire le proprietà morfologiche e di stabilità desiderate. Per tale ragione la seconda parte del lavoro sperimentale, descritta nel *capitolo 2*, è finalizzata alla realizzazione di un impianto su scala di laboratorio in grado di produrre microcapsule di alginato. In particolare, il materiale di parete e il filler da incapsulare vengono pompati attraverso un ugello di coestrusione a geometria concentrica. Un disco rotante taglia il getto in uscita dall'ugello, permettendo così la formazione di piccole gocce che gelano a contatto con un agente di *cross-link*. Dopo un'opportuna ottimizzazione dei parametri chiave del processo, è stato possibile produrre microcapsule monodisperse di diametro 0.73 mm contenenti un cuore liquido di bioattivo.

Le proprietà funzionali di differenti microcapsule sono state valutate nella terza parte della ricerca (vedi *capitolo 3*) Nello specifico la diffusione di microsfere di alginato contenenti cianocobalamina in soluzione acquosa, in presenza o meno di un secondo polimero con funzione di doppio rivestimento, è stata valutata simulando il flusso peristaltico proprio del contenuto del lume intestinale. Il modello d'intestino simulato utilizzato, già progettato e sviluppato dall'Università di Birmingham, mima i flussi peristaltici attraverso un meccanismo pneumatico in grado di riprodurre i caratteristici movimenti intestinali responsabili dell'avanzamento del bolo alimentare. Gli esperimenti di diffusione condotti hanno mostrato una buona ritenzione della vitamina trasportata, permettendo il calcolo di un flusso di massa complessivo. La diffusività sembra essere direttamente correlata alla solubilità del materiale parete. Altri tipi di microcapsule, contenenti un ceppo modificato di *Bifidobacterium longum* luminescente, sono state utilizzate efficacemente per proteggere la vitalità dei batteri probiotici in condizioni gastriche simulate.

Nella progettazione di un ingrediente funzionale un prerequisito è che esso possa assolvere la propria

specifica funzione e, al contempo, rimanere sufficientemente gradevole al palato. L'ingegnerizzazione di queste proprietà, oltre ad essere necessaria ed estremamente stimolante, può essere ottenuta su differenti scale di lunghezza. A riguardo, l'influenza delle dimensioni nel rilascio del bioattivo è stata affrontato nell'ultimo capitolo (*vedi capitolo 4*) della tesi. In particolare la ricerca, sviluppata in collaborazione con il gruppo "Food and Soft Material" dell'ETH di Zurigo, ha esplorato le potenzialità dell'utilizzo di un processo fisico per la produzione di nanoparticelle biopolimeriche (*solvent shifting*). E' stata chiaramente dimostrata la possibilità di produrre nanosfere con diametro piccolo fino a 20 nanometri senza l'utilizzo di alcun tipo di energia di *mixing*. Le nanoparticelle sono state studiate mediante l'utilizzo di tecniche ottiche avanzate come *light scattering* dinamico e *light scattering* dinamico depolarizzato ed utilizzate in esperimenti preliminari per migliorare la stabilità di un'emulsione alimentare spontanea.

Il lavoro svolto in questa tesi ha fornito un effettivo contributo per la comprensione dell'influenza delle proprietà strutturali dei materiali alimentari sul veicolo di proprietà salutari e nutrizionali. Tali risultati sono uno step essenziale nello studio degli aspetti bio-fisici e gastro-intestinali dell'assorbimento di nutrienti. Per la generazione di proprietà funzionali, la loro preservazione e il loro trasporto è stato seguito un approccio innovativo, che esplora la relazione esistente tra proprietà del materiale, processo e destrutturazione in ambiente intestinale. Tale approccio si basa sui concetti di strutturazioni dinamiche multiscala e su strategie biofisiche di disegno della struttura.

PREFACE

The food industry is constantly challenged to meet consumer demands for new food products that are safe, convenient, affordable, pleasurable and healthy. An understanding of fundamental structure and function relationships of food components is a key to stimulate and accelerate the development of innovative, complex and highly structured products and suitable production processes: ingredient formulation and production processes have a major role in commercial food development but their impact on food structure is poorly characterized. Furthermore the influence of structure and physical properties on the nutritional and health inducing properties of foods (e.g. bioavailability/efficacy of nutrients/ bioactives) has received fragmented research. The food structure design way to food innovation covers a multidisciplinary food research domain (food engineering, biophysics, applied soft matter, food technology, applied human nutrition) and activities are strategically designed in the frame of a integrated process & product design and engineering approach for creating innovative multiphase structured foods with targeted health benefits and optimal sensory characteristics. With the goal of health supporting functions, the process engineering for food properties generation, preservation and delivery relies on the concepts of multiscale structure dynamics and on biophysics-driven strategies for structure design.
In this framework, the aim of the Thesis is the design of health supporting food functions with development of food structure/health benefits relationships based on fundamental soft material concepts. This *soft matter approach* can be really well integrated in the more general concept of *tailor made food*, which already redesigned the way foods are produced (van der Sman, 2012). An application has been developed to bioactive encapsulation with manufacturing of new ingredients, water in water emulsions as carriers of vitamins and probiotics. Since physiological efficacy of bioactives is often impaired when they are incorporated in food matrices and undergo typical food processing regimes or they may impact negatively on the disintegration process in the gastrointestinal tract of human body, the Thesis will increase knowledge on the influence of structure and physical properties of food materials on the nutritional and health inducing properties of new ingredients as carriers of bioactives.

For many years food scientist have successfully used tools from different disciplines for developing food product. Consumer science delivers data on consumer preferences and acceptance and provides a basis for new product development. Nutritional science delivers the needs with respect to energy intake and also identifies any need to fortify foods with bioactive molecules. Chemical engineering gives important tools to control the large-scale production of manufactured foods, thereby optimizing throughput and ensuring food safety (Aguilera and Stanley, 1999). However, only recently the scientific community is giving more emphasis on food structuring for delivery of functionality (Lesmes and McClements, 2006). In this framework, over the past few years foods are studied as one of the most complex types of soft matter (Mezzenga *et al.,* 2005; Mezzenga, 2007; Tolstoguzov, 2000) and a number of scientist recognize the potential of soft condensed matter physics to understand and control food structure (Foegeding, 2007; adé Kruif, 1995; Dickinson, 2006; Chen and Mackley, 2006; Marangoni *et al,* 2007; Strybulevych, 2007; van der Sman, 2007; van der Sman and van der Graaf, 2006; van der Sman and var der Groot, 2008; Ubbink, 2008) Consequently, food science has been evolving in line with the progress being made in other branches of soft matter condensed physics, triggered by a continuous improving insight into the nature of biomaterials and by the development of new experimental techniques (Donald*,* 2004).

Borrowing some typical concept of soft matter physics, in the *first chapter* of this manuscript we will discuss the dynamics of alginate gels, a natural polymer extensively used in the food industry as thickening agent. For such polymer the typical length scale is somewhat defined by the mesh size of the formed network. We will see that the dynamics of alginate gels are strictly related to its gelation

condition, resulting in a tunable length scale, which affects directly the properties of the gels such as their rheological response to deformation and stress.
In the *second chapter* we will present in details a method for the production of novel food structures based on alginate gels, which are designed as controlled release vehicles. A detailed overview of their application and functional properties, in particular under simulated gastro intestinal conditions, will be given in *chapter 3* of this thesis.
Finally, in *chapter 4* we will focus our research on self assembled solid emulsion at the smallest length scale. In this section we will first give the ternary phase diagram for a totally food grade polymer/solvent/non solvent system, obtained by using advanced optical techniques. Then, the possibility to produce polymer nanoparticles without any kind of mixing energy will be discussed. Preliminary application will be also presented.

Main scientific goal of the thesis in the design of health supporting food functions are:

1. Design of complex polymer and colloidal systems with structure/health benefits in nano and microstructures for bioactive controlled release
2. Structure forming encapsulation technology for the manufacturing of micro and nano carriers intended for bioactive delivery
3. Bio-physical and gastro intestinal engineering aspects of nutrient absorption.

REFERENCES

1. adé Kruif KG, Hoffmann MA, van Marle ME, van Mil PJ, Roefs SP, Verheul M and Zoon N, 1995, Gelation of proteins from milk. *Faraday Discussions*, *101*, 185-200.
2. Aguilera JM and Stanley D W, 1999. Microstructural Principles of Food Processing and Engineering. Aspen Publishers, Gaithersburg.
3. Chen YW and Mackley M R, 2006, Flexible chocolate Soft Matter, 2: 304–309
4. Dickinson E, 2006, Colloid science of mixed ingredients. Soft Matter, 2(8): 642–652
5. Donald A, 2004, Food for thought. Nature Mater. 3, 579-581
6. Foegeding A, 2007, Rheology and sensory texture of biopolymer gels. Curr. Opin. Colloid Interface Sci., 12: 242–250
7. Lesmes U, McClements DJ, 2009. Structure–function relationships to guide rational design and fabrication of particulate food delivery systems, Trends in Food Sci. and Tech., 20(10) 448:457
8. Marangoni AG, Idziak S H J, Vega C, Batte H, Ollivon M, Jantzi PS and Rush W E, 2007, Encapsulation-stucturing of edible oil attenuates acute elevation of blood lipids and insulin in humans. Soft Matter, 3(2):183–187
9. Mezzenga R, 2007, Equilibrium and non-equilibrium structures in complex food systems. Food Hydrocolloids, 21: 674–682
10. Mezzenga R, Schurtenberger P, Burbidge A and Michel M, 2005, Understanding foods as soft materials. Nat. Mater., 4: 729–740
11. Strybulevych A, Leroy V, Scanlon MG and Page JH, 2007, Characterizing a model food gel containing bubbles and solid inclusions using ultrasound. Soft Matter, 3: 1388–1394
12. Tolstoguzov V, 2000, Foods as dispersed systems. Thermodynamic aspects of composition-property relationships in formulated food. J. Therm. Anal. Cal., 61(2): 397–409
13. Ubbink J, Burbidge A, and Mezzenga R, 2008, Food structure and functionality: a soft matter perspective. Soft Matter, 4 (8): 1569–1581
14. van der Sman RGM and van der Goot AJ, 2008, The science of food structuring. Soft Matter, 5: 501-510
15. van der Sman RGM and van der Graaf S, 2006, Diffuse interface model of surfactant adsorption onto flat and droplet interfaces. Rheol. Acta, 46(1): 3–11
16. van der Sman RGM, 2007, Soft condensed matter perspective on moisture transport in cooking

meat. AIChE J, 53(11): 2986–2995
17. van der Sman RGM, 2012, Soft matter approaches to food structuring. Adv. Colloid Interface Sci., 176-177: 18-30.

1. ALGINATE: GELATION, AGING AND DYNAMICS

1. Alginate gelation studies

1.1. INTRODUCTION

Encapsulation technology is receiving increasing commercial attention for protection and delivery of bioactives in food applications. Indeed, many bioactives are often unstable, and when directly incorporated in foods, besides altering flavour and texture, may be prone to degradation before reaching the target site within the body. It was already shown that encapsulation could consistently improve their bioactivity and physiological effect (Augustin and Sanguansri, 2008). In addition to the selection of an appropriate process to provide the desired morphology, stability, and release mechanism, the challenges in developing commercially viable capsules rely on the selection of the most appropriate shell formulation materials. Among a wide class of natural biopolymers, which include traditional foodstuff such as starch and pectins, an increasingly important role is taken by alginate, actually a family of unbranched polysaccharides isolated from brown seaweeds, which is one of the extensively used materials in tissue engineering (Augst *et al*., 2006), for immobilizing living cells and (Smidsrød 1974), and recently, to obtain, when mixed with polyacrylamide, highly stretchable composite gels (Sun *et al*., 2012). One of the major advantages of alginate as encapsulating material is its aptitude to adhere to intestinal tissues, where bioactive substances can be released at a controlled rate, a feature that can be critical in food, biomedical, and pharmaceutical applications (Pawar and Edgar, 2012). The performance of alginate microbeads would be however greatly improved, provided that the mechanism governing the polymer gelation process was well understood. (Augst *et al*, 2006; Draget *et al*, 1997)

Structurally, alginates are block copolymers composed of β-D-mannuronic acid (M) and α-L-guluronic acid (G) arranged in a block wise pattern where homopolymeric regions of M (M-blocks) and G (G-blocks) residues are interspersed by regions of alternating structures (GM-blocks) (Morris *et al.*, 1978). Gelation is due to the association of sequences of guluronate, linked di-axially along the chain, whereas the mannuronate residues are linked equatorially. The guluronate residues adopt a regular 2-fold symmetry-giving rise to a buckled chain. In the presence of divalent ions, Ca^{++} in our experiment, interchain association occurs by dimerization of chain sequences with the cations sandwiched within the dimer on specific sites along each of the interior surfaces. This is commonly referred to as the "egg-box" model (Potter *et al*.,1994). The mannuronate residues in alginate give sites with both 2- and 3-fold symmetry, but the equatorial linkages lead to a much flatter structure, which can less readily accommodate the cations. Models of the alginate gelation processes simplify this complex mechanism considering that a divalent metal ion interact with the guluronic residues of the alginate polymer and forms a networked structure that physically gels the solution. The interaction can be expressed in terms of the reaction stoichiometry as

$$n_C\ Ca^{++} + \text{Alginate} \longrightarrow Ca - \text{Alginate} \qquad \textbf{(1.1)}$$

The simplest choice of the stoichiometric coefficient $n_c = 0.5$ means that two molecules of alginate are bridged by the divalent ion (Mancini, 1999). A more refined theory (Morris *et al*, 1978) link n_c to the guluronic acid content X_G of the alginate. According to the egg-box model, the maximum binding capacity is ¾ Ca^{++} per guluronic acid residue, such that

$$n_C = 3X_G/4 \qquad \textbf{(1.2)}$$

In our experiment $X_G = 0.56$ (see Table 1.1) and $n_c = 0.42$. This simplified "egg-box" model has recently been questioned, since GM blocks too are found to contribute to chain cross-linking, albeit to a lesser extent (Donati *et al*, 2005). All evidence suggests anyway that alginate gels are held together by non-covalent bonds primarily due to ion bridging, although hydrogen bonds and dispersion forces may also contribute to the gel strength (Zhao *et al*., 2011). At variance with the chemical bonds in simple polymer gels, these "physical" cross-links are prone to break and reform to relax local internal stresses that build up upon gelation. Such a non-permanent, reversible nature of the cross-links is very likely to be responsible for the thermo-reversibility of alginate gels and for their propensity to display creep behavior over long times (Donati *et al*, 2005; Zhao *et al*, 2011). Moreover, the macroscopic

properties of the gel are expected to depend not only on the density, strength, and lateral extent of the cross-links, but also on their restructuring kinetics (Donati *et al*, 2009; Mancini *et al*, 1999).

In this section, through a detailed investigation performed by photon correlation imaging, a novel light scattering technique particularly suitable to investigate the microscopic dynamics of spatially inhomogeneous systems, we highlight and discuss several features of the gelation kinetics and the restructuring processes in alginate gels generated by the slow perfusion of $CaCl_2$ (Brambilla *et al*, 2011). In particular, the advancement of the gelation front, accurately marked by a dramatic increase of dynamic time correlations, displays a very surprising, non-diffusive time behaviour, which can hardly be reconciled with the existing gelation model. After the formation of a dynamically quasi-arrested structure, the gel undergoes a time evolution characterized by a first consistent restructuring and strengthening accompanied by a progressive slowing-down of the local dynamics, followed by a much longer period marked by drastic and abrupt global "fluidization" events, which do not apparently lead to significant changes of the gel structure, but presumably contribute to a slow "creeping" behaviour observed for the gel at very long time. Finally, the macroscopic mechanical properties of the gel show evident traces of the temporal evolution analyzed by PCI, giving experimental evidence that alginate gels share many properties in common with attractive colloidal glasses. Our results therefore suggest that the physical mechanisms that are supposed to account for the mechanical and rheological properties of soft glassy systems may have a wider generality, and may be shared by polymer gels with physical cross-links.

1.2. MATERIALS AND METHODS

1.2.1. Chemicals

Sodium alginate (Algogel 6020) was obtained from Cargill Inc., France, and used without further purification. Reagent grade sodium chloride and calcium chloride were purchased from Sigma Aldrich. The polymer mannuronic and guluronic weight fractions, whose values strongly influence the gelling process, have been determined as described by Grasdalen (1983), and are reported in Table 1.1. Size exclusion chromatography yields a polymer number–averaged molecular weight $M_n \simeq 110$ kDa (corresponding to a degree of polymerization of about 560), and a weight–averaged molecular weight $M_w \simeq 330$. Hence, this natural biopolymer displays a very large degree of polydispersity $M_w/M_n \simeq 3$. Sterile solutions of this alginate were prepared by dissolving solid Na^+-alginate in the desired volume of deionized water. Sodium azide 0.02% (w/w) was added to prevent microbiological growth, and gelation was induced by slowly permeating the solutions with $CaCl_2$ according to the protocols described in what follows.

X_G	X_{GG}	X_M	X_{GM+MG}	X_{MM}
0.56	0.26	0.44	0.30	0.14

Table 1.1 Mannuronic (X_M) and guluronic (X_G) weight fractions in Algogel 6020, and weight fractions of the dimeric units X_{GG}, X_{GM+MG} and X_{MM}.

1.2.2. Photon correlation imaging

Photon Correlation Imaging (PCI) is a recently introduced optical method, suitable to investigate slow dynamics in colloidal glasses and gels by measuring the time-correlation function of the scattered light, as in standard Dynamic Light Scattering (DLS), but with the major advantage of allowing for spatial resolution by investigating the local dynamics at distinct points within the scattering volume. We shall give only a summary description of PCI, mainly emphasizing the rich amount of physical information that can be extracted using this powerful technique, and referring to the seminal contributions by L. Cipelletti and co-workers for a more detailed analysis (Cipelletti *et al*, 2003; Maccarrone *et al*, 2010). Basically, the experiment consists of forming on a multi-pixel camera an image of the scattering volume, observed at a given scattering angle ϑ, through a suitably stopped-down optics (see Fig. 1.1a).

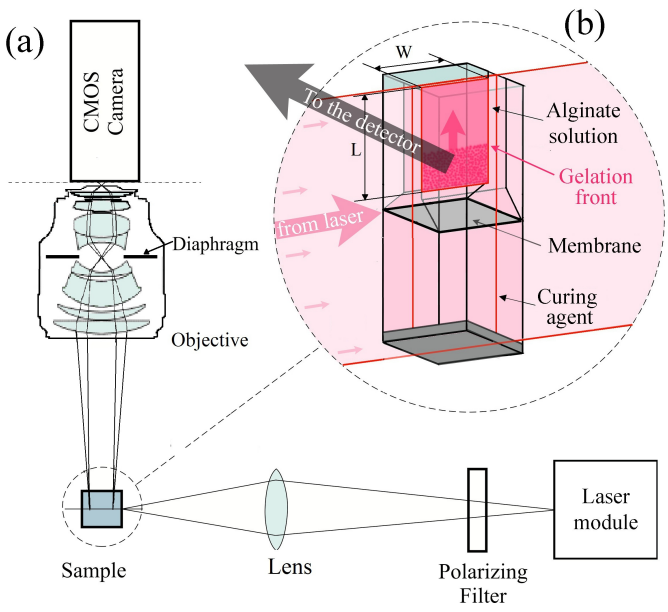

Figure 0.1 (a) Scheme of the PCI setup in a 90° scattering angle configuration. (b) Scheme of the optical cell used to perform gelation.

In other words, the imaging optics is provided with a partially closed iris diaphragm placed in the focal plane of the lens that, besides accurately selecting the scattering wave-vector $q=(4\pi/\lambda)\sin(\vartheta/2)$, causes the image to become "speckled" because the intensity at each given point on the image plane originates from the interference of the field scattered by a finite size region in the sample plane. The simultaneous measurement of the time-dynamics over many speckles yielded by the multi-pixel detector, besides providing a fast ensemble averaging of the intensity correlation function (crucial when investigating samples with a very slow dynamics), allows us to identify the occurrence and follow the temporal evolution of those dynamic effects associated with the presence of spatial heterogeneities in the investigated sample. Quantitatively, the latter can be characterized as follows. First, the speckle pattern is subdivided into "regions of interest" (ROIs) by grouping together a given number of adjacent pixels. Then, one introduces the so-called "degree of space–time correlation" (or "correlation index") $c_I(\tau;t,\mathbf{r})$ between two images taken at times t and $t+\tau$ as

$$c_i(\tau;t,r) = \frac{\langle I_p(t) I_p(t+\tau)\rangle_r}{\langle I_p(t)\rangle_r \langle I_p(t+\tau)\rangle_r} - 1 \qquad \textbf{(1.3)}$$

where I_p is the scattered intensity measured by the p^{th} pixel and $\langle\ldots\rangle_{\mathbf{r}}$ denotes an average over all pixels within a ROI centered around $\mathbf{r}$. Hence, $c_I(\tau;t,\mathbf{r})$ is simply related to the covariance between the intensity measured on the same speckle at two different times, sampled over the given ROI and, in particular, $c_I(0;t,\mathbf{r})$ is the relative variance of the intensity in $\mathbf{r}$ at time t. Note that c_I is a function of the delay time s that, in samples displaying a restructuring and aging kinetics, depends parametrically on the aging time t (and, for spatially inhomogeneous samples like those considered in this work, also on the local position $\mathbf{r}$). In fact, as shown in what follows, it is exactly this time-dependence that yields the basic features of the gelation process. Provided that the investigated kinetics is sufficiently slow, however, the statistical accuracy can be enhanced by time averaging $c_I(\tau;t,\mathbf{r})$ over a time window δt that is much shorter than the characteristic evolution time of the investigated kinetics, which allows us to reduce the statistical noise due to finite sampling on the limited number of pixels in a ROI. The local dynamics can then be quantified by defining:

$$g_2(\tau) - 1 = \langle c_I(\tau; t, r) \rangle_{\delta t} \quad \textbf{(1.4)}$$

Such a "coarse-grained" correlation index actually bears the same information of the intensity correlation function measured in a standard DLS experiment, yet with the crucial advantage of a much better statistical accuracy due to pre-averaging over the speckles in a ROI, which allows averaging over a time window δt much shorter than the total measurement time required in a DLS measurement. In glassy or gelling systems, however, the correlation index also displays intrinsic fluctuations, which are not just due to the instrumental noise associated with finite sampling, but to real physical processes taking place in the system. A striking manifestation of these physical fluctuations on which we shall particularly focus is the occurrence of sudden "correlation bursts" due to structural rearrangements that rapidly propagate over large regions of the sample. Such a "dynamic heterogeneity" can be investigated by considering the (coarse-grained) variance of $c_I(\tau;t,r)$ on a ROI

$$\chi(\tau) = \langle c_I(\tau; t, r)^2 \rangle_{\delta t} - \langle c_I(\tau; t, r) \rangle_{\delta t}^2 \quad \textbf{(1.5)}$$

which quantifies the temporal evolution of the restructuring events taking place at a given location and aging time. As shown in the above equation, the dependence of $\chi(\tau)$ on the delay τ allows us to easily set apart slow changes of the local dynamics associated with aging from the aforementioned sudden global restructuring events. Whereas the former processes are indeed characterized by a peak in the local value of χ occurring at a delay time τ comparable to the relaxation time of $g_2(\tau)$ and getting more pronounced the larger the size of the correlated region within the sample (Berthier *et al*, 2005)., the latter are highlighted by a sudden increase of $\chi(\tau)$ over the whole sample which is not correlated with the local dynamics. What is also particularly interesting for the present study is that PCI, besides being a sensitive probe of the dynamic slowing-down and kinetic arrest associated with gelation, also allows us to detect and map the presence of hydrodynamic motion in the sample. Indeed, whereas standard DLS can detect only relative particle motion (in other words, provided that the scattering volume is uniformly illuminated, the far field speckle pattern generated by a system of scatterers in uniform motion remains stationary), in a PCI configuration the speckle motion on the image plane faithfully maps the local flow field within the sample. As in standard Particle Imaging Velocimetry (PIV) (Takumaru and Dimotakis, 1995) techniques this allows us to obtain via a FFT algorithm the spatial cross-correlation function of the speckle pattern at different times t_1 and t_2. In this scheme, the local sample displacement in the time interval t_2-t_1 is related to the position of the cross-correlation peak, whereas the height of the peak itself decays on a time scale set by the Brownian dynamics of the sample measured at a wave-vector q. This technique, which has been successfully used to probe the collapse and restructuring of colloidal depletion gels (Brambilla *et al*, 2011), proves to be extremely useful for investigation of the detailed mechanism by which gelation proceeds. To follow gelation, the alginate solution is confined to the lower, optically accessible part of a cuvette (VWR International), by a porous membrane with 100 mm pore size, which is mounted on a custom-made plastic frame that tightly fits into the wedge-shaped connection between the sample compartment and an upper reservoir (see Fig. 1.1b).

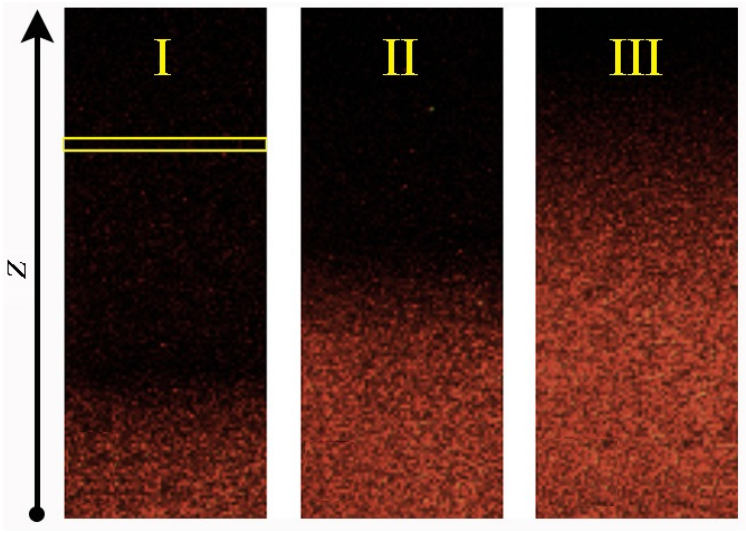

Figure 0.2 Snapshots of the cell taken about 13 (I), 25 (II), and 45 (III) hours after the curing agent has been poured into the reservoir. The *z* axis indicates the measurement coordinate, whereas the yellow box indicates the size and shape of a ROI.

This cell geometry allows us to laterally image a rectangular area *S* within the sample with a vertical extent $L \approx 16$ mm and a horizontal width $W \approx 6.4$ mm, which allows mapping the sample region extending from the cell bottom down to about 3.5 mm over the membrane (in the following, we call *z* the vertical distance from the bottom of *S*). Gelation is started by gently pouring the curing agent (a 0.1 M $CaCl_2$ solution) in the reservoir atop the membrane, carefully avoiding the presence of air bubbles. The cell is then rapidly turned upside down and mounted on the cell holder with the reservoir at the bottom to avoid convection effects that may arise from the fact that the $CaCl_2$ solution is slightly denser than the alginate fluid (see also Section 1.3.2). The illumination optics is composed of a 50 mW semiconductor laser module operating at $\lambda = 656$ nm (SY Lasiris SNF501L, StockerYale, New Hampshire, USA) that includes a holographic grating allowing us, with the aid of a lens (f = 300 mm), to shape the beam on the cell entrance window as a uniform vertical sheet of width $w = 20$ mm (see Fig. 1.1a). An objective images the investigated sample region *S* on a rectangular area with a size of 300 px 120 px of a CMOS camera sensor (Optikam Pro5, Ponteranica, Italy), whereas a diaphragm placed in the objective focus selects a scattering angle $\vartheta = 90°$ (corresponding to a scattering wave-vector $q \simeq 1.8 \times 10^5$ cm^{-1}) with a speckle size of about 3 px x 3 px. The exposure time is typically set to 1/15 s, with a time interval between successive images of 30 s, and the sensor gain is tuned during the gelation process so as to optimize the intensity of the speckle pattern within the gel phase. Since during the gelation kinetics the intensity and correlation index are expected to depend only on the vertical position *z*, the speckle pattern image was subdivided into 30 ROIs with a height of 10 px (corresponding to about 530 mm in the sample) and laterally extending over the whole width *W* of the investigated sample region (120 px). Each ROI contains therefore about 100 speckles, a value which was found to yield a good vertical resolution with an acceptable statistical noise in the correlation function. If necessary, spatial resolution can nonetheless be simply improved by changing the imaging lens and focusing on a smaller gel region. Finally, the space–time resolved correlation index $c_I(\tau;t,\boldsymbol{r})$ is then computed for each ROI using a custom-made code running on ImageJ, a public domain image processing software.

1.2.3. Mechanical properties

To investigate the macroscopic mechanical properties of alginate hydrogels, several gel samples were prepared by pouring the liquid solution of alginate into dialysis tubes with a diameter of 21 mm (Sigma

1. Alginate gelation studies

Aldrich, MWCO 12 000) and an overall length of 200 mm, which were then sealed and immersed in a water bath containing a 0.1 M calcium chloride solution. To detect the effects of microscopic restructuring observed by PCI on the gel macroscopic properties, the samples were extracted in sequence from the gelation bath after a curing time increasing from 6 hours up to 6 days. Each cylinder was transversally cut into cylindrical sections, which were then separately subjected to uniaxial compression tests using a texture analyzer TA (XTplus, Stable Micro System, England) operating at T = 23°C. To eliminate any effect due to the non-ideal cutting of the cylinders, the samples are sandwiched between the upper and lower plates of the TA, and first pre-loaded with a stress of about 2–3 kPa, so as to compress them to a length h_0 that is about 2% smaller than the unperturbed value. Measurements then consist of further compressing them at a minimum constant speed of V = 1 mm s^{-1} from an initial height h_0, accurately measured after the pre-stress has been applied, up to rupture. To check for reproducibility, tests were repeated on several samples for each value of the time spent in the gelation bath. To obtain the stress relaxation curve behavior, similar cylindrical gel samples were submitted to a quasi-static uniaxial compression at constant deformation, and the stress recorded as a function of time for a maximal duration of about 1 h. The initial deformation was applied at the very high strain rate of 33 mm s^{-1}, allowing us to consider it as quasi-instantaneous.

1.3. RESULTS AND DISCUSSIONS

1.3.1. General features of the gelation process

A preliminary qualitative description of the progress of the gelation process permits us to single-out its main features and set apart distinct time regimes, allowing us at the same time to familiarize with the kind of information that can be extracted from a comparative analysis of the intensity and degree of correlation profiles obtained by PCI. With a negligible delay, due to the time it takes to cross the separating membrane, the curing agent that has been poured into the lower compartment of the cell starts diffusing into the upper compartment, triggering the onset of alginate gelation and generating a gelation front that propagates upwards, as shown by the three snapshots in Fig. 1.2. Visually, this front is marked by a noticeable increase of the scattered intensity in the cell region already invaded by the $CaCl_2$ solution. This effect can be related to the microscopic dynamics of the gelling alginate solution by contrasting the time behaviour of the scattered intensity and the correlation index on a single ROI of the sample, located at z = 5 mm from the cell bottom (namely, approximately 8 mm above the membrane). Fig. 1.3 shows that at $t_0 \simeq$ 24h, roughly corresponding to the time it takes for the curing solution to propagate from the membrane up to the ROI location, after an initial dip the scattering intensity starts to grow, reaching a plateau which is about 20 times larger than its value at t = 0. The rising part of the intensity is rather well fitted by an exponential with a time constant $t_a \simeq$ 850 s. Since an increase of the scattering intensity witnesses a change in the sample structure factor, this means that structural rearrangements keep on taking place in the ROI for a long period of time, quantified by the "aging" time t_a. The temporal evolution of the local microscopic dynamics is, however, very different.

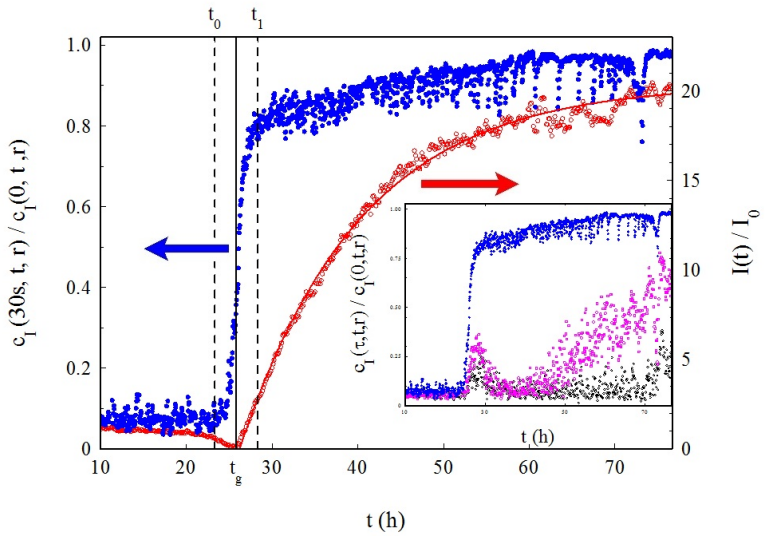

Figure 0.3 Time dependence of the intensity ratio $I(t)/I(0)$ (open dots, right axis) and the normalized degree of the space–time correlation $\hat{c}_I(\tau,t,z)$ after a delay of τ = 30 s (bullets, left axis),measured for a ROI centered at z = 5mm. The full line is an exponential fit to the intensity curve for $t > t_g$ with a time constant $ta \simeq$850 s. The inset shows the normalized correlation index at delay times τ = 10 min and τ = 50 min.

To highlight this contrasting behavior, it is useful to introduce a "normalized" degree of correlation by taking the ratio $\hat{c}_I(\tau;t,z) = c_I(\tau;t,z)/c_I(0;t,z)$ of $c_I(\tau;t,z)$ to its value at τ = 0. Let us first concentrate on the behavior of $\hat{c}_I$ for shortest delay time τ = 30 s between two images of the ROI. Since the decay time of the correlation function for a fluid alginate solution, measured by standard DLS at the same q-vector, is of about 25 ms, it is not surprising that, for $t < t_0$, the correlation index between the two speckle patterns is basically zero. However, as soon as the scattered intensity starts to change, $\hat{c}_I(\tau;t,z)$ shows a rapid increase, reaching a value of about 0.9 in a few minutes. In other words, for $t > t_1$ the speckle pattern is still fully correlated after a delay time that is more than two orders of magnitude

longer than the correlation time of the alginate solution. Hence, for $t > t_1$, the whole alginate solution in the ROI is already a quasi-arrested gel, where however noticeable structural rearrangements, highlighted by the persisting increase of $I(t)$, are still going on. Noticing that t_1-t_0 is of the order of magnitude of the time it takes for the Ca^{++} ions to traverse the ROI, the conversion of the solution into a dynamically arrested structure can be assumed to take place almost instantaneously when the curing agent becomes available. Such a sharp dynamic arrest allows us to take $t_g = (t_0 + t_1)/2$ as a reasonable average time in the ROI marking the transition from a fluid to a gelled system. By quasi-arrested, however, we mean that residual dynamic effects persist in the gel well beyond t_g. The inset in Fig. 1.3 shows indeed that the degree of correlation still decays over much longer delays. Indeed, after a delay of $\tau = 50$ min, $\hat{c}_I(t)$ has decreased to zero even at a time t when $I(t)$ has basically reached its plateau value. If at this stage structural changes are associated with such a long time decay of the correlations, they are too weak to be mirrored by changes in the scattering intensity at the selected q-vector. Actually, we have not detected a fully arrested dynamics after any ripening time. An investigation of the macroscopic stress relaxation discussed in Section 1.3.6 shows that such a long persistence of diffusive microscopic dynamics is arguably responsible for a slow macroscopic creeping of alginate gels.

1.3.2. Kinetic of the gelation front

The abrupt increase of c_I suggests that dynamic arrest, or at least a dramatic increase of the correlation time imputable to the formation of a loose gel structure, is a quasi-instantaneous process, taking place as soon as Ca^{++} comes into contact with alginate. The time-dependence of the advancement of the gelation front along the cell, tracked by plotting the "gelling time" t_g for each single ROI, is however quite surprising. Fig. 1.4 shows that the gelation front advances indeed linearly with time with a speed of $v_g = z(t_g)/t_g \simeq 0.3$ mm h^{-1} over the whole investigated range. Extrapolated to $t_g = 0$, the linear fit yields z = - 2.8 mm, which is consistent with the estimated position of the membrane. Note also that the time $t_1 - t_0$ it takes for c_I at a delay time of 30 s to switch up to a value close to one is approximately constant and in good agreement with the time it takes for the gelation front to cross a ROI at the constant speed v_g.

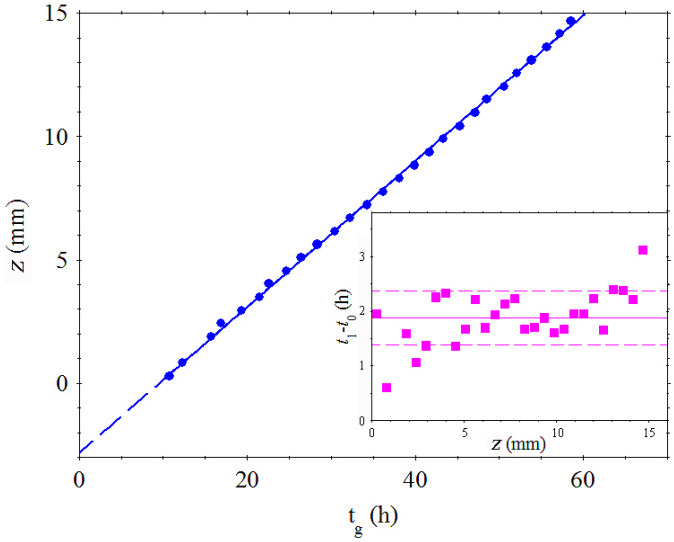

Figure 0.4 Kinetics of the gelation front, showing the position z corresponding to a specific gelling time $t_g = (t_1 + t_0)/2$. The linear fit yields an advancing speed $v_g \simeq 0.3$ mm h^{-1}, and an intercept $z(0) \simeq - 2.8$ mm, approximately coincident to the position of the separating membrane. The inset shows that $t_1 - t_0$ is almost independent from the position in the cell, roughly amounting to the time it takes for the gelation front to traverse a ROI at the constant speed v_g (here full and broken lines indicate the average value and standard deviation of $t_1 - t_0$).

This striking experimental evidence can hardly be reconciled with the existing models of alginate gelation. The most widely used approach, due to Mikkelsen and Elgsaeter (1995, M–E model), is indeed based on assuming that the local concentration of both calcium ions and free alginate behaves diffusively, decreasing at the same time because of the formation of the polymer gel. The latter is conversely assumed to be immobile, with a local concentration that steadily grows because of two different mechanisms, the inclusion of an additional monomer to an already formed network and the novel association between two free chains. For a generic dependence of the diffusion coefficients on the concentration of the three species, these assumptions lead to a set of nonlinear equations that must be solved numerically (Mikkelsen and Elgsaeter, 1995). However, within the (strongly) simplifying assumption of constant diffusion coefficients of alginate and calcium ions, the M–E model becomes just a particular case of a reaction–diffusion process, which has been extensively investigated in the literature because of its large interest both in chemical and biological pattern formation (Liesegang 1896), and in the context of diffusion limited aggregation (Witten Jr. and Sander, 1981), with sophisticated methods (Barkema *et al.*, 1996; Koza, 1996). When applied to gelation, these analytical solutions yield a gelation front position $z_f(t)$ that, for initially separated reagents at concentrations a_0 and c_0, behaves diffusively, $z_f^2(t) \longrightarrow D_f t$ for $t \longrightarrow \infty$, with a long-time front diffusion coefficient D_f that can be evaluated by equating the fluxes of the reactants at the position of the gelation front (Koza, 1996). Whereas a suitable dependence of the diffusion coefficients on the concentration of the reacting species may lead to a time behavior which is not strictly diffusive, as observed in other experiments (Thu *et al.*, 2000; Braschler *et al.*, 2011), it is much harder spotting a clear physical mechanism yielding a gelation front that, instead of a diffusing, propagates at a constant speed along the cell. A possible explanation may be hinted by the initial moderate decrease in intensity which is detected just in the region where c_1 starts to grow (namely, close to the leading edge of the gelation front, see Fig. 1.3), which is observed to a greater or lesser extent for all the ROIs. Such a dip in the scattered intensity may reasonably be attributed to the presence of a thin layer before the advancing gel, with a thickness of the order of a few hundred microns, where the concentration of alginate is sensibly lower than in the bulk. The physical origin of such a "depletion layer", which has apparently been observed in other measurements of alginate gelation (Braschler *et al.*, 2011; Thumbs and Kohler, 1996), is not easy to spot. Tentatively, we suggest that it could stem from a mechanism that is not included in the M–E model: syneresis, namely a progressive shrinking over long times of the structure by solvent ejection, which is a common and extensively studied phenomenon in polymer gels. In the investigated sample, syneresis of the alginate matrix is already highlighted for times slightly exceeding the gelation time of the whole sample by the onset of a slow uniform translation of the speckle field, witnessing a backward motion of the whole gel structure towards the negative z direction, which eventually leads, at much longer times, to gel detachment from the cell bottom and lateral walls. However, gel shrinking is very likely to take place even before, while the gelation front advances and the gel gets progressively reinforced by the increase in the cross-link density supplied by the incoming Ca^{++} ions. Since the diffusion constant of alginate is very low, this might presumably leave a polymer-depleted region just on top of the gel. Whether or not this physical mechanics is plausible, the presence of the depletion layer implies that there is a region within the sample where the density profile of the solution gets inverted, regardless of whether the alginate or the curing solution is initially placed on top. Such an inverted density profile is hydrodynamically instable, unavoidably leading to micro-convective effects. The latter, however slow, would noticeably modify the spatial distribution of the curing agent, leading in general to a quasi-uniform concentration profile within the depletion layer. The presence of convective flow is commonly expected and often experimentally observed to accelerate transport processes with respect to their purely diffusive limit (Kiselev and Ryzhik, 2001). Micro-convection within the depletion layer may thus lead to a very different time behavior of the gelation front (Thumbs and Kohler, 1996). To support this view, we tried to enhance convective effects by repeating the same experiment, but without turning the cell upside down, so that the heavier curing solution lies on top of the alginate solution. Fig. 1.5, where the times t_2 required for the scattering intensity to double its initial value (which is just slightly longer than t_g) are compared, shows that in the presence of

macroscopic convection, the time it takes for the scattered intensity to double its initial value linearly depends on the position z, yet the front advances with a speed that is more than three times larger than in the hydrostatically stable case.

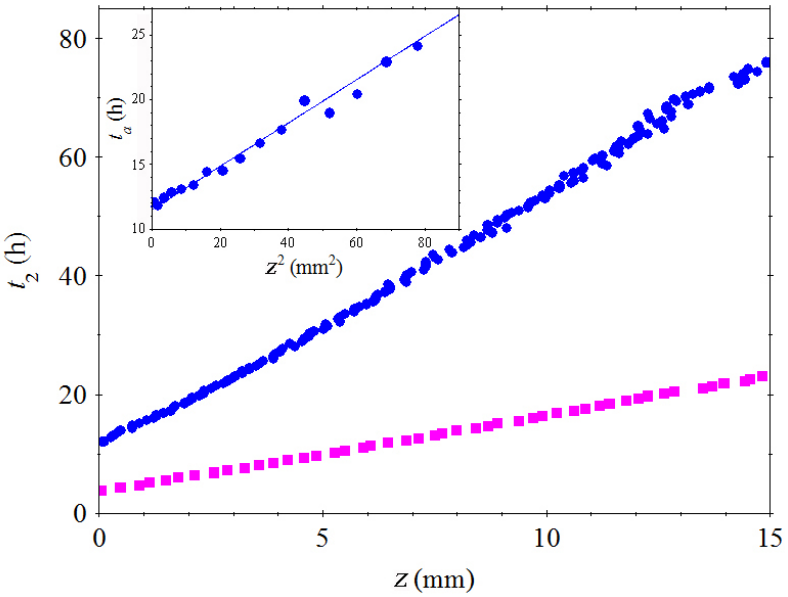

Figure 0.5 Time t_2 required for the scattered intensity to double its initial value, as a function of the position in the cell, for the sample discussed in the text (bullets), and for an identical sample placed in the cell mounting with the reservoir containing the curing agent at the top (squares). The inset shows the dependence of the aging time t_a, obtained from an exponential fit to the growth of the scattered intensity curve, on the square of the measuring coordinate z.

This evidence, although far from being conclusive, shows that convective effects, which are not considered in the simple diffusion/reaction model, may drastically change the time behaviour of a gelation process. This observation may be relevant in most practical applications of alginate, where the adopted geometry implies horizontal concentration gradients, unavoidably leading to convection. Nonetheless, effects related to the spreading of the advancing front of the curing agent can be detected by looking at the aging time t_a, defined like in Section 1.3.1 as the time constant of the exponential growth of the scattered intensity at a given position z. The inset in Fig. 1.5 shows indeed that t_a grows quadratically with z from a minimum value $t_{a0} \simeq 11.5$ h at $z = 0$. Such an increase can be reasonably attributed to a delay in the supply of the additional Ca^{++} ions required for the loose percolating structure formed at t_g to "ripen". Fitting the curve as $z(t) = [D(t_a - t_{a0})]^{1/2}$ actually yields a fit parameter $D \simeq 1.7 \times 10^{-5} cm^2 s^{-1}$, which has the typical order of magnitude of the diffusion coefficient of small ions. This rather strange combination of a linearly advancing gelation front with a gel aging that shows evident traces of the ion permeation of an already gelled structure points out the need for further studies of the kinetics of gelation processes in gels with ionic cross-links.

1.3.3. Gel aging

The progressive change in the gel dynamics during the restructuring period following t_g can be quantitatively analyzed by means of the correlation functions defined in eqn (1.4), using a coarse-graining time interval of $\delta t = 100$ min that, as shown below, is still much shorter than the aging time scale of the gel. Fig. 1.6 shows that all correlation functions $g_2(\tau) - 1$ obtained on a ROI located at $z = 0.5$ mm eventually decay to zero regardless of the aging time, confirming that the gel dynamics is never fully arrested.

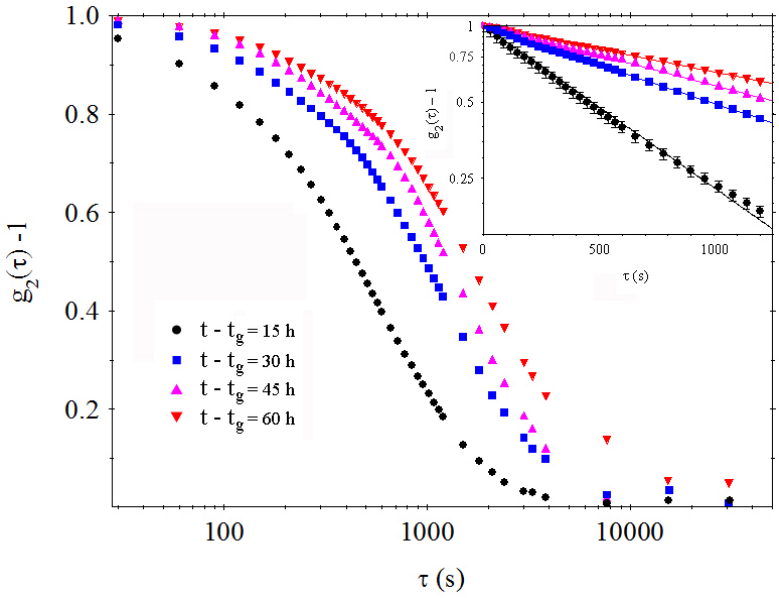

Figure 0.6 Correlation functions $g_2(\tau)$ -1 obtained in a fixed ROI located at z = 0.5 mm, measured at different aging times t - t_g: the semilogarithmic plot in the inset shows that the correlation functions decay roughly exponentially, with a decay constant τ_r that substantially grows with t.

The semi-logarithmic plot in the inset shows that the decay of $g_2(\tau)$ - *1* is reasonably well fitted by a single exponential decay, with a relaxation time τ_r that grows with the aging time, increasing by more than two order of magnitudes before possibly starting to level off. A qualitatively similar behavior is found analyzing different ROIs. In order to compare the aging behavior at long times for different sample locations, it is useful to evaluate the dynamics counting the time, for each single ROI, from the moment when the gel has locally reached a comparable restructuring time. The latter can be consistently stated as the sum of the time t_g when the dynamic arrest takes place with the subsequent characteristic aging time t_a. Fig. 1.7 shows that the results for τ_r at different ROIs, when plotted as a function of the shifted time $\Delta t(z) = t - [t_g(z) + t_a(z)]$ at the ROI position z, rescale on a single master curve. This means that, to a good approximation, the dynamic evolution of the gel, when referred to Δt, does not depend on the position along the sample. This is further confirmed by the inset in the figure, showing that the full correlation functions obtained for different ROIs at the same value Δt superimpose quite well. These observations suggest that, once the gel restructuring reaches a final stage, the microscopic dynamics is spatially homogeneous along the sample and depends only on the "local" age of the gel.

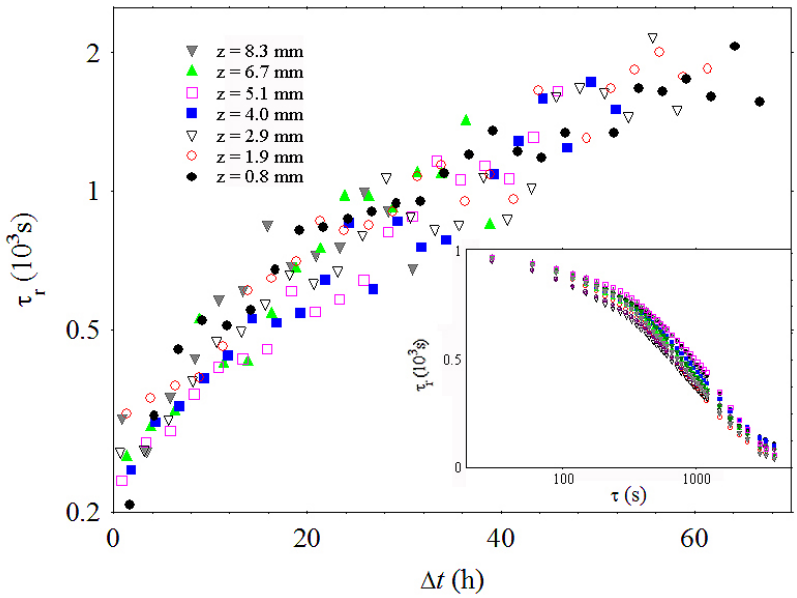

Figure 0.7 Microscopic relaxation time τ_r as a function of $\Delta t(h)$ measured with respect to a time-origin $t_g(z) + t_a(z)$, given for each ROI an approximate indication of the instant when the gel has reached an almost stationary structure. The positions along the cell corresponding to the different symbols are specificated in the legend. The inset shows that the full correlation functions obtained for different ROIs at the same value Δt almost superimpose.

At first sight, a simple exponential form of the correlation functions in a complex system like a gel looks rather surprising. Actually, when colloidal or polymer gels are probed over length scales, set by the inverse scattering wave-vector q^{-1}, which are smaller than the mesh size ξ, $g_2(\tau)$ usually displays a very complex behavior basically reflecting internal relaxation processes, which share many aspects in common with the correlation functions observed in glassy systems. However, we probe the gel structure over a length scale of $q^{-1} \simeq 55$ nm, which is quite larger than the typical mesh size $\xi = 5$–15 nm of alginate gels (Klein *et al.,* 1983). In fact, internal modes, which have typical relaxation times in the range of hundreds of μs (Strand *et al.,* 1982), (hence 5 orders of magnitude shorter than the first delay $\tau_1 = 30$ s measured by PCI), are responsible only for the tiny reduction with respect to the ones in the apparent intercepts of the correlation functions shown in Fig. 1.6. Notice that the latter, which is already as small as 5% for a relatively "young" gel ($t - t_g = 15$ h), becomes totally negligible as the gel ages. The very slow dynamics detected by PCI has therefore a radically different physical origin. In the past few years, several experimental and theoretical investigations have indeed suggested that weak colloidal gels and soft glassy systems may exhibit distinctive dynamical features, driven by the accumulation of internal stresses (Cipelletti *et al.,*2000; Duri and Cipelletti, 2006), generated on a microscopic scale by bond formation and rupture. These stresses relax via localized microcollapses creating a long-range elastic deformation field and constituting the elementary steps leading to a progressive gel compaction. On the much longer time scales of such a microscopic stress relaxation, the DLS correlation functions are predicted to behave very differently, both in terms of shape and q-dependence. Whereas the superposition of internal mode relaxations yield a short-time dynamics which is often well described by a stretched exponential, $g_2(\tau)$ may display a compressed exponential form, namely, the instantaneous decay rate increases with time. A general model based on the relaxation of stress dipoles (Bouchaud and Pitard, 2001), shows that, provided that the microcollapses take place very rapidly, the behavior of $g_2(\tau)$ is set by a characteristic time scale $\tau_q \simeq \eta(q\xi)/G^I$, where

G^I is the gel compression modulus, and η is the dynamic viscosity. Specifically, $ln[g(\tau)]$ decays as:

$$\ln[g(\tau)] \sim \begin{cases} (q\tau)^{3/2} & \tau \ll \overline{\tau_q} \\ q^{3/2}\tau & \tau \gg \overline{\tau_q} \end{cases} \qquad (1.6)$$

The experimental results for a very weak colloidal gel, with a compression modulus of $G^I \simeq 0.1$ mPa, actually support both the compressed exponential form of $g(\tau)$ and the q^{-1} dependence of its decay rate predicted by the upper expression in eqn (1.6) (Cipelletti *et al.,*2000; Duri and Cipelletti, 2006). As we shall see in Section 1.3.5, however, the elastic moduli of the alginate gels we investigate are hugely larger, in the range of 10^2 kPa. Hence it is not surprising that the decay of $g_2(\tau)$ is very well fitted by a simple exponential, as predicted by eqn (1.6) for $\tau \gg \tau_q$. Note that, even in this case, the decay rate should still display a non-diffusive $q^{3/2}$ behavior. Unfortunately, our experimental setup cannot be simply adapted to investigate the q-dependence of $g_2(\tau)$, which might yield an interesting test of the stress-dipole. Nevertheless, when $ln[g(\tau)] \sim q^{3/2}\tau$, the stress-dipole relaxation model predicts the experimental decay time of $g_2(t)$ to grow linearly with the gel aging time. Fig. 1.7 shows that indeed, to a good approximation, τ_Γ increases linearly with Δt in all ROIs, giving an indirect support to the model.

1.3.4. Dynamic heterogeneity

The aging of colloidal gels, made of particles linked by short-range attractive interactions, is usually also characterized by a strongly heterogeneous dynamics (Duri *et al.,*2005; Bissing *et al*., 2003). This means that the local degree of correlation at a given time shows strong spatial fluctuations. Moreover, on top of the micro-scale collapses that are supposed to yield the overall decay of the local correlation functions, according to the model described in the former section, the gel aging is characterized also by structural rearrangements witnessed by abrupt decreases of the degree of correlation ("spikes") that extend over wide regions of the sample. The result presented in what follows show that a very similar behavior is shared by alginate polymer gels with physical cross-links. Studying gels characterized by an aging stage varying along the z direction allows us to investigate by PCI how the degree spatial and temporal heterogeneity qualitatively and quantitatively depends on aging. Striking evidence of the sudden rearrangements characterizing the heterogeneous dynamics of aging alginate gels can be obtained by focusing on a single structural rearrangement event visualized by means of a so-called "dynamical activity map", where the spatial distribution of the correlation index is represented by a false-color map (Duri *et al.,* 2009). In order to clearly point out that dynamic heterogeneity occurs not only along the aging direction, but also at constant z (namely, within gel regions that are supposed to be structurally homogeneous, at least on the average), it is useful to redefine the subdivision of the sample into regions of interest as follows. A first ROI in the speckle pattern is constructed as a 15 px x 15 px square. Then, all the other ROIs are generated by shifting the latter by 5 px along either the z-axis or the horizontal coordinate x. Besides yielding a much clearer visualization, this method, although introducing some correlation between adjacent partially overlapping ROIs, can be shown to ensure better spatial resolution. To each of these regions is then attributed the average value of the normalized correlation index $\hat{c}_I(\tau;t,\boldsymbol{r})$ within the ROI, evaluated at the delay time τ = 30 s. Fig. 1.8 shows a typical sequence of maps referring to a single rearrangement event. In the first map, referring to a starting time $t = t^*$ just before the rearrangement occurs, a fully correlated region (in red), where the sample is already dynamically arrested, can be clearly told apart from a fully uncorrelated zone (in blue) close to the top of the observation region, where gelation has not yet taken place. Moreover, a decrease of the degree of correlation by increasing z witnesses the different aging stages within the gel phase. In the second activity map, taken at starting times $t^* + \tau$, a rearrangement event generating close to the gel interface is seen to turn the whole gel into a dynamically active structure that almost completely looses correlation within a delay time τ, showing that the events rapidly propagate over macroscopically large length scales. Subsequently, correlation is recovered starting from the bottom, more "aged" part of the gel, until, at $t \simeq t^* + 3\tau$ the gel reverts to a state that does not substantially differ from the original one.

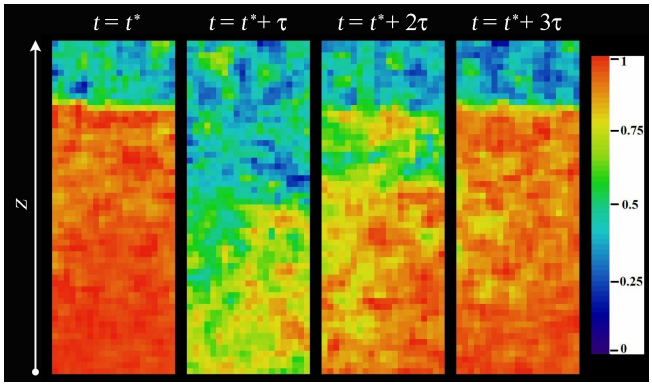

Figure 0.8 Sequence of activity maps, obtained as described in the text, referring to a single restructuring event taking place at a time $t^* \simeq 40$ h after sample preparation. The scale to the right displays the color scale for the normalized degree of correlation $\hat{c}_I(30\text{ s};t,r)$.

The possibility that these correlation drops are not artifacts due to a rigid motion of the speckle field (Duri *et al.,* 2009), generated for instance by a sudden detachment of the gel from the cell walls as a consequence of a macroscopic shrinkage, can be easily ruled out by an image correlation velocimetry analysis (Brambilla *et al*, 2011). As already mentioned, gel shrinking effects can conversely be clearly detected after gelation has taken place over the whole sample. These results, together with those discussed in Section 1.3.3, suggest that there are two kinds of dynamic processes taking place in an aging alginate gel: a progressive slowing down of the local microscopic dynamics, witnessed by the increase of the structural relaxation time τ_r, and an intermittent sequence of restructuring "bursts", involving the whole sample but not leaving any significant trace on the gel structure, at least apparently. These two different processes are better appreciated by considering the time behavior of the fluctuations in c_I, expressed by its (coarse-grained) variance $\chi(\tau)$. As discussed in Section 1.2, this amounts to evaluating how much the degree of correlation after a delay time τ fluctuates over the pixels in a given ROI, taking than the average of the standard deviation of c_I over a short time window δt. In the two panels of Fig. 1.9, which refer to two ROIs at different vertical positions z, the behavior of χ as a function of τ is represented by a single vertical line of thickness δt with a color code that varies from blue to red with an increasing value of $\chi(\tau)$, whereas the way $\chi(\tau)$ changes with the time t after sample preparation is monitored on the horizontal axis. On both ROIs, the structural rearrangements leading to the slowing down of the local microscopic dynamics are associated with a strong increase of $\chi(\tau)$ at short delays τ, lasting for a significant fraction of the aging time t_a. Since both t_g and t_a depend on z, both the temporal location and the duration of this process are considerably different for the two ROIs.

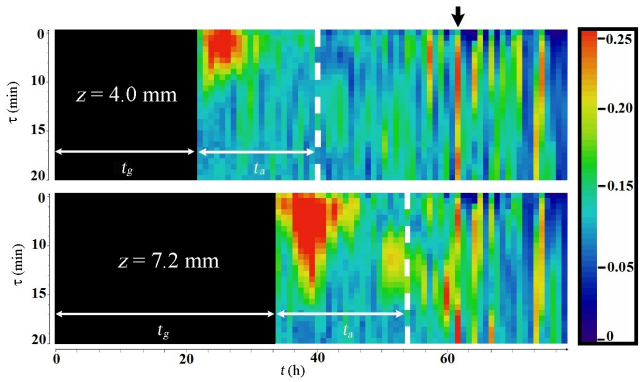

Figure 0.9 Dependence on the delay time τ (vertical axis) of the standard deviation $\chi(\tau)$ of the correlation index, shown in the color code, as a function of time t. The two graphs refer to different ROIs displaying the indicated gelation and aging times t_g, t_a. The arrow points at a typical abrupt de-correlation burst.

A more detailed analysis shows that $\chi(\tau)$ is peaked around the value of the structural relaxation time τ_r at time t, whereas the amplitude of the peak progressively decreases with τ. Conversely, after the main structural rearrangement on spatial scales of the order of q^{-1} has completed (namely, for $t > t_a$ when the local dynamics has reached the quasi-homogenous stage shown in Fig. 1.7), sudden increases of $\chi(\tau)$ lasting for a time $t \leq \delta t$, but persisting for much longer delays τ, take place. Since these events correspond to de-correlation bursts rapidly propagating over the whole sample, they take place at the same time on the two ROIs, namely, their timing is not dictated by the local aging stage, but only on the absolute time t. Such a temporal coincidence of the de-correlation bursts on different sample regions is strikingly highlighted by Fig. 1.10, where a time window of about 20 h, beginning at $t > t_g + t_a$, is shown for five different ROIs along the sample.

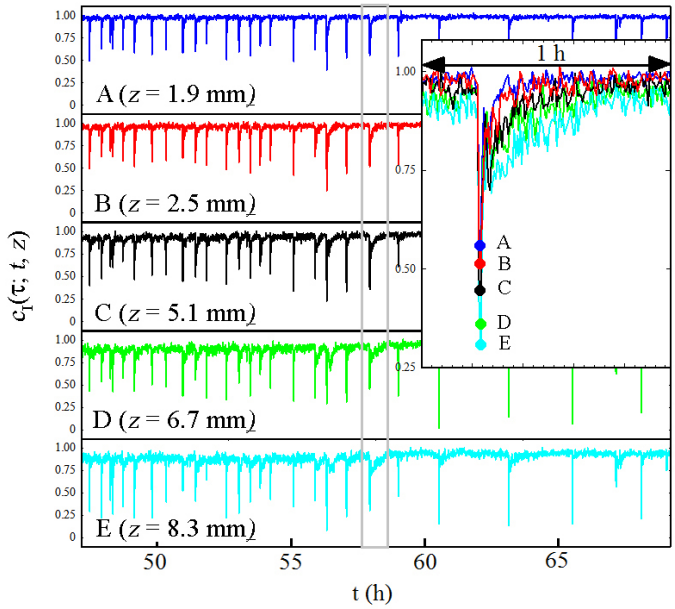

Figure 0.10 Coincident "spiking" behavior of $c_I(\tau;t,z)$ for five different ROIs over a time window of about 20 h. The inset shows the superposition of the spiking events occurring between the two grey lines in all the ROIs**.**

Notice that the time interval between two consecutive drops increases with the aging time. The evolution of the gel towards a more homogeneous state, witnessed for $t - t_g < t_a$ both by the behavior of the local dynamics and by the fading of the fluctuations in c_I, is then also accompanied by a later progressive decrease of the frequency of global rearrangements persisting for a very long time. Although the timing of the global de-correlation events is the same over the whole gel, the amplitude and duration of a single spike on a specific ROI depends on the aging stage of the latter. The inset in Fig. 1.10 shows indeed that the bursts get stronger and longer with z. This means that the sample regions where the gel is relatively "younger" are more affected by the rearrangement and take more time to revert to their original state.

Mechanical properties of the gels

The alginate gels whose macroscopic properties we investigated were prepared according to a procedure which had to necessarily be quite different from the way gelation was obtained in the PCI experiments. Here gelation proceeds from the membrane inwards, hence the longitudinal compression measurements performed at a given aging time reflect only the average mechanical properties of gels whose structure varies along the radial direction. This amounts to testing simultaneously a set of parallel "springs" whose elastic constants physically correspond to gels at diverse aging stages. The compression and stress relaxation tests discussed in this section are not therefore meant to provide a full mechanical characterization of alginate gels, but rather to support qualitatively our microscopic PCI investigation. Nonetheless, our preliminary data already bear clear evidence of the progressive overall aging of the gel structure, and yield further hints on the nature and kinetics of cross-links in alginate gels.

1.3.5. Uni-axial compression test

We first discuss the results of uniaxial compression tests obtained as described in Section 1.2 for alginate solutions kept in the gelation bath for a period of time ranging between 6 h, roughly corresponding for the selected experimental geometry to the minimum time required to obtain a macroscopic weak gel, and 144 h. The samples were compressed at constant speed from an initial length h_0 to a final length h, and the uniaxial compression stress σ_m in excess of the pre-stress value defined in Section 1.2 was measured as a function of the strain $\lambda = 1 - h/h_0$. The experimental excess stress σ_m was then corrected for the increase of gel cross-section at a constant volume to obtain the "true" stress $\sigma = \sigma_m(1 - \lambda)$. The double-log plot in the inset of Fig. 1.11 shows that the overall stress–strain relationships for different aging times t progressively merge into a single curve, characterizing the region where a consistent strain hardening is observed. With the exception of the samples kept in the gelation bath for 6 h, the maximum compression that the gels can sustain before rupture is almost independent of t. An expanded linear view of the different curves of $\sigma(\lambda)$ for a compressional strain not exceeding $\lambda \simeq 0.2$, shown in the main body of Fig. 1.11, first displays a linear increase of $\sigma(\lambda)$ (full lines), corresponding to a Young's modulus $E = \sigma/\lambda$ that steadily increases from $E \simeq 150$ kPa to $E \simeq 350$ kPa with increasing gelation time. This linear elastic region (region I) is limited however to compression values not exceeding about 5%, and is followed by a roll-off rapidly leading to a behavior which is still linear, but corresponds to an apparent elastic constant E_0 x 120 kPa which is almost independent of sample aging (region II). The lower-right inset shows that the intercept σ_0 of the linear fits (dotted lines) with the $\lambda = 0$ axis, corresponding to an apparent yield stress, grows roughly linearly with the gel Young's modulus E measured at small compression values. While the behavior at small λ shows that the gel stiffens with t, for a sufficiently large deformation the time spent in the gelation bath seems to affect the alginate gels only for what concerns σ_0, whereas their apparent compression modulus does not change. The latter observation, together with the merging of all the response curves in the strain hardening region, suggests that the gel elastic response at small λ may stem from the concurrence of more microscopic mechanisms, whereas larger deformations are controlled by a single mechanism, not affected by t. A similar behavior has been recently observed in gels made of synthetic alginates where the fractional content of GM alternating sequences can be carefully controlled by

Mørch *et al.* (2008), who pointed out that the gels display a degree of plasticity that increases with the length of the alternating GM blocks, very probably due to the restructuring of the junctions involving GM sequences. On the basis of this evidence, the observed stress–strain behavior can be accounted for by assuming that the crosslinks between GG sequences form at the early stages of the gelation process and are weakly affected both in number and strength by gel ripening, whereas additional links due to GM sequences increase in number and strength with aging, increasing the overall stiffness of the gel. Because the latter cross-links are weaker, they are more easily subject to breaking under stress than pure guluronate cross-links, so that, by increasing λ, the gel evolves from a state where its elastic response is due by both kinds of links to an intermediate pseudo-plastic state where the apparent Young's modulus is determined by the stiff GG bonds alone. Moreover, the separation between two different elastic regimes should be much more pronounced for more aged gels, in agreement with the experimental evidence (in fact, it is almost negligible at t = 6 h, when the inner part of the gel has barely formed). Such a different behavior of the two kinds of cross-links for what concerns their rates of formation and breaking can arguably be justified by the specific features of calcium binding to alginate, which takes place in three separate steps (Fang *et al.,* 2007): Ca^{++} ions first interact with a single guluronate unit to form ion–monomer complexes, which then pair to generate egg-box dimers eventually associating into bond sequences. Whereas the kinetic rate of the first step clearly does not depend on the kind of link that is formed, in the case of GG blocks, the following ones are however strongly cooperative due to the specific stereochemistry described by the egg-box model. In fact long sequences of paired GG blocks can form at a much faster rate[48]. Hence, the GG binding sites presumably get saturated as soon as the gelation front runs into them, while the subsequent gel ripening entails a slow spatial rearrangement of the GG junctions, but not their increase in number and strength. Conversely the cross-links formed by alternating GM sequences, which are known to be much less stereospecific (Donati *et al.,* 2009), grow at a much slower rate, progressively strengthening a basic framework mostly made of GG bonds. In this picture, rather large GG junctions are then seen as stiff, permanent blocks embedded into an elastic medium whose global elastic properties evolve however with the gel aging, because they depend on the number and strength of GM bonds too. The latter, which break and restructure much more easily than the large GG cross-link sequences (Donati *et al.,* 2009), actually provide an efficient way to relax local stresses in the gel. The presence of this weaker, easily restructuring links, is then likely to play a crucial role in determining the peculiar mechanical properties of a physical polymer gel like alginate (Sun *et al.,* 2012).

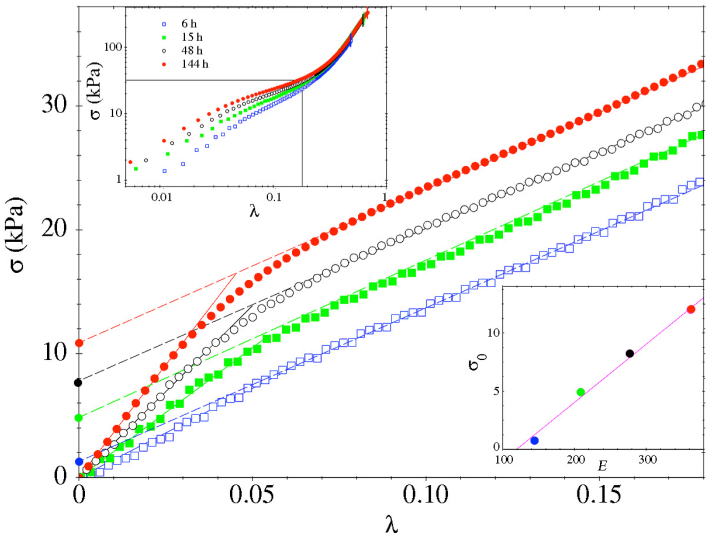

Figure 0.11 Upper-left inset: uniaxial stress–strain relationship for alginate gels made by permeation of a 0.1 M calcium chloride solution for the periods of time *t* shown in the legend, obtained at a compression speed of 1 mms^{-1}. Vertical bars indicate the maximum compression that each sample can bear before gel rupture. Each curve is obtained as the average of at least four samples obtained under the same conditions. Main body: expanded linear view. The boxed region, extending up to a maximum compression of about 20%. Lower-right inset: linear behaviour of the apparent yield stress σ_0 with the gel's Young's modulus *E*.

Let us briefly comment on the eventual strain-hardening behaviour of alginate gels at very large values of λ, which is actually shared by many other biopolymer gels. In the case of thin and flexible F-actin and intermediate filament networks, strain hardening may be accounted for by a nonlinear force-extension behavior of the individual filaments leading to a uniform affine deformation of the structure (Storm *et al*., 2005 and Gardel *et al*., 2004). Conversely, the response of a network consisting of stiff thick fibers, such as collagen and bundled actin, seems to be governed by collective bending deformations (Lieleg *et al*., 2007 and Onck *et al.,* 2005). Because it contains very large cross- link regions, often exceeding the size of the chain segments between two junctions, an alginate gel may be regarded as a kind of composite, simultaneously displaying the presence of stiff and soft regions (Zang *et al*., 2007). The non-linear elastic behavior of this composite polymer network has started to be investigated only recently (Sun *et al.,* 2012). When the volume fraction of the stiff component is so low that it does not form a percolating network, strain hardening can be accounted for by modelling the system as a fiber reinforced elastic composite, where the cross-link regions are regarded as stiff rods randomly and isotropically distributed in a softer matrix (Huisman *et al.,* 2010; Das and MacKintosh, 2010). Such a composite model, however, does not take into account the most peculiar property of polymer gels characterized by physical cross-links with a finite lifetime such as alginate, namely, that the network topology is unceasingly fluctuating because the cross-links continuously break and re-form at different locations. The experimental consequences of this ceaseless network dynamics is discussed in the next section.

1.3.6. Stress relaxation

At a compression speed of 1 mm s^{-1}, therefore, the gel responds to a uniaxial compression with a finite stress, displaying an overall behavior that, in regions I and II, resembles that of a "pseudo-plastic" solid. However, both the full decay of the correlation functions measured by PCI and the persistence of large scale restructuring bursts, witnessing that the microscopic dynamics never stops, suggest that the gel may actually creep macroscopically over a very long time, so that its mechanical response should be regarded as truly plastic. In other words, one may wonder whether the gel would actually yield

when deformed at an infinitesimally slow rate. This question is better answered by testing the value after a delay τ of the stress $\sigma(\tau)$ after a given compression has been rapidly applied at $\tau = 0$, for samples kept in the gelation bath for increasingly longer periods of time t. Here we present only the results obtained in the limits of a very short or very long t and to a single value $\lambda = 0.1$ of the initially applied strain, which roughly correspond to the initial part of region II in Fig. 1.11, where, according to our tentative interpretation, most of the GM cross-links have already opened up. This does not mean, however, that the weaker GM bonds should not contribute to stress relaxation, for novel cross-links of this kind may re-form and break while the sample relaxes.

A first clear evidence that can be extracted from the stress relaxation measurements shown in Fig. 1.12 is that the stress $\sigma(\tau)$ (made dimensionless by normalizing to its initial value) always decays asymptotically to zero, even for the largest curing time t = 144 h.

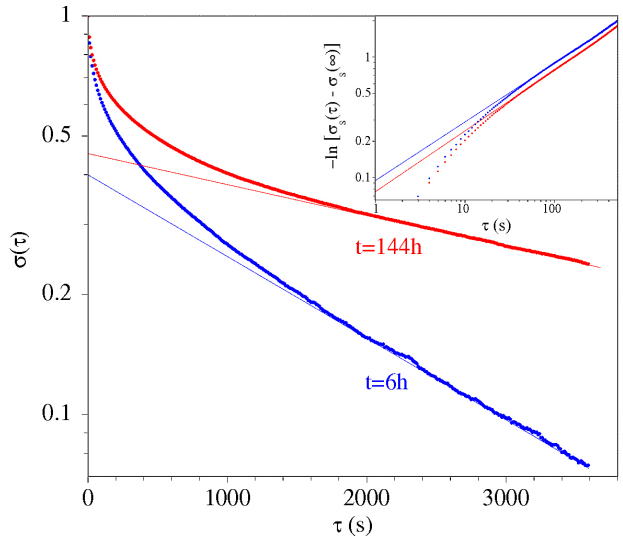

Figure 0.12 Main body: normalized stress σ, as a function of the delay time τ after a compression of 10% was rapidly applied, for samples kept in the gelation bath for 6 h and 144 h. Inset: negative logarithm $-\ln[\sigma_s(\tau) - \sigma_s(\infty)]$ of the short-time relaxations, obtained as discussed in the text, fitted with stretched exponentials in the range 50 s$\leq \tau \leq$500 s. The best-fit parameters are $\beta = 0.47$, $\tau_{\sigma s} = 115$ s for $t = 6$ h, and $\beta = 0.49$, $\tau_{\sigma s} = 150$ s for t = 144 h.

Thus, in the long time limit, all gels yield and comply to the applied strain, which actually implies a fully plastic behavior at vanishingly small compression rates. Hence, the stress–strain relationship depends on the compression rate, so that alginate gels behave in fact as thixotropic materials, albeit their creeping behavior is extremely slow. The semi-log plot shows that, at long delay time τ, the normalized stress displays a simple exponential decay

$$\sigma(\tau) \underset{t\to\infty}{\longrightarrow} \sigma_1(\tau) \sim exp(-\tau/\tau_{\sigma 1}) \qquad \textbf{(1.7)}$$

where the long-time stress decay constant $\tau_{\sigma 1}$ increases from about 2100 s for the weak gel kept in the gelation bath for just 6 h, to 5600 s for the most aged gel. Quite interestingly, these values are of the same order of magnitude of the microscopic relaxation time τ_r of the correlation functions in aged gels. The microscopic stress-relaxation model we used in Section 1.3.3 to account for the time behavior of $g_2(\tau)$ suggests a physical picture of the long-time creeping behavior of the gel expressed by eqn (1.7), possibly providing an explanation of the close similarity between $\tau_{\sigma 1}$ and τ_r. The decrease in $\sigma(\tau)$, which is in fact a decrease in the pressure felt by the compressing plate due to gel yielding, is of course

related to a progressive reduction of the overall gel strain $\lambda(\tau)$ through the stress–strain experimental relationship shown in Fig. 1.11, which deviates only moderately from linearity. If we assume that the macroscopic strain relaxation results from the addition of a large number of uncorrelated microscopic collapses occurring at random points in the gel, $\lambda(\tau)$ would be a Poisson process, exponentially decaying with the same time constant of the local correlation. At short time, however, the strain relaxation curve is significantly non-exponential, displaying in particular an extremely steep decay for $\tau \longrightarrow 0$, witnessing that, at short time, very fast relaxation mechanisms contribute to $\sigma(\tau)$ too. Stress relaxation curves are commonly fitted with an arbitrary superposition of exponentials that, however, are very hard to be attributed to specific physical mechanisms. It is conversely tempting to try to give an overall description of $\sigma(\tau)$ that, albeit approximate, may be related to a general physical picture. As a first guess, the long time contribution to the stress relaxation given by eqn 1.7 may be tentatively factorized out by writing

$$\sigma(\tau) = \sigma_1(\tau)\sigma_s(\tau) \qquad \textbf{(1.8)}$$

This amounts to assuming that the mechanism responsible for the long-time creeping of the gel is totally uncorrelated with the microscopic mechanisms contributing to the fast initial decay of $\sigma(\tau)$. This is a rather crude approximation, which however yields a short-time contribution that of course does not decay to zero, but to a finite value $\sigma_s(\infty) \simeq 0.4$ for both curves, a behavior actually expected for a fully arrested gel. Interestingly, by subtracting from $\sigma_s(\tau)$ its long-time plateau value both curves behaves very similarly and can be accurately fitted, except at very small τ, by a "stretched-exponential" (SE) function

$$\sigma_s(\tau) - \sigma_s(\infty) = exp\left[-(\tau/\tau_{\sigma s})^{\beta}\right] \qquad \textbf{(1.9)}$$

where $\tau_{\sigma s}$ is a characteristic time constant, and the exponent $b \leq 1$ accounts quantitatively for the amount of "stretching", lower values of b corresponding to a function that at short time decay much faster than a simple exponential with the same decay constant $\tau_{\sigma s}$, displaying however a much longer long-time tail. This behavior is better appreciated by plotting the (negative) logarithm of $\sigma_s(\tau) - \sigma_s(\infty)$. A pure stretched exponential yields indeed a power-law behavior $-ln[\sigma_s(\tau) - \sigma_s(\infty)] = (\tau/\tau_{\sigma s})^b$, which on a double log plot appears as a straight line with a slope b. As shown in the inset in Fig. 1.12, this is actually the case for s $\tau \gtrsim 30$–50 s. Moreover, both curves show an almost identical stretch exponent $b \simeq 0.5$, and close values of $\tau_{\sigma s} \simeq 100$–150 s. SE relaxations are observed frequently in a multitude of different physical situations ranging from the microscopic dynamics of super-cooled liquids and spin glasses (Gotze and Sjogren, 1992; Castaing and Souletie, 1991), to the response of critical mixtures and polymer solutions to external fields (Piazza *et al*., 1988; Degiorgio *et al.,* 1990). One of the reasons for the ubiquity of this functional behavior is because a SE behavior naturally emerges as the long-time asymptotic behavior of the superposition of parallel relaxation mechanisms that depend on a continuous parameter ℓ and individually yield an exponential decay with a time constant $\tau(\ell)$, provided that the probability distribution of these different mechanisms has the very general form $P(\ell) \sim exp\,[-(\ell / \ell_0)^p]$ (Continentino and Malozemoff, 1986). In particular, when $\tau(\ell)$ scales as ℓ^q, the stretch exponent is given by $b = p/(p + q)$. Since in our general picture the gel, initially subjected to an external stress, relaxes by the sequential breaking of cross-links of the alginate chains that can have widely different lengths ℓ and bond strengths, an overall SE relaxation of $\sigma_s(\tau)$ is not too surprising. Borrowing some basic concepts commonly used in describing stress relaxation in biopolymer bundles (Lieleg *et al*., 2011; Vink and Heussinger, 2012), we assume that breaking a bond of size made of ℓ individual Ca^{++} links requires an activation energy $E_a(\ell)$ linearly proportional to ℓ and the local longitudinal compressional force F the bond feels (Vink and Heussinger, 2012), which is directly related to the macroscopically applied stress. In a first approximation, the time τ_b it takes to cross the barrier and break the bond is given by the product of the Boltzmann factor of $E_a(\ell)$ times the

equilibrium lifetime of a single link τ_b^{eq} in the absence of an external load (Lieleg *et al.,* 2011), $\tau_b(\ell) = \tau_b^{eq} exp(F\ell/kT)$. Hence, assuming that bonds of a specific size ℓ lead to a single exponential decay of the stress proportional to $exp[-\tau/\tau_b(\ell)]$ (so that $q = 1$), a stretched exponential decay with $b \simeq 1/2$ would result from an exponentially decaying (p=1) probability distribution for the bond size ℓ or, approximately, even if $P(\ell)$ is a Poisson distribution with a low average value $<\ell>$. Although rather heuristic, this simple superposition model provides some clues for the origin of the short-time SE behavior of the stress relaxation in terms of local rearrangements.

1.4. REFERENCES

1. Augst AD, Kong HJ and Mooney D, 2006, Alginate Hydrogels as Biomaterials. Macromol. Biosci. 6: 623
2. Augustin MA, Sanguansri L, 2008, Encapsulation of Bioactives. In Food Materials Science, 577:601, Springer New York
3. Barkema G, Howard M and Cardy J,1996, Reaction-diffusion front for A+B→∅ in one dimension. Phys. Rev. E: Stat. Phys., Plasmas, Fluids, Relat. Interdiscip. Top., 53: 2017–2020.
4. Berthier L, Biroli G, Bouchaud J, Cipelletti L, El Masri D, L'Hˆote D, Ladieu F and Pierno M,2005, Direct Experimental Evidence of a Growing Length Scale Accompanying the Glass Transition. Science, 310:1797–1800.
5. Bissig H, Romer S, Cipelletti L,Trappe V and Schurtenberger P, 2003, Intermittent dynamics and hyper-aging in dense colloidal gels. PhysChemComm, 6:21–23.
6. Bouchaud J and Pitard E, 2001, Anomalous dynamical light scattering in soft glassy gels. Eur. Phys. J. E, 6: 231–236.
7. Brambilla G, Buzzaccaro S, Piazza R, Berthier L and Cipelletti L, 2011, Highly Nonlinear Dynamics in a Slowly Sedimenting Colloidal Gel. Phys. Rev. Lett.,106: 118302.
8. Braschler T, Valero A, Colella L, Pataky K, Brugger J and Renaud P, 2011, Link between alginate reaction front propagation and general reaction diffusion theory. Anal. Chem., 83:2234–2242.
9. Castaing B and Souletie J, 1991, Dynamic scaling and non exponential relaxations in the presence of disorder. Application to spin glasses. J. Phys., 1: 403.
10. Cipelletti L, Bissig H, Trappe V, Ballesta P and Mazoyer S, 2003, Time-resolved correlation: a new tool for studying temporally heterogeneous dynamics. J. Phys.: Condens. Matter, 15: S257.
11. Cipelletti L, Manley S, Ball R: C and Weitz DA, 2000, Universal Aging Features in the Restructuring of Fractal Colloidal Gels. Phys. Rev.Lett., 84: 2275–2278.
12. Continentino MA and Malozemoff AP, 1986, Dynamic scaling and the field-dependent critical line in a fractal cluster model of spin glasses. Phys. Rev. B:Condens. Matter, 33: 3591.
13. Das M and MacKintosh F, 2010, Poisson's Ratio in Composite Elastic Media with Rigid Rods. Phys. Rev. Lett., 105:138102.
14. Degiorgio V, Piazza R, Bellini F, Mantegazza T and Goldstein RE, 1990, Stretched-Exponential Relaxation of Electric Birefringence in Polymer Solutions. Phys. Rev. Lett., 64: 1043.
15. Donati I, Holtan S, Mørch Y**,** Borgogna M, Dentini M and Skj°ak-Bræk G, 2005, New Hypothesis on the Role of Alternating Sequences in Calcium−Alginate Gels. Biomacromolecules. 6:1031–1040.
16. Donati I, Mørch Y, Strand B, Skj°ak-Bræk G and Paoletti S 2009, Effect of Elongation of Alternating Sequences on Swelling Behavior and Large Deformation Properties of Natural Alginate Gels. J. Phys. Chem. B, 113: 12916–12922.
17. Draget KI, Skjåk-Bræk G, Smidsrød O, 1997, Alginate based new materials. International journal of biological macromolecules, 21 (1–2) 47:55
18. Duri A and Cipelletti L, 2006, Length scale dependence of dynamical heterogeneity in a colloidal fractal gel. Europhys. Lett., 76: 972–978.
19. Duri A, Bissig H, Trappe V and Cipelletti L, 2005, Time-resolved-correlation measurements of temporally heterogeneous dynamics. Phys. Rev. E: Stat. Phys., Plasmas, Fluids, Relat. Interdiscip. Top., 72: 051401.
20. Duri A, Sessoms D, Trappe V and Cipelletti L, 2009, Resolving Long-Range Spatial Correlations in Jammed Colloidal Systems Using Photon Correlation Imaging. Phys. Rev.Lett., 102: 085702.
21. Fang Y, Al-Assaf S, Phillips G, Nishinari K, Funami T, Williams P and Li L, 2007, Multiple Steps and Critical Behaviors of the Binding of Calcium to Alginate. J. Phys. Chem. B, 111:2456–2462.
22. Gardel M, Shin J, MacKintosh F, Mahadevan L, Matsudaira P and Weitz D, 2004 Elastic

Behavior of Cross-Linked and Bundled Actin Networks**.** Science, 304:1301–1305.
23. Gotze W and Sjogren L, 1992, Relaxation processes in supercooled liquids Rep. Prog. Phys., 55: 241.
24. Grasdalen H, 1983, High-field,< sup> 1</sup> H-NMR spectroscopy of alginate: sequential structure and linkage conformations. *Carbohydr.Res.*,118:255–260.
25. Huisman E, Heussinger C, Storm C and Barkema G, 2010, Semiflexible filamentous composites. Phys.Rev. Lett., 105: 118101.
26. Kiselev A and Ryzhik L, 2001, Enhancement of the traveling front speeds in reaction-diffusion equations with advection. Ann. Henri Poincare C, 18: 309–358.
27. Klein J, Stock J and Vorlop K, 1983, Pore size and properties of spherical Ca-alginate biocatalysts. Eur. J. Appl. Microbiol. Biotechnol.,18: 86–91.
28. Koza Z, 1996, The long-time behavior of initially separated A+ B→ 0 reaction-diffusion systems with arbitrary diffusion constants. J. Stat. Phys., 85: 179–191.
29. Lieleg O, Claessens M, Heussinger C, Frey E and Bausch A, 2007, Mechanics of bundled semiflexible polymer networks. Phys. Rev. Lett., 99: 88102.
30. Lieleg O, Kayser J, Brambilla G, Cipelletti L and Bausch A, 2011, Slow dynamics and internal stress relaxation in bundled cytoskeletal networks. Nat. Mater.,10: 236–242.
31. Liesegang R, 1896, Ueber einige eigenschaften von gallerten. Naturwiss. Wochenschr.,11: 353.
32. Maccarrone S, Brambilla G, Pravaz O, Duri A, Ciccotti M, Fromental J, Pashkovski E, Lips A, Sessoms D,Trappe V, et al., 2010, Ultra-long range correlations of the dynamics of jammed soft matter. Soft Matter, 6(21): 5514–5522.
33. Mancini M, Moresi M and Rancini R, 1999, Mechanical properties of alginate gels: empirical characterisation. J. Food Eng., 39(4):369–378.
34. Mikkelsen A and Elgsaeter A, 1995, Density distribution of calcium-induced alginate gels. A numerical study. Biopolymers, 36: 17–41.
35. Mørch Y, Holtan S, Donati I, Strand B and Skj°ak-Bræk G, 2008, Mechanical properties of C-5 epimerized alginates. Biomacromolecules, 9: 2360–2368.
36. Morris E, Rees D,Thom D and Boyd J, 1978, Chiroptical and stoichiometric evidence of a specific, primary dimerisation process in alginate gelation. Carbohydr. Res., 66: 145–154.
37. Onck P, Koeman T, van Dillen T and van der Giessen E, 2005, Alternative explanation of stiffening in cross-linked semiflexible networks. Phys. Rev. Lett., 95: 178102.
38. Pawar SN, Edgar KJ, 2012, Alginate derivatization: A review of chemistry, properties and applications. Biomaterials, 33 (11) 3279: 3305
39. Piazza R, Bellini T, Degiorgio V, Goldstein R, Leibler Sand Lipowsky R, 1988, Stretched-exponential relaxation of birefringence in a critical binary mixture. Phys. Rev. B: Condens. Matter, 38: 7223.
40. Potter K, Balcom B, Carpenter T and Hall L, 1994, The gelation of sodium alginate with calcium ions studied by magnetic resonance imaging (MRI). Carbohydr. Res., 257:117–126.
41. Smidsrød O, 1974, Molecular basis for some physical properties of alginates in the gel state. J. Chem. Soc., Faraday Trans., 57: 263.
42. Storm C, Pastore J, MacKintosh F, Lubensky T and Janmey P, 2005, Nonlinear elasticity in biological gels. Nature, 435: 191–194.
43. Strand KA, Bere A, Dalberg PS, Sikkeland T and Smidsrød O, 1982, Dynamic and static light scattering on aqueous solutions of sodium alginate. Macromolecules, 15: 570–579.
44. Sun J, Zhao X, Illeperuma W, Chaudhuri O, Oh K, Mooney D, Vlassak J and Suo Z, 2012, Highly stretchable and tough hydrogels. Nature, 489: 133–136.
45. Thu B, G°aserød O, Paus D, Mikkelsen A, Skj°ak-Bræk G, Toffanin R, Vittur F and Rizzo R, 2000, Inhomogeneous alginate gel spheres: An assessment of the polymer gradients by synchrotron radiation-induced x-ray emission, magnetic resonance microimaging, and mathematical modeling. Biopolymers, 53:60–71
46. Thumbs J and Kohler H, 1996, Capillaries in alginate gel as an example of dissipative structure

formation. Chem. Phys., 208: 9–24.
47. Tokumaru P and Dimotakis P, 1995, Image correlation velocimetry. Exp. Fluids,19:1–15.
48. Vink R and Heussinger C, 2012, Cross-linked biopolymer bundles: Cross-link reversibility leads to cooperative binding/unbinding phenomena.J. Chem. Phys., 136: 5102.
49. Witten Jr T and Sander L, 1981, Diffusion-limited aggregation, a kinetic critical phenomenon. Phys. Rev. Lett., 47: 1400–1403.
50. Zhang J, Daubert C and Allen Foegeding E, 2007, A proposed strain-hardening mechanism for alginate gels. J. Food Eng., 80: 157–165.
51. Zhao Y, Hu F, Evans J and Harris M, 2011, Study of sol–gel transition in calcium alginate system by population balance model. Chem. Eng. Sci., 66: 848–858.

2. PRODUCTION OF ALGINATE LIQUID-CORE MICROCAPSULES BY CO-EXTRUSION TECHNOLOGY

2. Production of alginate liquid-core microcapsules by co-extrusion technology

2.1. INTRODUCTION

The food industry expects increasingly complex properties from food ingredients. Obtain such complex properties requires new structuring technologies and knowledge and oftentimes can only be provided by encapsulation technology. Encapsulation has been used in the past to mask the unpleasant taste of certain ingredients and also to simply convert liquids to solids (Gouin, 2004). However, in recent years, the concept of controlled release of bioactive ingredients at the right place and the right time has become more and more interesting (Chen *et al*, 2006).

Food bioactives are physiologically active components in food or dietary supplements of plant or animal origin that have a role in health beyond basic nutrition. The range of food components now considered as bioactives include vitamins, minerals, functional lipids, probiotics, aminoacids, peptides and proteins, phytosterols, phytochemicals, and antioxidants and their use in foodstuff is exponentially increasing (Kris-Etherton *et al,* 2005). However, many of these bioactives are prone to degradation, they are unstable and incorporation in foods can alter flavour, odour and texture. They may be directly added to food if they are compatible with the food matrix and their direct addition does not impact negatively with the bioavailability of the bioactive. Moreover bioactivity needs to be maintained in order to have a physiological function when delivered to its particular target site within the body (Lopez-Rubio *et al*, 2006).

Encapsulation technology can be efficiently used for protection and delivery of bioactives in food applications (Champagne and Fustier, 2009). With carefully fine-tuned controlled release properties, microencapsulation is not just an added value, but is also the source of totally new ingredients with matchless properties. The growing interest by food technologists in the enormous potential of encapsulation is demonstrated by the exponential increase in the number of publications, as demonstrated by many review papers (King, 1995; Benita, 1998; Gibbs *et al*, 1999; Brazel (1999); Kondo, 2001; Augustin *et al*, 2001; Poncelet *et al*, 2002; Gouin, 2004; Desai and Jin Park, 2005; Madene *et al.,* 2006; Augustin and Hemar, 2009)

In encapsulation, components are packaged within a secondary material and delivered in small particles. Sophisticated shell materials and technologies have been developed and an extremely wide variety of functionalities can now be achieved through microencapsulation. Liposome entrapment (Kim and Baianu, 1999; Taylor *et al* 2005; da Silva *et al.* 2010), spinning disk (Senuma *et al*, 2005) and microfluidic devices (Skurtys and Aguilera, 2008), as well as coacervation (Augustin and Hemar, 2009) to as lesser extent, have experienced the most rapid growth in interest from researchers and technologists. Other widespread carriers are colloidosomes (Dinsmore *et al*, 2005) and solid-liquid nanoparticles (Muller *et al*, 2000; Saupe and Rades, 2006).

Although a wide range of wall forming materials and technologies for manufacturing microcapsules of different size, shape and morphological properties are commercially available, combination of triggers that can activate the release of entrapped substances are still under study, in particluar temperature (fat/wax matrices), moisture (hydrophilic matrices), pH (enteric coating, emulsion coalescence and others), enzymes (enteric coatings, as well as a variety of lipid, starch and protein matrices), shear (chewing, physical fracture). Moreover, when dealing with bioactive encapsulation, food scientists should always keep in mind that cost considerations in the food industry are much more stringent than in, for instance, the pharmaceutical or cosmetic industries. Therefore, the cost-in-use of the encapsulated product must be tolerable in the final foodstuff. Some microencapsulation technologies are really difficult to be scaled up and, however scientifically impressive they are, might not be appropriate for all, if any, applications. (Gouin, 2004) In order to meet these variables, a material science approach is advantageous to design solid emulsion from hydrocolloids, that is a category of targeted encapsulating materials suitable as *"food grade enteric coating"*.

In this framework, alginate beads have been used extensively in microencapsulation because they are extremely easy to prepare on a lab-scale, the process is very mild and it can be conducted in sterile environments (Tønnesen, H. H., & Karlsen, 2002). However, two major drawbacks limit the use of

such microcapsules in the food industry. First, as easy as it is to make small batch using a syringe extruder and a stirred calcium bath, the scaling up of the process is not always very easy. Secondly, the microcapsules thus obtained are porous and allow fast and easy diffusion of water and other fluids in and out of the alginate matrix. This might be a advantage for the immobilization of live cells and enzymes that are meant to be accessible to their environment, but is definitely a drawback when one is trying to protect or segregate an ingredient from its environment and achieve a longer shelf life than the unencapsulated homologues (Gouin, 2004). Moreover, most of the plants for the production of alginate beads are currently optimized for beads filled with a hydrophobic dispersed phase, which is a major limiting factor in food applications, since most useful bioactives are not liposoluble. The present *chapter* describes the development and application of a new co-extrusion device for formation of beads as carrier for hydrophilic compounds. In principle, an aqueous core, enclosed by a well-defined external alginate shell, can be obtained by coextruding the two phases in a concentric laminar flow column, splitting the latter into drops by a mechanical rupturing by the blades of a rapidly rotating fan, and rapidly gelling the external polymer phase before interdiffusion with the internal phase takes place. A preliminary investigation on the capsule's effective release/retention of cyanocobalamin, a common vitamin of the vitamin B_{12} family will be also presented. The main goal is to design and develop a process facilitating the large-scale production of alginate beads, which makes it possible to envision a commercial encapsulated food ingredient based on the alginate bead technology.

2.2. MATERIALS AND METHODS

2.2.1. Chemicals

The ability to produce beads using an experimental encapsulation device was tested using solutions of the following sodium alginates as wall materials: Algogel 6020 (Cargill Inc., France) and Sodium alginate RPH (Carlo Erba Reagenti s.p.a., Italy). Sterile solutions of these alginates were prepared by dissolving solid Na^+-alginate in the desired volume of water, containing 0.02% (w/w) sodium azide to prevent microbiological growth. Commercial Olive oil and an aqueous solution of glucose syrup (40:60 w/w) were used as different filler materials. Glucose syrup (C* Sweet M 01621, D.E. 59-64) was provided by Cargill srl Rovigo. Reagent-grade sodium nitrate, calcium chloride and cyanocobalamin were purchased from Sigma Aldrich.

2.2.2. Materials characterization

H-NMR spectra of alginates: $_1$H NMR spectra were acquired on a Bruker Avance 500 spectrometer (Bruker, Karlsruhe, Germany). The Na^+-alginates samples were dissolved in D2O (3% w/v) and dried several times prior to NMR spectrum acquisition. The $_1$H spectra were recorded at a temperature of 70°C, a sweep width of 5999.7 Hz, an 90° pulse, and an acquisition time of 2.048 s. Typically, 32 or 128 repetitive scans were acquired and the data were processed with a line broadening of 0.3 Hz before Fourier transformation. Multiple-peak deconvolutions were performed with the software XWIN-NMR 3.5. Peak assignments and calculations of M/G ratio and the fractions of diad sequences (MM, GG and GM/MG) were performed as described by (Grasdalen *et al*,1983) .

Molecular weight (Mw) and polidispersity index (P.I.) of the alginates: The average molecular weight (M_w) of alginates was determined by size exclusion chromatography with multiangle light scattering (SEC-MALS) using two columns (TSK gel GMPWXL, Tosoh, 7.8mm ID x 30cm, Viscotek) in series as well as a differential refractive index detector, four-capillary differential viscometer and a low angle light scattering detector (Viscotek mod. 302 TDA). The mobile phase was 0.1 M $NaNO_3$ at a flow rate of 0.6 ml/min. Data were analyzed using OMNISEC 3 software.

Rheological measurements: to describe the rheological behaviour of the alginate solutions and of the different fillers, steady shear rheological data were obtained with a rheometer (SR-5000, Rheometric) using a double couette geometry with a gap of 1mm. Steady shear data were obtained over a shear stress range of 0.01-100 Pa at 23°C.

Surface tension measurements: The surface tension of the alginate solutions and of the different fillers was determined by means of the Wilhelmy balance technique using a contact angle tensiometer (DCA-

100, FTA Europe Ltd, Cambridge, UK). Each experiment was repeated five times to obtain an averaged surface tension value at 23°C.

2.2.3. Co-extrusion device

The alginate solution and the filler phase were simultaneously pushed by peristaltic pump (Velp Scientifica srl, Milan) from the glass containers to the co-extrusion nozzle (Nisco Engineering AG, Zurich). An home made jet cutter, made of plastic material and several cutting wires, was used to cut the solid liquid jet into uniform cylindrical segments. The final gelation of the microbeads was obtained by ionotropic reaction with calcium chloride (0.1-1M in distilled water). All studies were performed at 23°C.

2.2.4. Beads size measurements

The size of polymerized alginate bead has been determined by Image Analysis. Bead samples were applied to a microscope slide and examined microscopically. The size measurements were determined by connecting a digital camera (Cyber-shot DSC-W70, Sony, China) to a microscope (D Laborlux Leitz, Germany). The camera was interfaced to a PC operating with Image Pro Plus 6.2 (Media Cybernetics, USA). Determination of the size distribution was performed on at least 100 measurements.

2.2.5. Mechanical properties

To investigate the macroscopic mechanical properties of alginate microbeads, five capsules were placed side by side under parallel plate geometry and then subjected to uniaxial compression tests using a texture analyzer TA (XTplus, Stable Micro System, England) operating at T = 23°C. To eliminate any effect due to the non-ideal spherical shape, the samples are sandwiched between the upper and lower plates of the TA, and first pre-loaded with a stress of about 5 grams. Compression was performed at a constant speed of $V = 7.5$ mm min^{-1} from the initial height h_0, accurately measured after the pre-stress has been applied, up to rupture. To check for reproducibility, tests were repeated several times for each different sample.

2.2.6. Diffusional properties

In order to estimate the beads ability to be used for controlled release of small hydrophilic bioactive compounds, diffusion experiments were carried out using cyanocobalamin as simple probe. An aqueous solution of glucose syrup (40:60 v/v) and cyanocobalamin (0.03 mM) was prepared and used as filler phase in beads production. Afterwards 3g of beads were placed in a covered tube with 5 ml of distilled water at 25 or 80°C. Temperature control was provided by a thermostatically controlled bath. Diffusion of vitamin was quantified by measuring the absorbance in the surrounding medium at λ=361 nm (spectrophotometer Cary V Varian).

2.3. RESULTS AND DISCUSSION

2.3.1. Co-extrusion plant

A schematic representation of the major features of the lab scale apparatus we developed is shown in figure 2.1a. The alginate solution (2) and the filler phase (1) were simultaneously pushed by peristaltic pumps (3a-3b) to the coaxial nozzle (4), which consists of two sub-nozzles allocated in a coaxial way (fig. 2.1b). The core material is pumped into the inner nozzle while the alginate dispersion is pushed through the annulus, allowing true "core-shell" morphology of the beads. As the liquid stream exits the nozzle a rotating jet cutter consisting of several wires (5a-5b) processes the fluid to defined uniform cylindrical-shaped segments that, as a result of a complex balance between surface tension and viscous forces, become droplets while falling down. Finally the formed droplets are collected in a gelling bath (6) where the beads shell is hardened.

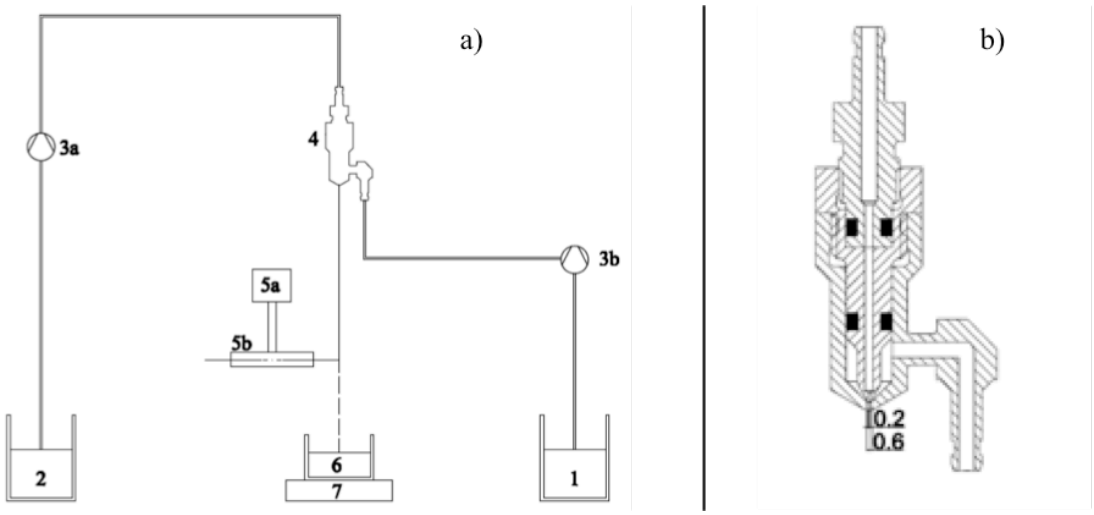

Figure 2.1 a) Schematic representation of the co-extrusion device. 1) filler solution supply 2) wall material solution supply 3) peristaltic pump 4) nozzle 5) jet cutter (a: engine b: rotating disc) 6) gelation bath 7) magnetic stirrer. And b) schematic representation of the co-extrusion nozzle

As already pointed out by Prüβe and co-workers (1998), for the production of PVA microparticles, in such a kind of process the height of the cutted cylinders and therefore the diameter of the resulting droplets (d_{bead}) depends on a number of parameters, namely the number *(z)* and the diameter of cutting wires (d_{wire}), the number of rotations of the cutting tool (n) and the mass flow (ϕ), the latter depending in turn both on the nozzle diameter (D) and on fluid velocity (v_{fluid}). In particular it has been shown that:

$$d_{bead} = \sqrt[3]{\frac{3}{2}D^2\left(\frac{v_{fluid}}{nz} - d_{wire}\right)} \qquad \textbf{(2.1)}$$

In our experiment the co-extrusion unit under study was designed to keep constant flow rates of the wall and core materials, as well as the nozzle (d_{int} = 0.2 mm and d_{ext} = 0.6 mm) and the jet cutter geometry. The mass flow ϕ and the number of rotations of the cutting tool n were adjusted in such a way that the liquid jet is not splashed off by contact with the rotating wires (z = 48, d_{wire} = 0.5 mm). This can in principle be achieved at very high v_{fluid} and very low n, however resulting in the formation of very big particles, being $d_{bead} \sim v_{fluid}/nz$. Moreover the higher the extrusion rate the higher the droplet velocity is, thus the probability of drops impacting each other upon contact with the $CaCl_2$

solution increases resulting in coalescence and loss of monodispersity or the formation of filaments (Serp *et al.,* 2000). An optimal configuration was found at $\phi \simeq 19$ ml min^{-1} and n = 400 rpm. The distance between the jet cutter and the gelling bath was set equal to 5 cm and kept constant for all the experiments.

The simplified model for the prediction of microbeads diameter as a function of processing parameters reported in eq 2.1 is however questionable since material's parameters such as viscosity, elasticity and surface tension can significantly contribute to the determination of particle shape and size (Chan *et al,* 2009). Moreover, the gelling properties of the shell material as well as the composition of the hardening bath are founded to be crucial for the production of microbeads with defined morphological properties (Chan *et al,* 2009). The latter observation become more important when using biopolymers which can display complex aging behaviour and heterogeneous dynamics effects upon gelation, as it is discussed in *chapter 1* for alginate. In a first part of this section a detailed study has been undertaken to investigate the effect of the alginate physical-chemical properties and of the gelling condition on the size and shape of alginate/alginate microparticles as well as on their mechanical properties, which can be critical in view of a final technological application. A second part of the work was focused on the optimization of the co-extrusion process for the production of microparticle containing an aqueous core enclosed by a well-defined external alginate shell. Finally, preliminary diffusional experiments were carried out to check the beads ability to be used for controlled release of small hydrophilic bioactive compounds.

2.3.2. Alginate selection

The precise composition of alginate varies markedly with season and seaweed species, with the result that the rheological properties and ability to extrude to form uniform drops and beads vary enormously from different suppliers and even from different batches from the same supplier. A detailed study has been undertaken to compare two commercially available alginates (Algogel 6020 and Alginate RPH) with respect to rheological behavior, molecular weight distribution, and potential for bead generation using the experimental encapsulation system. Table 2.1 summarizes the chemical composition, the average molecular weight and the polidispersity index (*PI*) of both alginates. Size exclusion chromatography yields a polymer number–averaged molecular weight $M_n \simeq 110$ kDa and $M_n \simeq 169$ kDa for Algogel 6020 and Alginate RPH respectively (corresponding to a degree of polymerization of about 560 and 855), and a weight–averaged molecular weight $M_w \simeq 330$ and $M_w \simeq 391$. Hence, both biopolymers display a quite large degree of polidispersity M_w/M_n between 2.5 and 3. H-NMR spectra showed a higher content of guluronic residues for Algogel 6020 ($X_G \simeq 0.52$) and so a higher affinity for cross-linking agents than Alginate RPH, for which $X_G \simeq 0.42$ (see table 2.2). Moreover, being the X_{GM+MG} weight fraction a little bit more in Alginate RPH than in Algogel 6020 ($X_{GM+MG} \simeq 0.30$ and 0.28 respectively), the former once gelled should evidence a higher shrinking together with an increased possibility to display partial network collapses. (Donati *et al*, 2005).

	Mn (kDa)	***Mw*** (kDa)	***PI***	d_p
Algogel 6020	110.675	328.312	2.966	559
Alginate RPH	169.34	391.719	2.313	855

Table 2.1 Polymer number-averaged molecular weight (Mn), weight averaged molecular weight (Mw), polydispersity index (*PI*) and degree of polymerization (d_p) for Algogel 6020 and Alginate RPH.

	X_G	X_{GG}	X_M	X_{GM+MG}	X_{MM}
Algogel 6020	0.56	0.26	0.44	0.30	0.14
Alginate RPH	0.42	0.14	0.58	0.28	0.30

Table 2.2 Mannuronic (X_M) and guluronic (X_G) weight fractions in Algogel 6020 and Alginate RPH, and weight fractions of the dimeric units X_{GG}, X_{GM+MG} and X_{MM}.

A flow curve for Algogel6020 for a given concentration (i.e. 2% w/w) is reported in the main body of fig. 2.2. As expected, due to the distribution of chain lengths, alginate solutions are not Newtonian and behave as pseudoplastic fluids. The stronger the shear stress the more chains are oriented and, hence, the lower the viscosity. The experimental curve is well fitted by using the Cross model (Cross, 1965), $\eta = \eta_\infty + [(\eta_0 - \eta_\infty)/(1+a\dot{\gamma}^m)]$, where η_∞ and η_0 are the infinity and zero shear viscosities, $\dot{\gamma}$ is the shear rate, a is the Cross time constant and m the rate constant. It could be useful to recall that in this equation $1/a$ gives us a critical shear rate that proves an indicator of the onset shear rate for shear thinning. An accurate analysis yields $1/a \simeq 0.31$ and $1/a \simeq 0.52$ for Algogel 6020 and Alginate RPH respectively, thus alginates with a narrow molecular weight distribution (i.e. low polidispersity index PI) show a more pronounced Newtonian rheology than alginates with a high PI (Serp *et al,* 2000). The insect of figure 2.2 reports the calculated η_0 values for both polymers at five different concentrations, ranging between 1 and 2% (w/w). The η_0 *vs [c]* dependence appears as a straight line in a double log plot, indicating a power law behavior $\eta_0 \sim [c]^n$ with a scaling exponent $n \simeq 3.6$ and $\simeq 3.1$ for Alginate RPH and Algogel 6020 respectively. The n values we determined are quite in agreement with previous finding (Lapasin and Princl, 1995) for which n typically varies as $[C]^{3.3}$, so that doubling the concentration gives about a tenfold increase in viscosity. A similar concentration dependence ($[C]^{3.75}$) has been predicted theoretically by de Gennes (1979) using the so-called scaling argument. The strong dependence of viscosity on *[C]* is well justified by the dominant role played by intermolecular interactions with neighbouring molecules, which proliferates as *[C]* increases. These physical circumstances, which may be explained by the entanglement concept (Graessly WW, 1974) or by the reptation theory (de Gennes, 1971), should scale with M_w explaining why we found n higher for Alginate RPH.

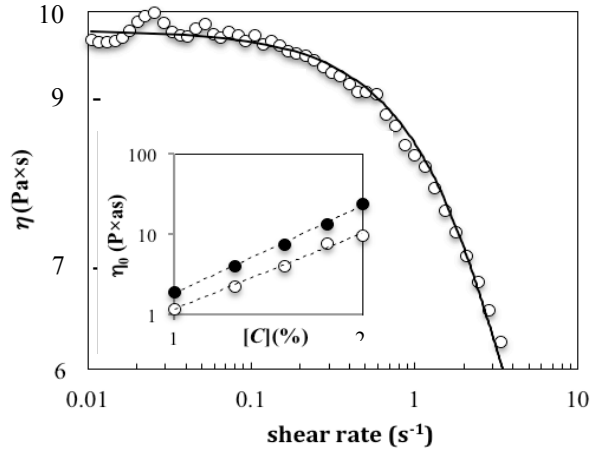

Figure 2.2 Main body: flow curve for a water solution of Algogel 6020. Solid line represents the fit according to the Cross model. Insect: zero shear viscosity η_0 dependence on alginate concentration [C] for Algogel6020 (empty circles) and AlginateRPH (filled circles)

Our results clearly show that the two tested alginates exhibit different rheological behaviors, and it would therefore be expected that the morphological and physical properties of the co-extruded microcapsules would be significantly different. Considering the higher processability and the higher affinity for calcium ions of Algogel 6020 with respect to Alginate RPH, the former has been chosen as optimal wall material.

2.3.3. Gelling condition

In a first series of extrusion experiment the gelling condition were optimized for the production of alginate/alginate microbeads (i.e. a 2% alginate solution was used as wall material and filler phase). In particular the incubation time in the gelling bath and the molarity of the cross-linking agent were considered. Let us first concentrate on the effect of the $CaCl_2$ molarity on the morphological and mechanical properties of the extruded microbeads. In these co-extrusion experiments the gelation time was arbitrarily chosen equal to 20 min, assuming *complete* gelation, and the nozzle-jet cutter distance was kept constant and equal to 15cm, ensuring that a uniform liquid jet reaches the jet cutter. The extruded alginate volume was $V_{alg} \simeq 10$ml, the gelling bath volume $V_{CaCl2} \simeq 230$ml and the molarity of the gelling agent was varied between 0.1 and 1M. Considering the fact that, for a given alginate concentration, the *g-equivalents* of calcium ions to be added to saturate theoretically all the carboxylic groups present in any alginate molecule is $n_{Ca^{++}} = 1/2 n_{NaAlg} d_p$ (Mancini *et al* 1999), it is not surprisingly to observe that the outer diameter of the obtained microbeads is almost independent from the counter ion concentration and $\simeq 0.65$ (data not shown). Indeed, for all the tested conditions the excess of Ca^{++} ions causes a complete saturation of the G-G residues and thus the complete formation of the capsules shell. Moreover, being the $[Ca^{++}]$ always exceeding $[COO^-]_{alg}$, the kinetic of gelation should not vary too much with the counter ion content. However it was already reported that an excess of gelling ions could influence the mechanical properties of the capsules, because of structural heterogeneity induced in the gel by the precipitation of the non-reactive salt fraction (Kuo and Ma, 2001). To investigate this possibility it could be useful to extract from the recorded mechanical profile (force/distance coordinates) a *"deformability index"*, defined as $\Delta F/\Delta d$ in the linear-elastic region, and the compression work up to rupture $W_b = \int F \, ds$, where F is the force and ds denotes the distance until maximum compression. In our analysis, in order to compare the mechanical data obtained from different batches both the deformability index and the compression work were normalized by the average weights of the beads and expressed in $Nmm^{-1}g^{-1}$ and $Nmmg^{-1}$ respectively. The insect of Fig 2.3 shows that $\Delta F/\Delta d$ slightly decreases from $\simeq 466$ $Nmm^{-1}g^{-1}$ at $[CaCl_2]$=0.1M to $\simeq 406$ $Nmm^{-1}g^{-1}$ when $[CaCl_2]$=0.5M, indicating more deformable capsules at higher counter ion concentration. The subsequent increases of the deformability index at $[CaCl_2]$=1M could be due to the absorption of non-reactive salt on the capsules surface. The fact that complex absorption phenomena can be related to the change in the mechanical properties is actually confirmed by the work at break (fig 2.3, main body), showing a value of $\simeq 82$ $Nmmg^{-1}$ when $[CaCl_2]$=0.1M followed by a *plateau* value $\simeq 50$ $Nmmg^{-1}$ for all the other tested calcium chloride concentration. Thus, in the limit $[COO^-]_{alg} << [Ca^{++}]$, the lower the counter ion concentration the higher the compression resistance. Considering the obtained results of $\Delta F/\Delta d$ and $\int F \, ds$, a solution containing 0.1M $CaCl_2$ was chosen as optimal cross-linking agent.

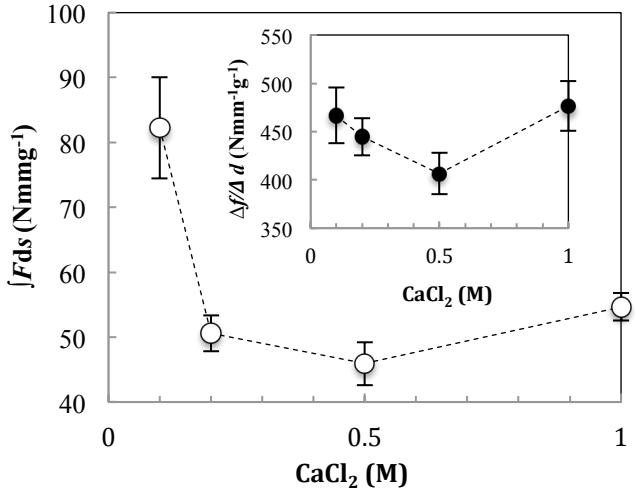

Figure 2.3 Calculated work at break ($\int F ds$, main body) and deformability index ($\Delta F/\Delta d$, insect) for alginate/alginate microbeads as a function of the molarity of the gelling agent ($CaCl_2$)

After choosing an appropriate Ca^{++} concentration (i.e. CaCl 0.1M) the influence of the gelling time was considered. In our experiments, the reaction times t_r was investigated in a range between 5 and 60 min. The main body of fig 2.4 shows the variation of the mean diameter as a function of t_r. Experimental results reveal that after an initial value ≃ 0.75 mm determined at t_r=5min, d_{bead} rapidly decreases to ≃ 0.65 mm when t_r=20min. Increasing the reaction time for longer times does not affect the dimension of the co-extruded microcapsules, indicating that a plateau value is reached. This evidence might be attribute to a complete saturation of the G-G blocks. The same conclusion can be drawn when considering the evolution of the mechanical properties with t_r. Indeed, the deformability index $\Delta F/\Delta d$, here presented in the insect of fig. 2.4, displays a very similar behavior, with a starting value of ≃735 $Nmm^{-1}g^{-1}$ at t_r=5min suddenly dropping at values closed to 470 $Nmm^{-1}g^{-1}$ when the reaction time reaches 20 minutes. The work at break calculated as previously described follows the same behavior an it was found ≃191 $Nmmg^{-1}$ at t_r=5min and ≃85 $Nmmg^{-1}$ at the plateau value. Thus, a gelling time of 20 minutes was judged the optimal condition for the next experiments.

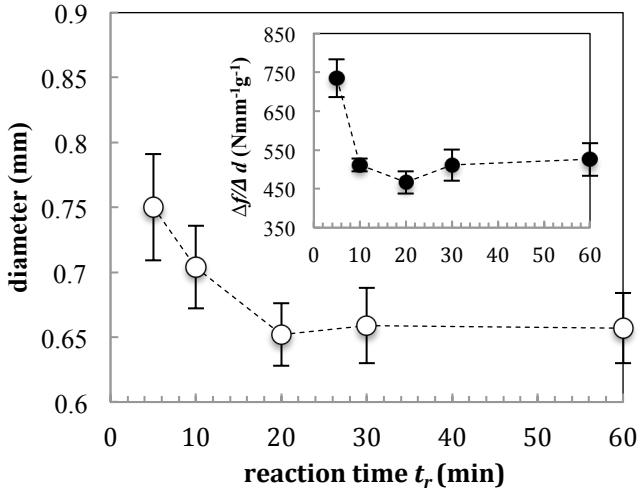

Figure 2.4 Calculated diameter and deformability index ($\Delta F/\Delta d$, insect) for alginate/alginate microbeads as a function of rection time t_r in the gelling agent ($CaCl_2$)

2.3.4. Process optimization for the production of alginate/liquid core microcapsule

In a further series of experiments, the extrusion process was optimized to produce beads to be used as carriers for olive oil or for an hydrophilic phase (glucose:water 60:40 v/v). First of all, the solutions were characterized in term of viscosity η, surface tension γ and density ρ (see Table 2.3). As expected, both the selected filler materials behave as Newtonian fluids and η is constant over the entire range of γ tested, namely 81 and 160 mPas for the olive oil and the glucose solution respectively. The surface tension γ of the aqueous solution of alginate (2% w/w) was ≃ 59 mN/m, in good agreement with previous finding (Del Gaudio et al., 2005; Hershko and Nussinovitch, 1998). Being the alginate a hydrophilic polysaccharide, the low surface activity we found is not surprisingly. The glucose solution reports a surface tension very close to the one of alginate, i.e. ≃ 63 mN/m, while γ for the olive oil was found ≃ 32 mN/m.

	η (Pa×s)	γ (mN×m^{-1})	ρ (kg/m3)
alginate	9.59	58.6	1.008
oil	0.081	32.1	0.916
glucose/water	0.16	62.6	1.282

Table 2.3 Viscosity (η) surface tension (γ) and density (ρ) of alginate solutions (2%w/v), olive oil and solutions of glucose/water (60:40 v/v).

It is clear that in view of an optimization of our co-extrusion process, where an inner jet consisting of olive oil or glucose solution flows concentrically to an outer jet of alginate, the effect of materials surface tension and viscosity should be taken into account in determining the drop size and drop shape during cutting or impaction with the gelling agent. In particular it has already shown that, for a free falling jet under gravity, both η and γ significantly affect the natural surface-tension-driven breakup of the laminar jet (Christanti and Walker, 2001), which in turn is important in the jet-cutting process. Indeed, the main target of getting an uniform distribution of beads sizes, implies the jet cutter working with continuous fluid streams, i.e. below the break up length L. Blaisot and Adeline (2003), already reported that L depends, among other parameters, on the fluid velocity, which in turn is related to the mass flow and the nozzle geometry. In this work, since our co-extrusion unit under study was designed

to keep constant flow rates of down streams of both wall and core materials and since the nozzle geometry was kept constant too, the liquid jet stability was controlled by controlling the nozzle-jet cutter distance λ. When $\lambda < L$ the liquid exiting the nozzle is a continuous stream and the jet cutting process is optimal; on the contrary, if $\lambda > L$ the liquid jet is instable and possibly breaks-up before the cutting process, generating bigger and non uniform microcapsules. In the following experiments, λ was varied between 10 and 25 cm and its influence on the size and on the mechanical properties of the co-extruded beads was investigated.

As shown in fig 2.5, the diameter of alginate/alginate microbeads is constant and $\simeq$ 0.6 mm up to $\lambda = 20$cm whereas a slight increase in d ($\simeq$ 0.8 mm) is observed for values of cutting distance equal to 25cm. The same trend is recorded for alginate/oil and alginate/glucose co-extruded microbeads, even if in those samples the critical length causing an increase in the droplet diameter is lower and equal to 20cm. The sharp augment of the diameter is particularly visible in microbeads containing an hydrophobic core, for which the d value changes from $\simeq$ 0.7mm at $\lambda = 15$cm to $\simeq$ 2.6mm when $\lambda = 20$cm, suggesting a transition between a continuous flow and a perturbed liquid jet. These experimental evidences can be tentatively explained considering the fact that, for an homogeneous Newtonian liquid jet, the break up-length is directly related to the Weber and the Ohnesorge number, $L \sim We^{0.5}(1+Z)$ (Man *et al*, 1998). Here $We = 2\rho R_j V_j^2/\gamma$ and $Z = \eta/(2\rho R_j \gamma)^{0.5}$ where, ρ is the density, γ is the surface tension, η is the viscosity and R_j and Vj are the radius and the velocity of the liquid jet. Thus, the break up length is directly proportional to the viscosity and in inversion proportion to the surface tension. However, in our case the fluid is not homogeneous and the differences between the viscosities ($\eta_{out} - \eta_{inn}$) and the surface tensions ($\gamma_{out} - \gamma_{inn}$) of the inner and the outer phase should be considered. For an alginate/alginate flow these terms are $\simeq 0$, and the liquid jet is almost stable over the entire range of λ tested. Introducing an inner phase causes the liquid jet to become unstable. Surface tension differences seems to be the dominant (Furlani *et al*, 2011; Christanti and Walker, 2001); the higher $\gamma_{out} - \gamma_{inn}$ the shorter the break up length, as clearly demonstrated by the sharp increase of the diameter for the alginate/oil system. Considering the experimental results of figure 2.5 a nozzle-jet cutter distance between 10 and 15 cm should be chosen for all the tested systems.

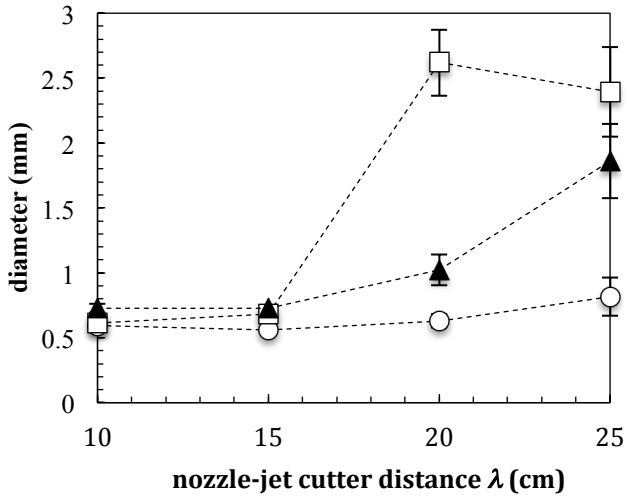

Figure 2.5 Calculated diameter for alginate/alginate (open circles), alginate/glucose solution (filled triangles) and alginate/oil (open squares) microbeads obtained as a function of the nozzle-jet cutter distance λ.

More insight on the optimal extrusion condition for the three different systems was obtained by measuring the mechanical properties of the extruded microbeads. As expected, the deformability index

$\Delta F/\Delta d$ reveals a higher resistance to compression when the encapsulated substance is hydrophobic, as in the case of olive oil (see fig 2.6). Moreover, $\Delta F/\Delta d$ increases with increasing the nozzle-jet cutter distance from 10 to 15 cm, with exception for the alginate/glucose beads for which the calculated values of $\Delta F/\Delta d$ are ≃ 177 $Nmm^{-1}g^{-1}$ at λ=10cm and about 105 $Nmm^{-1}g^{-1}$ when λ=15cm. The determined work at break follows the same trend (not shown). Thus, the optimal distance between the nozzle and the jet cutter was set equal to 15 cm or 10 cm for the production of alginate/oil or alginate/glucose microbeads respectively.

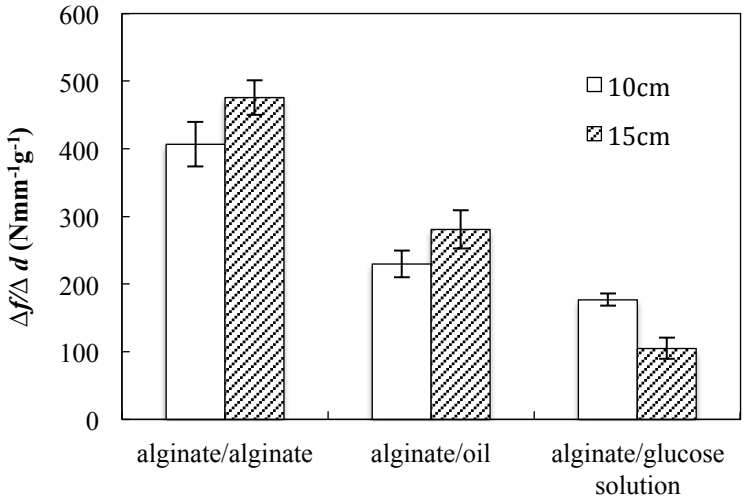

Figure 2.6 Hystograms of the calculated deformability index $\Delta F/\Delta d$ for alginate/alginate, alginate/oil and alginate/glucose solution (60:40v/v) co-extruded microbeads obtained for two different nozzle-jet cutter distances λ, namely 10 and 15 cm.

In the recent years, it has become a common trend to produce perfectly spherical Ca-alginate particles. The reasons could be to develop highly reproducible controlled release rates, which may be critical in some biomedical, pharmaceutical applications and physiological adsorption. Thus, the sphericity and the size distribution of the obtained microcapsule may play a crucial role in view of a final technological application. The shape of the obtained microcapsules can be well comprise by using a dimensionless indicator such as the aspect ratio *A.R.*, defined as the ratio between the major diameter d_{max} to the smaller diameter d_{min}, normal to the former. The aspect ratio varies from unity for a perfect sphere to approaching infinity for an elongated particle. Generally speaking, capsules are considered spherical if *A.R* <1.1 (Chan *et al.,* 2009). The size distribution can be evaluated by a coefficient of variation (*C.V.*), which is calculated by:

$$C.V. = 100\% \times \left(\sum_{i=1}^{N} \frac{(D_i - D_n)^2}{N-1} \right)^{0.5} \Big/ D_n$$

where D_i is the diameter of the *i-th* microsphere, N is the total number of the microsphere counted and D_n is the arithmetic average diameter. (Wang *et al*, 2011) Fig. 2.7 and fig 2.8 show the image and size distribution of Ca-alginate capsules with glucose syrup solution and olive oil as liquid core respectively. Both the prepared capsules are uniform and spherical, being *A.R.* = 1.05. The average diameter D_n is ≃ 0.76 for alginate/glucose microbeads, whereas is ≃ 0.7 for alginate coextruded with oil. The coefficient of variation *CV* was found 3.12% and 5.41% for alginate with hydrophilic or hydrophobic core respectively, indicating a narrow distribution of prepared Ca-alginate capsules and the possibility to effectively use them as carriers for bioactive compounds.

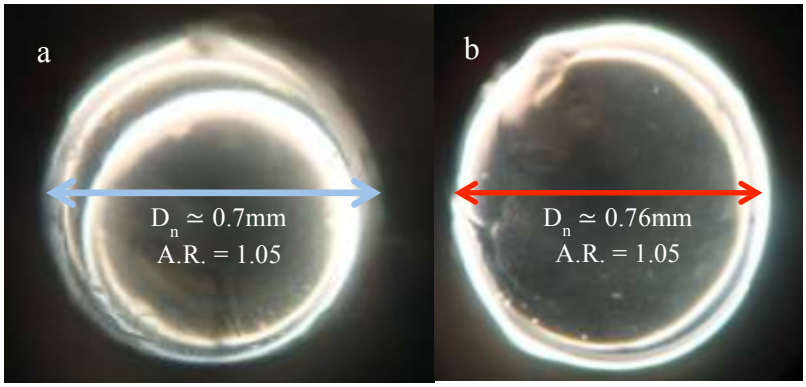

Figure 2.7 Optical images optained for alginate microbeads co-extruded with olive oil (a) and glucose/water solution (60:40 v/v) as filler phase. Values of mean diameter D_n and apparent radius *A.R.* are also reported.

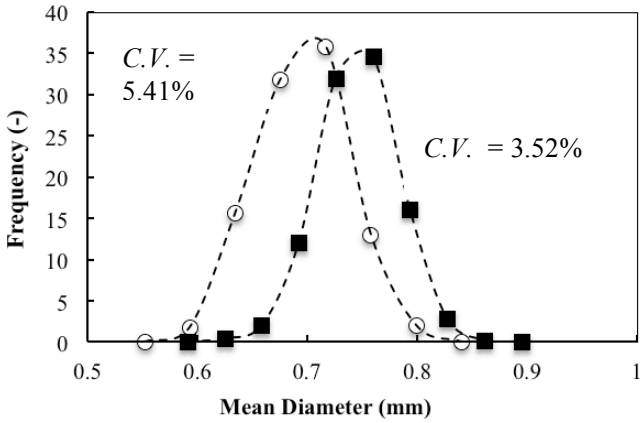

Figure 2.8 Size distribution for alginate/olive oil (open circles) and alginate/glucose solution (60:40 v/v) co-extruded microbeads. Calculated coefficients of variation (C.V.) are also reported.

2.3.5. Cobalamin diffusional properties from liquid core-alginate microsphere

As a final step of this work, in vitro release studies were carried out to test the potentiality of vitamin loaded alginate microbeads for technological application. An aqueous solution of glucose syrup (40:60 v/v) and cyanocobalamin (30 μM) was used as filler phase for beads production. The optimal operating conditions for the co-extrusion of alginate with an hydrophilic filler were used and the influence of two temperatures on the release behavior was investigated. Specific interactions of the drug with the biopolymer, such as hydrogen bonds and electrostatic interactions between cyanocobalamin and the alginate gels, were assumed negligible with respect to the osmotic pressure controlling the diffusion and release of the drug, allowing for the assumption of 100% drug release at long times. Figures 2.9(a) and 2.9(b) illustrate the drug release profiles from the alginate matrices at 80 and 25 °C respectively, plotted as a percentage of the released drug against time. As can be observed, the release at 80°C is much more rapid and is nearly 50% after 20 min; the same percentage of release at 25 °C has been reached after 20 days of storage.

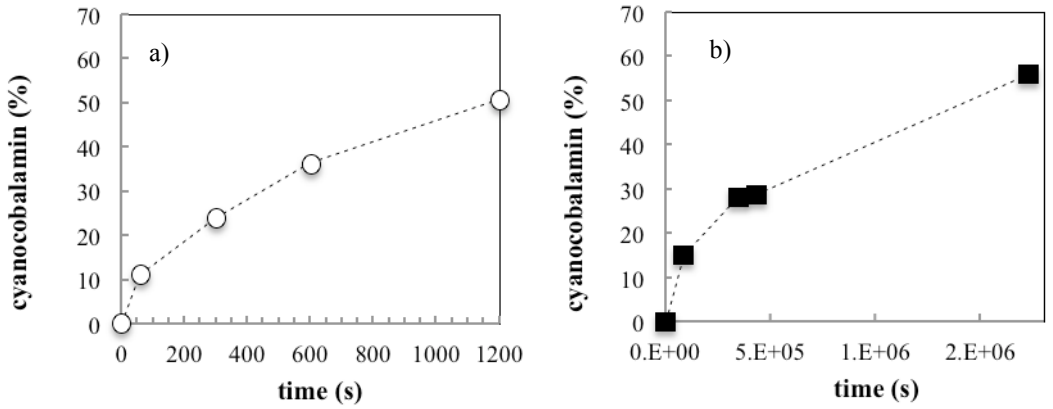

Figure 2.9 Cyanocobalamin release from alginate co-extruded microbeads in water at 80°C (a) and at 25°C (b) plotted against time

To determine the apparent diffusion coefficient (cm/s$^{0.5}$), D, of cyanocobalamin across the matrix, the quantity expressing the moles of drug released per unit area (mol/cm^2), *Q*, has been plotted against the square root of time (s$^{0.5}$) to determine *D* from the Q versus t$^{0.5}$ slope applying the Higuchi equation (Higuchi, 1967)

$$Q = 2C_0\sqrt{\frac{Dt}{\pi}} \qquad \textbf{(2.2)}$$

where C_0 is the initial molar concentration (mol/cm^3) of the drug in the matrix. In Figure 2.10, the profiles of drug released are plotted against the square root of time; the linear behavior confirms the Fickian diffusion release. Using the Higuchi equation, the diffusion coefficients are calculated to be $D_{80°C}$ = 6.35*10^{-9} cm/s$^{0.5}$ and $D_{25°C}$ = 4.51*10^{-12} cm/s$^{0.5}$. Note that *D* is very low, meaning a good retention of vitamin over time in the tested conditions. The release of vitamin is also temperature dependent and three orders of magnitude faster at 80°C, probably due to a partial swelling of the alginate shell at this temperature and a consequent increase in the mesh size of the polymer network.

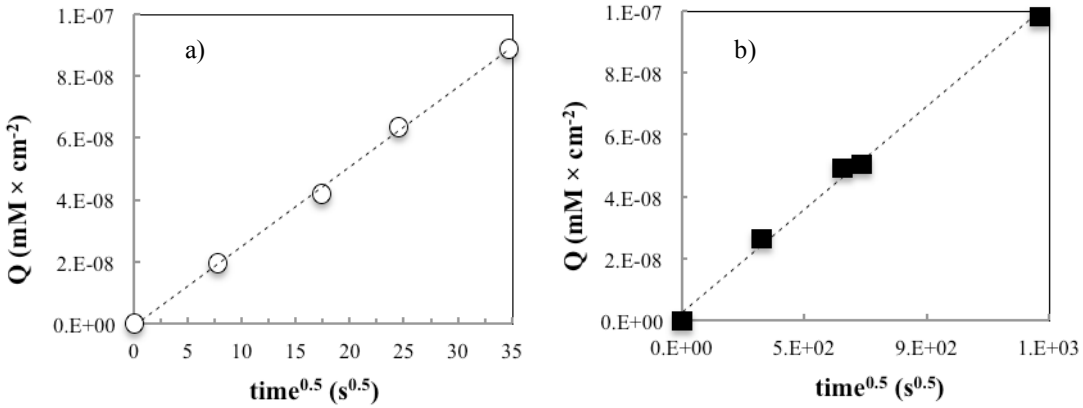

Figure 2.10 Millimoles released per unit area plotted against the square root of time for alginate co-extruded microbeads during diffusion in water at 80°C (a) and 25°C (b)

2.4. REFERENCES

1. Augustin M A and Hemar Y, 2009, Nano-and micro-structured assemblies for encapsulation of food ingredients. Chemical society reviews, 38(4): 902-912.
2. Augustin, MA, Sanguansri L, Margetts C, & Young B, 2001, Microencapsulation of food ingredients. Food Australia, 53(6), 220:223.
3. Benita S, 1998, Recent advances and industrial applications of microencapsulation. In Biomedical Science and Technology, Springer US, 17-29.
4. Blaisot JB, Adeline S, 2003, Instabilities on a free falling jet under an internal flow breakup mode regime. Int. J. of Multiphase Flow 29 629:653
5. Brazel CS, 1999, Microencapsulation: offering solutions for the food industry. Cereal Foods World, 44(6): 388-393.
6. Champagne CP and Fustier P, 2007, Microencapsulation for the improved delivery of bioactive compounds into foods. Current Opinion in Biotechnology,18(2): 184-190.
7. Chan ES, Lee BB, Ravindra P, Poncelet D, 2009, Prediction models for shape and size of ca-alginate macrobeads produced through extrusion–dripping method. Journal of Colloid and Interface Sci., 338 63:72
8. Chen L, Remondetto GE, Subirade M, 2006. Food protein-based materials as nutraceutical delivery systems. Trends in Food Sci. And Tech., 17(5) 272:283
9. Christanti Y, Walker L M., 2001, Surface tension driven jet break up of strain-hardening polymer solutions. J. Non-Newtonian Fluid Mech. 100 9:26
10. Cross MM, 1965, Rheology of non-Newtonian fluids: a new flow equation for pseudoplastic system. J. Colloid Sci. (20) 417
11. da Silva Malheiros P, Daroit DJ and Brandelli A, 2010, Food applications of liposome-encapsulated antimicrobial peptides. Trends in Food Science & Technology, 21(6): 284-292.
12. de Gennes PG, 1971, Reptation of a Polymer Chain in the Presence of Fixed Obstacles. J. Chem. Phys 55, 572
13. de Gennes PG, 1979, Brownian motions of flexible polymer chains. Nature 282, 367-370
14. Del Gaudio P, Colombo P., Colombo G., Russo P., Sonvico F., 2005, Mechanisms of formation and disintegration of alginate beads obtained by prilling. Int. J. Pharm. 302, 1.
15. Desai KGH, & Jin Park H, 2005, Recent developments in microencapsulation of food ingredients. Drying Technology, 23(7): 1361-1394.
16. Dinsmore AD, Hsu MF, Nikolaides MG, Marquez M, Bausch AR and Weitz DA, 2002, Colloidosomes: selectively permeable capsules composed of colloidal particles. Science, 298(5595): 1006-1009.
17. Donati I, Holtan S, Mørch Y**,** Borgogna M, Dentini M and Skj°ak-Bræk G, 2005, New Hypothesis on the Role of Alternating Sequences in Calcium−Alginate Gels. Biomacromolecules. 6:1031–1040.
18. Furlani EP, Delametter CN, Chwalek JM, and Trauernicht D, 2011, Surface Tension Induced Instability of Viscous Liquid Jets. In Technical Proceeding of the Fourth International Conference on Modeling and Simulation of Microsystems (April 2001).
19. Gibbs F, Kermasha S, Alli I, Catherine N, Mulligan B, 1999, Encapsulation in the food industry: a review. International Journal of Food Sciences and Nutrition, 50(3): 213-224.
20. Gouin S, 2004, Microencapsulation: industrial appraisal of existing technologies and trends. Trends in food science & technology, 15(7): 330-347.
21. Graessley WW, 1974, *The entanglement concept in polymer rheology* (pp. 1-179). Springer Berlin Heidelberg.
22. Grasdalen H, 1983, High-field,< sup> 1</sup> H-NMR spectroscopy of alginate: sequential structure and linkage conformations. *Carbohydr.Res.*,118:255–260.
23. Hershko V, Nussinovitch A, 1998, The behavior of hydrocolloid coatings on vegetative materials. Biotechnol. Prog. 14, 756.
24. Higuchi WI, 1967, Diffusional models useful in biopharmaceutics. Drug release rate processes. J.

Pharm. Sci. 56 315:324.
25. Kim HHY and Baianu IC, 1991. Novel liposome microencapsulation techniques for food applications. Trends in Food Science & Technology, 2: 55-61.
26. King AH, 1995, Encapsulation of food ingredients. Encapsulation and controlled release of food ingredients. Am Chem Soc. Washington, DC (USA): American Chemical Society, 26-39.
27. Kondo T, 2001. Microcapsules: their science and technology part III. Industrial, medical, and pharmaceutical applications. Journal of Oleo Science,50(3): 143-152.
28. Kris-Etherton PM, Hecker KD, Bonanome A, Coval SM, Binkoski AE, Hilpert KF, et al., 2002, Bioactive compounds in foods: their role in the prevention of cardiovascular disease and cancer. The American journal of medicine, 113(9):71-88.
29. Kuo CK, Ma PX, 2001, Ionically crosslinked alginate hydrogels as scaffolds for tissue engineering: part 1. Structure, gelation rate and mechanical properties. Biomaterials, 22(6) 511:521.
30. Lapasin R, & Pricl S. (1995). Rheology of polysaccharide systems. In Rheology of Industrial Polysaccharides: Theory and Applications (pp. 250-494). Springer US.
31. Lopez-Rubio A, Gavara R and Lagaron JM, 2006, Bioactive packaging: turning foods into healthier foods through biomaterials. Trends in Food Science & Technology, 17(10): 567-575.
32. Madene A, Jacquot M, Scher J and Desobry S, 2006. Flavour encapsulation and controlled release–a review. International journal of food science & technology, 41(1): 1-21.
33. Mancini M, Moresi M and Rancini R, 1999, Mechanical properties of alginate gels: empirical characterisation. J. Food Eng., 39(4):369–378.
34. Müller R, Mäder K and Gohla S, 2000, Solid lipid nanoparticles (SLN) for controlled drug delivery–a review of the state of the art. European journal of pharmaceutics and biopharmaceutics, 50(1): 161-177.
35. Mun R.P, Byars JA, Boger DV, 1998, The effects of polymer concentration and molecular weight on the breakup of laminar capillary jets. J. Non-Newtonian Fluid Mech., 74 285:297
36. Poncelet D, Teunou E, Desrumaux A and Della Valle D, 2002, Emulsification and microencapsulation: State of art. Landbauforschung Völkenrode, SH241, 27-31.
37. Prüβe U, Fox B, Kirchhoff M, Bruske F, Breford J, and Vorlop KD, 1998, New Process (Jet Cutting Method) for the Production of Spherical Beads from Highly Viscous Polymer Solutions. Chem. Eng. Technol., 21(1) 29:33
38. Saupe A and Rades T, 2006, Solid lipid nanoparticles. In Nanocarrier Technologies. Springer Netherlands, 41-50
39. Senuma Y, Lowe C, Zweifel Y, Hilborn JG and Marison I, 2000, Alginate hydrogel microspheres and microcapsules prepared by spinning disk atomization. Biotechnology and bioengineering, 67(5): 616-622.
40. Serp D, Cantana E, Heinzen C, von Stockar U, Marison IW, 2000, Characterization of an Encapsulation Device for the Production of Monodisperse Alginate Beads for Cell Immobilization. Biotechnology and Bioengineering. 70(1) 41:53.
41. Skurtys O, and Aguilera JM, 2008, Applications of microfluidic devices in food engineering. Food Biophysics, 3(1): 1-15.
42. Taylor TM, Weiss J, Davidson PM and Bruce BD, 2005, Liposomal nanocapsules in food science and agriculture. Critical Reviews in Food Science and Nutrition, 45(7-8): 587-605.
43. Tønnesen HH. and Karlsen J, 2002, Alginate in drug delivery systems. Drug development and industrial pharmacy, 28(6), 621-630.
44. Versic RJ, 1988, Flavor encapsulation. Flavor Encapsulation, 1-6.
45. Wang JY, Jin Y, Xie R, Liu JY, Ju XJ, Meng T, Chu LY, 2011, Novel calcium-alginate capsules with aqueous core and thermo-responsive membrane. Journal of Colloid and Interface Science, 353 61:68

3. ALGINATE MICROBEADS FUNCTIONALITY: APPLICATION IN A SMALL INTESTINE MODEL AND PROTECTION OF PROBIOTIC VIABILITY IN GASTRIC CONDITIONS

2. Alginate microbeads functionality

3.1. INTRODUCTION

As an answer to the increase in health related diseases, over the last decades the interest of food technology to provide consumers with safe food products and to use technological developments to engineer a new range of foods that will improve health is exponentially increasing (Foster and Norton 2009). In this framework, one of the major challenge for food scientist is to create new formulated ingredients able not only to deliver active molecules with advanced health benefits but also functionality through their structure (Norton *et al* 2006). Some of the possibilities include designing stimuli-responsive drug delivery systems that can undergo suitable changes in response to specific environmental fluctuations or imposed variations of control parameters. Although many types of stimuli have been considered most of the literature has focused on temperature and pH (Schmaljohann, 2006). The latter in particular, due to the fact that it changes naturally within the human body, can be considered as an ideal self-regulatory stimulus capable of directing the response of the carrier to a defined tissue or cellular compartment. (Langer,1990; Kost and Langer, 2001). Therefore, it is not surprising that nowadays most of the scientist deals with design pH triggered functional structure. To name two examples, in recent years biopolymer systems able to self-structure to provide advanced satiety control and controlled delivery of nutrients were designed by Foster and Norton (2009), whereas food-grade lyotropic liquid crystals capable of responding to pH variations with a reversible switch in both the structure and physical properties were designed by Negrini and Mezzenga in 2011. When dealing with hydrogels, as in our work, pH is well established as a means to induce swelling/deswelling (Crowther *et al*, 1999; Gupta *et al,* 2002) thus potentially affecting the release behavior during the gastric-intestinal transition.

Although crucial to control the release during the gastro intestinal transition, a pH responsive formulation actually is not enough to claim the effective possibility to trigger the release of active ingredients, drugs, and pharmaceutical molecules in the gastrointestinal tract (high pH), while preventing premature release in the stomach environment (low pH). Indeed, besides the simulation of the chemical condition that can be found in the gastro intestinal tract, the digestive system characteristic movements can deeply affect the functional properties of these structures (Khanvilkar and others 2001, Chu *et al* 2009; Macierzanka *et al* 2009, Guyton and Hall, 2005). Therefore, in order to achieve the full potential offered by the latest developments in the field of food material science, a fundamental understanding of the behavior of food structures *in vivo* is required. Unfortunately *in vivo* experiment are note easy to be performed and, even if a number of simulated model have been proposed for the stomach, few are available for the other parts of gastro-intestinal tract (Blanquet *et al*, 2001; Mercuri *et al*, 2009). One of these prototypes was developed by Tharakan in 2008 at the department of chemical engineering of the University of Birmingham. This small intestine model (SIM), which is composed of an of an experimental rig that efficiently simulates the segmentation motion of the human small intestine, has been already utilized to study mass transport phenomena occurring in the lumen and their potential effect on the concentration of species available for absorption (Fonseca 2011). Authors found that, when segmentation motion was applied the mass transfer coefficient in the lumen side of the SIM increases up to a factor of 7 (Tharakan *et al*, 2010), thus confirming that the simulation of the characteristic movement of the digestive system is essential when studying release properties of functional foods.

In this section, the release properties of co-extruded alginate microbeads as carrier for vitamin B_{12} were tested in the small intestine model previously characterized by Tharakan and co-workers (2008). A detailed investigation on the effect of the application of two different double coating will be presented and, under the assumption of a pseudo-steady state diffusion, an overall mass transfer coefficient will be calculated. Finally, functionality of alginate microbeads for protection of probiotic viability from gastric condition will be evaluated by using a modified bioluminescent *Bifidobacterium longum*.

3.2. MATERIALS AND METHODS

3.2.1. Chemicals

Alginate Algogel 6020 (Cargill Inc., France) was used as encapsulating material. Chitosan (medium molecular weight) was supplied by Sigma Aldrich and shellac flakes were kindly provided by Agar G.T.C. (Milan). Glucose syrup (C* Sweet M 01621, D.E. 59-64) was purchase by Cargill srl Rovigo and Actilight 950P (FOS) was provided by Giulio Gross s.p.a. (Milan). All the other reagents, unless otherwise specified were purchased from Sigma Aldrich.

3.2.2. Microbeads preparation

Different types of alginate microcapsules were produced using the experimental apparatus already described in chapter 2 of this manuscript. Process variables were kept constant throughout.

Alginate/cyanocobalamin microcapsules: Alginate microbeads containing a liquid core of cyanocobalamin were used to test the effect of encapsulation on the diffusional properties of the vitamin in a simulated model of small intestine (see section 3.2.3). The wall material consists of an alginate solution 2% w/v whereas an aqueous solution of glucose syrup (40:60 v/v) and cyanocobalamin (60 mM) was used as filler phase. To investigate the effect of double coating, chitosan coated calcium–alginate gel beads were obtained by transferring the primary alginate/cyanocobalamin capsules into chitosan solution (0.3% w/v in aqueous acetic acid solution 2% v/v, pH 5) for 30 minutes under mild stirring. In a similar way, shellac coated calcium alginate gel beads were obtained by immersion of the primary particle in ethanolic solution of shellac (15% w/v) for 30 minutes. Before diffusional experiment all the particles were collected by filtration and washed twice with 100 ml double-distilled water, consecutively.

Alginate/bifidobacterium microcapsules: In a second set of experiments we investigated the effect of encapsulation on the metabolic state of a probiotic bacterium under simulated gastric condition. Microcapsules preparation was performed using an alginate solution 2% w/v as wall material and a suspension of a modified luminescent *Bifidobacterium longum biovar longum* in FOS 2% as filler phase. Microcapsules were also prepared by simple co-extrusion (i.e. the wall material and the inner phase are the same) using a suspension of alginate 2% w/v, FOS 2% and the modified probiotic. Double coating of the primary capsules with chitosan was obtained as described above. Electro-competent *Bifidobacterium* cells were prepared in collaboration with the Microbiology group of the Department of Food Environmental and Nutritional Sciences of the University of Milan as described in Guglielemetti *et al* (2008).

3.2.3. Small–intestine model

The small intestine model (SIM) used in this work, schematically shown in fig 3.1, was designed and implemented by Tharakan (2008) in the School of Chemical Engineering at the University of Birmingham, UK. The SIM functions as a concentrically mass transfer exchanger composed of an inner semi-permeable RC membrane (Spectra/Por 7, MWCO 8000 Daltons, 32 mm of diameter, Medicell International Ltd London, UK) and an outer non-active and impermeable silicone transparent tubing (Flexible Hose Supplies, UK, diameter of 50 mm and wall thickness 3 mm). This dynamic *in vitro* model has a unique pneumatic mechanism to reproduce the characteristic segmentation movements responsible for the flow and mixing in the human small intestine. The SIM comprises by two independent and flexible compartments: the food or lumen side where digestion reactions take place and the recipient side where the products of absorption can be collected. The inner side or lumen of the SIM is represented by the semi-permeable dialysis membrane, with a characteristic length of 50 cm and 3.0 cm of diameter, whereas the outer or recipient side is represented by a transparent silicon tube (50 cm and a 5 cm of diameter). The flexible tubing allowed being deformed in a physiologically representative manner (Tharakan, 2008). Two types of flow are seen in the small intestine: a peristaltic flow, generated in the SIM using a variable peristaltic pump (Watson-Marlow, 323S/D), and a local segmentation flow, generated in the SIM by squeezing the tube. Segmentation contractions in the SIM were produced by inflation and deflation of two inflatable rubber cuffs (from an Omron Blood Pressure monitor) around the wall of the intestinal rig. When the cuff was fully inflated the external

wall of the SIM was compressed and occluded, generating mixing and propulsion of the lumen content. On the contrary, when the cuff was deflated relaxation of the membrane was produced. In the SIM, inflation was induced by supplying pressurized air into the cuff whereas deflation was attained by applying vacuum. The airflow and vacuum were controlled by solenoid valves (Burkert W2YLE, Germany) fixed on a control panel. The opening or closing of the solenoid valves was automatically controlled by a programmable logic controller (PLC, National Instruments NI USB-9162) connected to a computer by National Instruments NI- DAWMAX software. A pressure indicator (Sunx: DP2-42E) was used to monitor the rate at which the cuff was inflated by the compressed air.

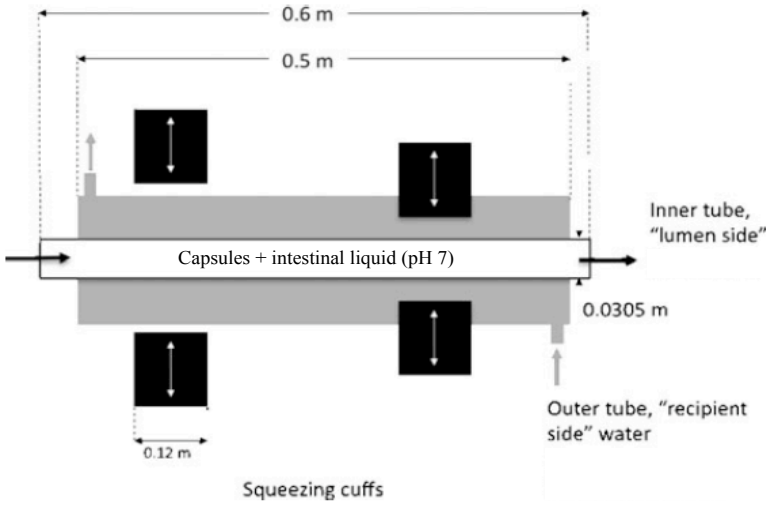

Figure 3.1 Schematic diagram of the small intestine model (SIM) implemented at the University of Birmingham and used in this work. Reprinted and modified from Tharakan *et al*, 2010

3.2.3. Diffusion experiments in SIM

Microspheres (2 g) were placed in 650 mL of simulated intestinal fluid (SIF) pH 7 and placed in the lumen side of the small intestine model, where they remained in agitation for 2.5 hours at 23°C. Flow through the inner tube was 1.87×10^{-3} m^3s^{-1}, giving an average velocity of 0.016 m/min, representative of that induced by peristalsis in the lumen side of the small intestine (Ganong, 2005) The 2 cuffs were inflated alternatively with a 2 s inflation time, 2 s deflation time, 2 s delay, and 0.5 *barg* inlet air pressure to simulate typical segmentation motion. The simulated intestinal fluid at pH7 was prepared as described in USP XXIII (1995). Aliquots of 1.0 ml were taken every 30 minutes in the recipient side (deionized water, 1L) and vitamin B12 content was measure by electrochemiluminiscence imunoassay (ECLIA) on a Roche Elecsys automatic analyzer (Roche diagnostic, Switzerland).

3.2.4. Metabolic state of encapsulated cells under simulated gastric condition

Microcapsules containing modified luminescent *Bifidobacterium* cells (1g) were placed in 50 mL of simulated gastric fluid pH3 (SGF) for three hours under mild agitation. The SGF containing 0.125 NaCl, 0.045M $NaHCO_3$, 0.007M KCl and pepsin 500 U/ml. Every 30 minute aliquots of 50 capsules were taken and the metabolic state of the cells was measured by light emission. Samples were dispensed in a 96-well white microtite plate in quadruplicate, immediately added of 150ml physiological solution and D-luciferin (250-µM, pH7) and finally measured for luminescence signal with a luminometer (VICTOR3, PerkinElmer Italia s.p.a.) under aerobic conditions. All bioluminescence measurements were performed at 37 °C in a constant mode and ensuring that the bacterial cells are at early-exponential growth.

3.3. RESULTS AND DISCUSSION

3.3.1. Cyanocobalamin diffusion in the small intestine model

In vitro release studies were carried out first to establish the influence of the wall material composition on the release behavior in SIM. Assuming the bulk fluid is well mixed on both food and recipient side one would expect uniform concentrations far away from the membrane, with a concentration boundary layer close to the membrane. Phenomena occurring can be visualized as follows (see fig. 3.2):

1. transport of solutes from the liquid core of the beads to the lumen side through the polymer shell of thickness X_1 (m), with diffusion coefficient D_1 (m^2/s)
2. transport through the boundary layer on the lumen side to the membrane surface of the SIM, described by a mass transfer coefficient, k_{lm} (m/s);
3. transport through the membrane of thickness X_2 (m), controlled by diffusion, with diffusion coefficient D_2 (m^2/s);
4. transport through the boundary layer in the recipient side, described by a mass transfer coefficient, k_r (m/s).

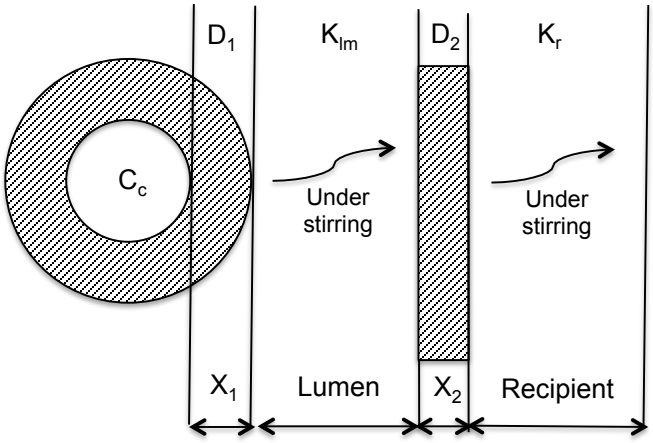

Figure 3.2 Phenomenological model for diffusion in the small intestine model

Figure 3.3 illustrates the drug release profiles from the different capsules, plotted as cyanocobalamin concentration in the recipient side of the small intestine (C_r) against time (t). As can be observed, the release from chitosan coated microbeads seems a little slower and after 2.5 hour is ≃ 1100 pg/mL; at this time, alginate microbeads and shellac coated microcapsules have released ≃ 1300 pg/mL. For all the tested samples concentration increases roughly linearly with time ($r^2 > 0.98$), and the mass flux across the membrane Q can be easily calculated as

$$Q = (\Delta C_r/\Delta t)\times[V_r/(2\pi r_m l_m)]$$

where V_r is the recipient volume, r_m is the membrane radius and l_m its length. We found $Q \simeq 1.9\times10^{-6}$ mmol/m^2s for chitosan coated microbeads, whereas no significant difference were seen for shellac coated microbeads and alginate capsules ($Q \simeq 2.13\times10^{-6}$ mmol/m^2s). Thus, vitamin release seems to be directly related to the coating solubility. Indeed, chitosan is insoluble at pH 7 (Pillai *et al*, 2009) whereas shellac starts to dissolve around pH 6.8 (Limmatvapirat *et al*, 2004). In a previous work on the small intestine model, Tharakan and coworkers (2010) calculated the mass flux across the membrane for non encapsulated riboflavin. They found a value of $Q = 5.32\times10^{-5}$ mmol/m^2s. Considering no specific interactions of the drug with the membrane of the SIM and even taking into account that the overall mass transport should scale as *1/d*, the fact that Q for riboflavin is ≃ 27 times faster than the value we found for cyanocobalamin suggests the effectiveness of our encapsulation system. The

constant mass flux we see can be taken into account by assuming a pseudo steady state. Under this assumption, the authors already mentioned above showed that an overall mass transfer coefficient K (m/s) can be calculated as

$$K = Q/(C_{lm} - C_r)$$

where C_{lm} and C_r are the concentrations in the lumen and the recipient side respectively. Unfortunately in our experiment only C_r is measured and C_{lm} cannot be quantified over time, being directly related to the vitamin diffusivity (D_I) through the polymer shell of the capsules.

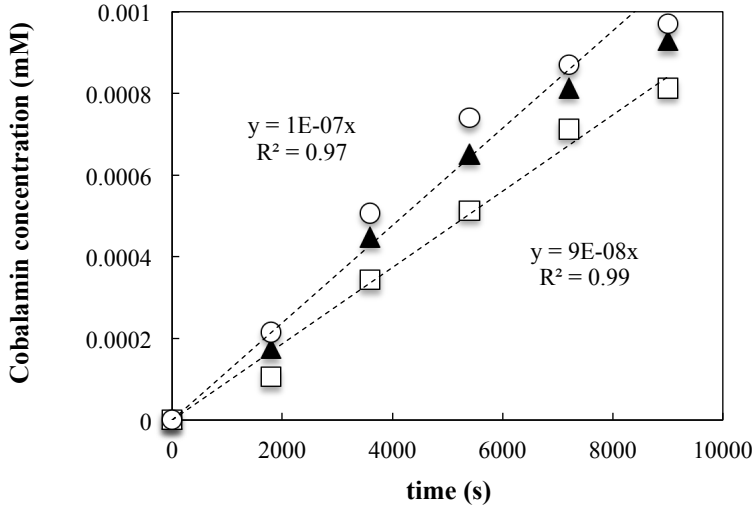

Figure 3.3 Cyanocobalamin concentration in the recipient side against time for intestinal fluid under segmentation motion showing linearity. Error bars are tipically smaller than marker size.

More insight on the diffusion behaviour of the different capsules we used in this work was obtained by diffusional experiment under simulated gastric conditions, pH 3. We determined the cobalamin concentration in the simulated gastric environment up to 5 hours. Results showed that for all the tested capsules a complete diffusion is observed at $t < 30$ min and the construction of release profiles was not possible. We conclude that when the pH is low the mesh size of all the polymers we tested increases and small molecules as cyanocobalamin cannot be retained, regardless the shell composition.

3.3.2. Metabolic state of *Bifidobacterium longum* under simulated gastric condition

The formulation of probiotics into microcapsules is an emerging method to reduce cell death during GI passage, as well as an opportunity to control release of these cells across the intestinal tract. The majority of this technology is based on the immobilization of bacteria into a heterogeneous polymer matrix, which is generally constituted of alginate and chitosan. In the next part of our work we will briefly show how, by using the same wall materials, co-extrusion technology can effectively increase the preservation of cell viability in gastric fluids.

Let us start by comparing the capsules immediately after the production process. In fig.3.4 the light emission curves for alginate microbeads obtained from simple extrusion or from the co-extrusion process, in presence or not of chitosan as double coating, are shown. As it is evident chitosan has a negative effect on the cell viability, as can be notice by the huge decrease of maximum light emission β_{max} in the double coated capsules, namely $\simeq$80%. This can be explained by considering that chitosan is basically a natural antimicrobial agent (Rabea *et al*, 2003). The co-extrusion process, which in principle allows the separation between the material used as double coating and the filler phase, seems to better maintain the *Bifidobacterium* viability, as clearly visible in fig 3.4. Thus, in the next series of

experiment, we focused our attention on the capsules produced by co-extrusion process.

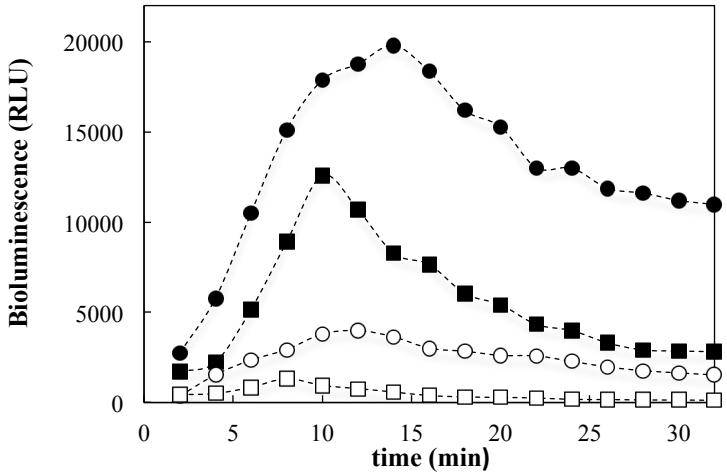

Figure 3.4 Light emission as a function of time of early log-phase B. Longum encapsulated in co-extruded alginate microbeads (filled circles), extruded alginate microbeads (filled squares), co-extruded alginate microbeads with a double coating of chitosan (empty circles) and extruded alginate microbeads with chitosan as double coating (empty squares)

In order to evaluate the suitability of co-extrusion technology for the protection of probiotics metabolic state under gastric condition, we employed bioluminescent *B. longum* for a quick test of the efficacy of different wall materials to preserve cell physiology under acidic conditions. It should be recall that, in such an experiment, the luciferase biosensor can monitor in real-time the physiological state of all cells, because it correlates sensitively to intracellular ATP (Guglielmetti *et al*, 2008). We incubated co-extruded capsules containing early-log phase cells of recombinant *B. longum* in simulated gastric fluid pH 3 for 3 h and then we measured the decrease in β_{max}. Values of β_{max} for unencapsulated *B. longum* and for the bioluminescent probiotic incubated in physiological solution were also determined for comparison. A first clear evidence that can be extracted from the luminometer measurements shown in the insect of fig 3.5 is that the bioluminescence $\beta_{max}(t)$ (made dimensionless by normalizing to its initial value) decays more slowly in presence of chitosan as double coating. For these capsules after 3 hours of incubation in SGF the bioluminescence loss is $\simeq$ 75% whereas at the same time capsules surrounded by a simple alginate shell loose $\simeq$ 98% and no cells viability is retained for unencapsulated *B. longum*. Thus, even taking into account that the co-extrusion process in presence of chitosan causes almost an 80% reduction of the initial value of bioluminescence, the effectiveness of encapsulation in preserving cell viability after three hours in simulated gastric fluid for double coated microsphere is $\simeq$2 times higher than the same value obtained for alginate co-extruded beads.

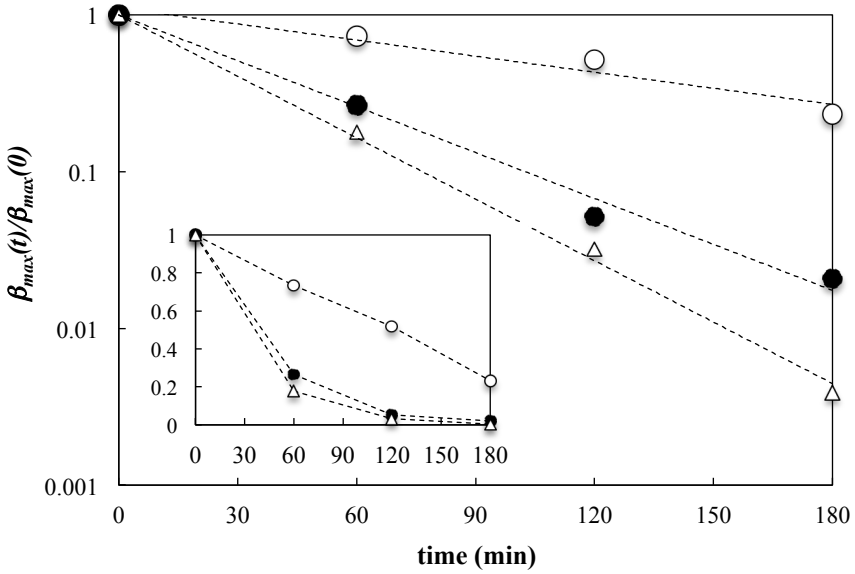

Figure 3.5 Insect: decay of $\beta_{max}(t)/\beta_{max}(0)$ as a function of incubation time in simulated gastric fluid of early phase *B. longum* encapsulated in co-extruded alginate microbeads (filled circles), co-extruded alginate microbeads with a double coating of chitosan (empty circles) and unencapsulated (empty triangles). Main body: same values plotted in a semi-log plot display a simple exponential decay. Here the dashed lines represent the fit of experimental data with $\beta_{max}(t)\sim exp\hat{}(-\lambda t)$ with r^2 always greater than 0.98

More insight on the β_{max} decay can be obtained by plotting the same values in a semi-log plot (fig. 3.5, main body). As it is ease to see, for all the tested samples the normalized bioluminescence displays a simple exponential decay

$$\beta_{max}(t)\sim exp^{-\lambda t}$$

where the decay constant λ increases from about 0.007 min^{-1} for the co-extruded capsules double coated with chitosan, to 0.022 min^{-1} for alginate co-extruded microcapsules and 0.03 min^{-1} for *B. longum* alone. A more intuitive description of this characteristic exponential decay can be given by the time required fore the bioluminescence to fall to one half of its initial value, $t_{1/2} = ln2/\lambda$. Accordingly, we obtained $t_{1/2} \simeq$ 99 min for alginate/chitosan co-extruded microcapsule, $t_{1/2} \simeq$31 min for the same capsules without double coating and $t_{1/2} \simeq$23 min for non encapsulated *B. longum*. Considering that in our experiment the emitted bioluminescence is directly proportional to the physiological state of cells, we can conclude that our co-extrusion technology, together with the presence of chitosan as double coating polymer, can effectively increase the preservation of probiotics cell viability in gastric environment. Further application of our encapsulation process in *in vivo* system can be found in Turroni *et al* (2013).

3.4 REFERENCES

1. Blanquet S, Marol-Bonnin S, Beyssac E, Pompon D, Renaud M, Alric M., 2001, The "biodrug" concept: an innovative approach to therapy. Trends Biotechnol 19(10):393–400.
2. Chu B-S, Rich GT, Ridout MJ, Faulks RM, Wickham MSJ, Wilde PJ, 2009. Modulating pancreatic lipase activity with galactolipids: effects of emulsion interfacial composition. Langmuir 25(16):9352–60.
3. Crowther HM, Saunders BR, Mears SJ, Cosgrove T, Vincent B, King SM, Yu GE, 1999, Poly (NIPAM) microgel particle de-swelling: a light scattering and small-angle neutron scattering study. Colloids Surf., 152: 327–333.
4. Fonseca MRJ, 2011, An Engineering Understanding of the Small Intestine. PhD Thesis, University of Birmingham.
5. Foster TJ, Norton IT. 2009. Self-assembling structures in the gastrointestinal tract. In: Mc-Clements DJ, Decker EA, editors. Designing functional foods: measuring and controlling food structure breakdown and nutrient absorption. Oxford: Woodhead Publishing Limited. p 601–22.
6. Ganong W, 2005, Review of medical physiology. NY, U.S.A: McGraw-Hill.
7. Guglielmetti S, Ciranna A, Mora D, Parini C, Karp M, 2008, Construction, characterization and exemplificative application of bioluminescent *Bifidobacterium longum biovar longum.* International Journal of Food Microbiology, 124: 285–290
8. Gupta P, Vermani K, Garg S, 2002, Hydrogels: from controlled release to pH-responsive drug delivery. Drug Discovery Today, 7: 569–579.
9. Guyton AC, Hall JE. 2005. Textbook of medical physiology. 11 ed. Saunders.
10. Khanvilkar K, Donovan MD, Flanagan DR., 2001. Drug transfer through mucus. Adv Drug Deliv Rev 48(2-3):173–93.
11. Kost J, Langer R, 2001, Responsive polymeric delivery systems. Adv. Drug Delivery Rev. 46: 125–148.
12. Langer R, 1990. New methods of drug delivery. Science, 4976: 1527–1533.
13. Limmatvapirat S, Limmatvapirat C, Luangtana-anan M, Nunthanid J, Oguchi T, Tozuka Y,... & Puttipipatkhachorn S, 2004, Modification of physicochemical and mechanical properties of shellac by partial hydrolysis. International journal of pharmaceutics, 278(1), 41-49.
14. Macierzanka A, Sancho AI, Mills ENC, Rigby NM, Mackie AR, 2009. Emulsification alters simulated gastrointestinal proteolysis of beta-casein and beta-lactoglobulin. Soft Matter 5(3):538–50.
15. Mercuri A, Faulks R, Craig D, Barker S, Wickham M, 2009, Assessing drug release and dissolution in the stomach by means of dynamic gastric model: a biorelevant approach. J Pharm Pharmacol 61:A5.
16. Negrini R, Mezzenga R., 2011, pH-Responsive Lyotropic Liquid Crystals for Controlled Drug Delivery. Langmuir 27: 5296–5303.
17. Norton I, Fryer P, Moore S. 2006. Product/process integration in food manufacture: engineering sustained health. AIChE J 52(5):1632–40.
18. Pillai CKS, Paul W, & Sharma CP, 2009, Chitin and chitosan polymers: Chemistry, solubility and fiber formation. Progress in Polymer Science, 34(7), 641-678.
19. Rabea EI, Badawy MET, Stevens C. V., Smagghe G., & Steurbaut W., 2003, Chitosan as antimicrobial agent: applications and mode of action. Biomacromolecules, 4(6), 1457-1465.
20. Schmaljohann D, 2006, Thermo-and pH-responsive polymers in drug delivery. Adv. Drug Delivery Rev. 58: 1655–1670.
21. Tharakan A, 2008, Modelling of physical and chemical processes in the small intestine. PhD Thesis, University of Birmingham.
22. Tharakan A, Norton IT, Fryer PJ, and Bakalis S, 2010, Mass Transfer and Nutrient Absorption in a Simulated Model of Small Intestine. Journal of Food Science 75,6: 339-346.
23. The United States Pharmacopeia (1995), Unites States Pharmacopeial Convenction, Inc.,

Rockville, MD

24. Turroni F, Serafini F, Foroni E, Duranti S, O'Connell Motherway M, Taverniti V, Mangifesta M, Milani C, Viappiani A, Roversi T, Sanchez B, Santoni A, Gioiosa L, Ferrarini A, Delledonne M, Margolles A, Piazza L, Palanza P, Bolchi A, Guglielmetti S, van Sinderen D, Ventura M, 2013. Role of sortase-dependent pili of Bifidobacterium bifidum PRL2010 in modulating bacterium-host interactions. *PNAS* 110(27).

4. NANOPARTICLES FORMATION BY SOLVENT SHIFTING: UNDERSTANDING THE *OUZO EFFECT*

4. Nanoparticles formation by solvent shifting

4.1. INTRODUCTION

While trying to design a functional food, one should always keep in mind that the new product must be structured in such a way as to accomplish a specific function whilst being palatable enough to be eaten. If, as in our case, a bioactive compound must be released, the functional ingredient needs to alter its structure in response to an external environmental change such as in temperature or pH fast enough to be an efficient delivery carrier, but slow enough to preserve the structure during the tasting and perception process. The engineering of these properties is necessary and extremely challenging and clearly, can be obtained at multiple length scales. At nanometric level, hierarchical supramolecular assemblies based on hydrogen bonds or ionic interactions such as those used to design soft materials (Ikkala and Brinke, 2002; Antonietti *et al* 1994), could be an appealing strategy. With this approach, complex foods can be generated by self-assembly of simple food-grade components such as protein, polysaccharides and lipids, without need of covalent bonds, which could alter the food-grade nature of the assembly (Mezzenga *et al,* 2005). These types of nm-scaled dispersion have been shown to enhance the delivery efficiency and bio-viability (LaVan *et al*, 2003).

In this section we will discuss the possibility to produce polymeric particles by means of a spontaneous emulsification process, namely the *"solvent-shifting"*. Such a process is really attractive: it is spontaneous, mild, reproducible and gives rise to controlled monodisperse emulsion (Botet, 2012). Moreover, it does not require the use of surfactants, it is easy to be scaled up (Mitri *et al*, 2012) and appears deceptively simple: a hydrophobic solute is first dissolved into a polar solvent that is fully miscible with water, and then this solution is mixed with a large amount of water. The solution becomes a non-solvent for the hydrophobic molecules and instantaneously turns milky, because of the formation of small droplets strongly scattering the visible light. Only recently Vitale and Kantz (2003) analyzed in details this process and gave to it the name "*Ouzo effect*", due to the fact that such amazing phenomenon can be seen in everyday life upon dilution of some alcoholic drinks with water, as Ouzo in Greece and Pastis in France (Sitnikova et al, 2005; Grillo, 2003; Carteau et al, 2007; Scholten and van der Linden, 2008).

Up to know, most of the investigation efforts to understand the spontaneous emulsification, focus on the experimental phase diagram of ternary solutions as it is expected to give the key to control the entire process. Two parts of the diagram are already well known (Jones, 2002), namely the binodal and the spinodal line. The former separates the domain of parameters for which the equilibrated system is under a single homogeneous phase, from the domain for which several phases appear. The spinodal line instead separates the domain where the phase separation grows by nucleation, from the domain where the different pure phases appear spontaneously. It has already been shown that, in this general picture, the production of metastable dispersions or emulsions is limited to a small region of the composition map, called the Ouzo region, which is found somewhere between the binodal and the spinodal line at very high dilution (Ganachaud and Kantz, 2005). At present, the physical cause of this limitation is not understood.

The growing interest by scientist in the enormous potential of spontaneous emulsification is demonstrated by the exponential increase in the number of publications, as demonstrated by many papers (Mosqueira *et al*, 2000; Beck-Broichsitter *et al*, 2010; Mora-Huertas *et al*, 2011; Noriega-Peláez EK *et al*, 2011; Khayata *et al*, 2012; Bally *et al*, 2012). However, the fact that we do not understand yet the mechanisms leading to this kid of self-organized systems is a major drawback. Without such a knowledge, one can only proceed by *"trial-and-error"* to find the emulsification operating window.

In this chapter, we will first give the ternary phase diagram for a totally food grade polymer/solvent/non solvent system, obtained by using advanced optical techniques. Then, the possibility to produce polymer nanoparticles without any kind of mixing energy will be discussed. A first qualitative description of the physical phenomena governing the ouzo effect will be given and preliminary application will be presented too.

4.2. MATERIALS AND METHODS

4.2.1 Nano-precipitation process

Shellac flakes (kindly provided by G.T.C. s.r.l) were first dissolved in ethanol (analar Normapur) by stirring the flakes in the solvent for one night. The mass fraction of shellac dissolved in the solvent ranged from 2.5×10^{-4} to 3.8×10^{-2}. Then, fresh distilled milliQ water was poured quickly into the organic solution without any kind of stirring, in order to avoid shearing and breakup of the larger droplets formed by homogeneous nucleation. Prior to the nano-precipitation process, all solutions were filtered through 0.45 μm Millipore membrane filters into a dust free sample holders. The mass fraction of water was kept constant and equal to 5g. The amounts of organic solution and the mass fraction of shellac in the organic solution were chosen to reach the desired final mass fraction of shellac and solvent in the ternary system shellac/ethanol/water. These compositions are noted as f_p^i (initial mass fraction of shellac in ethanol), f_p (final mass fraction of shellac), and f_s (mass fraction of solvent in the final solution). The resulting dispersion was immediately analysed through light scattering, without removing the solvent.

4.2.2. Static, dynamic and depolarized light scattering

Static and dynamic light scattering were performed on undiluted dispersion at 25°C. The measurements used a 3D DLS spectrometer equipped with a 25mW HeNe laser operating at l=632.8 nm, a two channel multiple tau correlator and a variable-angle detection system (LS Instruments, Fribourg, Switzerland). The scattering cells (5mm quartz NMR cuvette) were immersed in an index matching bath of cis-decaline which does not change the polarization plane of the laser light. For static light scattering (SLS), the range of scattering vectors covered was $9\times10^{-3}\text{nm}^{-1} < q < 2.5\times10^{-2}\text{nm}^{-1}$. Measurements were made in an angular region from 40 to 140° with a step of 10°. Filtered toluene was used to calibrate the instruments. For the depolarized dynamic light scattering experiment (DDLS), two Glan-Thomson polarizers with extension coefficients higher than 10^{-5} were used in front of the detector to measure the depolarized scattered intensity. DDLS measurements were made in an angular region from 30 to 140° with a step of 5°, corresponding to scattering vectors between $7\times10^{-3}\text{nm}^{-1} < q < 2.5\times10^{-2}\text{nm}^{-1}$. In dynamic light scattering (DLS), the time correlation function of the scattered electric field was analysed with the cumulants method. Viscosity and refractive index of the continuous phases were deduced from tables according to the water/solvent content (Nowakowska, 1939).

4.2.3. Equilibrium phase separation

The binodal line is the equilibrium solubility limit of the polymer in the ethanol-water mixture. It was determined by titrating with water a solution of shellac in the solvent and by following the optical density at 600nm (spectrophotometer Cary V Varian). The composition at the binodal line was deduced from the mass of water added at the onset of turbidity (i.e. extreme increase in optical density, see fig. 4.4a).

4.2.4. Ouzo boundary

As proposed by Aubry at al. (2009) this boundary separates a region where solvent shifting produces nanoparticles only, from another region where it produces nanoparticles and bigger particles. This boundary can determined using filtration (to separate out the bigger particles) and light scattering (to detect the reduction in the number of particle). Briefly, for each dispersions the total scattered intensity was measured before and after filtration (pore size 0.45 microns) by using the 3D DLS instrument. The ratio of the two intensities (RI_s) was then plotted as a function of the final polymer mass fraction. An example is shown in figure 4.4b for two different mass fraction of solvent, namely 0.1 and 0.2. When $RI_s \to 1$ all particles passed through the filter and we can consider these compositions within the Ouzo range. For a given concentration RI_s decreases, indicating that bigger particle were removed by filtration. Roughly speaking this critical point can be taken as point of the Ouzo boundary.

4.3. RESULTS AND DISCUSSION

4.3.1. Turbid samples

Let us start with a brief, eye characterization of the produced dispersions. Fig 4.1 shows six different samples produced according to the nanoprecipitation process described in section 4.2.1. Here, the solvent mass fraction f_s is kept constant and equal to 0.2, whereas the final polymer mass fraction f_p^f varies between 1×10^{-3} and 5×10^{-3} from left to right. When f_p^f is very low, the produced dispersion is optically transparent whereas, as can be easily noticed by the milky-white colour, an augment of the final polymer mass fraction causes an increase in the turbidity of the suspension. These evidences clearly affect the scattering properties of our suspensions.

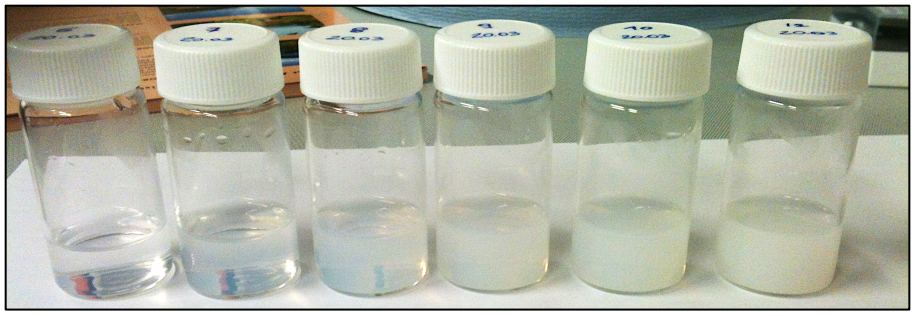

Figure 4.1 Different suspensions obtained by using the nanoprecipitation process. The mass fraction of solvent f_s is constant and the final mass fraction of polymer f_p^s is increasing from 1×10^{-3} to 5×10^{-3} from left to right.

Recalling basic theory, the light scattering properties of a sample can be classified in terms of the ratio of the mean free path, L_p of a photon (the average distance travelled by the photon in the medium before being scattered) to the size, L_s, of the sample (Pusey, 1999). For $L_p/L_s \gg 1$, the sample is transparent: most of the photons pass through the sample unscattered, some are scattered once, and the probability of double or higher-order multiple scattering is negligible. These samples are been proved to be well characterized by both static and dynamic light scattering (Berne and Pecore, 1976; Pecora, 1985; Chu, 1991). If $L_p/L_s \ll 1$, the sample is opaque like paint: typically a photon is scattered many times and the probability is negligible that a photon passes through the sample unscattered. Characterization of these samples progressed a lot in the last ten years by diffusing-wave-spectroscopy (DWS), where temporal fluctuations in light which has been scattered many times are measured (Maret, 1997). For $L_p/L_s \simeq 1$ the probabilities that a photon is not scattered, is scattered once, or is scatter a few times, are of comparable order of magnitude. Then, the sample can be called turbid, since appears cloudy, but one can still see through it. Lying awkwardly between the extremes of transparency (single scattering) and opacity (multiple scattering), turbid samples pose experimental and theoretical challenges. (Pusey 1999).

In our experiments, only for few samples $L_p/L_s \gg 1$. Moreover, most of the samples for which $L_p/L_s \ll 1$ presented macroscopic precipitation, and therefore were not analyzed. For all the other dispersions we prepared, $L_p/L_s \simeq 1$ and we used three-dimensional dynamic light scattering (3D-DLS) to suppress multiple scattering. 3D Cross correlation effectively suppresses the multiple scattering contribution from concentrated turbid samples by performing two simultaneous scattering measurements at the same scattering volume and same scattering vector and extracting only single scattering information common to both. Here we gave only a summary description of this technique (see figure 4.2) and we cite Pusey (1999) for a more detailed analysis.

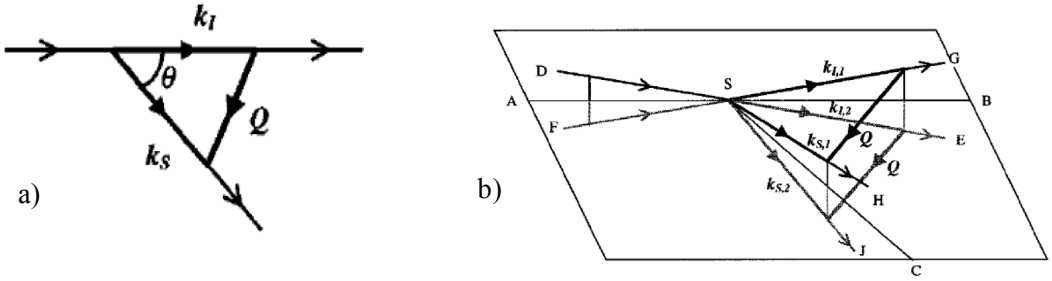

Figure 4.2 a) Normal one-beam light scattering. Incident light described by propagation vector k_I is scattered through angle ϑ. The scattered light is described by propagation vector k_s, ($|k_s| = |k_I| = 2\pi/\lambda$), and the scattering vector Q is defined by $Q = k_s - k_I$. b) Three-dimensional dynamic light scattering. The parallelogram represents the average scattering plane. Solid lines are above the plane, shaded lines below. The sample is situated at *S*. Illuminating beams of the same colour, *DE* and *FG*, originating above and below the average scattering plane, cross in the sample; *AB* represents the perpendicular projection of these beams onto the plane. The scattered beams *SH* and *SJ* project onto *SC*. The scattering angle ϑ is the angle between *SG* and *SH* and between *SE* and *SJ*. It is clear that the beam pairs *SG-SH* and *SE-SJ* define the same scattering vector *Q*. *(reprinted from Pusey, 1999)*

4.3.2. Particle size

In our experiment, the size of the nanoparticles in the final dispersion was measured systematically using 3D dynamic light scattering. Reproducibility was found to be better than 5% for all the tested samples. In dynamic light scattering a time correlation function (TCF) of the scattering intensity is measured which is given as

$$g_2(t,q) = \frac{\langle i(0)i(t)\rangle}{\langle i(0)\rangle^2} \qquad \textbf{(4.1)}$$

in which *i(0)* and *i(t)* are the scattering intensities at time $t = 0$ and at a certain delay time t. In dilute solutions $g_2(t,q)$ can be expressed in terms of the normalized electric field correlation function $g_1(q,t)$ using Siegert's equation

$$g_2(t) = 1 + \beta|g_1(t)|^2 \qquad \textbf{(4.2)}$$

where the coefficient β depends on the quality of the coherence. When monomodal fiber optics is used, β is close to the theoretical value of 1. In the case of a monodisperse system of particles and for short delay times $g_1(t)$ is well approximated by a simple exponential decay

$$g_1(t) = exp(-\Gamma(q)t) \;\; if \; \Gamma(q)t < 1 \qquad \textbf{(4.3)}$$

This decay time is related to an apparent mutual diffusion coefficient

$$\Gamma(q) = q^2 D_{app}(q,c) \qquad \textbf{(4.4)}$$

The double extrapolation of $D_{app}(q,c)$ to c=0 and q=0 gives the translation diffusion coefficient from which the hydrodynamic radius R_h is determined using the Stokes-Einstein equation

$$R_h = \frac{k_B T}{6\pi\eta_s D_{app}} \qquad \textbf{(4.5)}$$

with k_B, Boltzmann's constant, T, absolute temperature, and η_s, the solvent viscosity. For polydisperse systems, $g_1(t)$ is given by an integral equation

$$g_1(t) = \int_0^\infty G(\Gamma) e^{-\Gamma t}\, d\Gamma \qquad \textbf{(4.6)}$$

where G(Γ) is the normalized distribution function of the decay rates. A commonly used technique to analyze eq 4.6 is the method of cumulants, which is based on a series expansion of $ln(g_1(t))$:

$$\ln g_1(t) = -\bar{\Gamma} t + \frac{\mu_2}{2} t^2 + \frac{\mu_3}{3} t^3 + \cdots \qquad \textbf{(4.7)}$$

At q=0, the first cumulant yields the z average of the diffusion coefficient and the second cumulant is a measure of polidispersity (relative standard deviation, σ).
From a first view of the main body of figure 4.3, showing the variation of the mean particle diameter with the mass fraction of shellac in the initial solution (i.e. before adding water) for the shellac/ethanol/water system, one important observation can be drawn: the diameter of the obtained nanospheres increases with increasing the polymer mass fraction and follows the same trend when we increase the solvent concentration. If the former experimental evidence is expected and in accordance with the *nucleation-aggregation* model proposed by Aubry *et al* (2009), the reason why an augment in the quality of the solvent (i.e. higher f_s) causes the particle size to increase is actually hard to spot, following the general rules for a *nucleation-and-growth* process. Indeed, the *nucleation-and-growth* model predicts that the number of nuclei should vary rapidly with solvent quality, and therefore with the concentration of nonsolvent. Consequently, the mean particle diameter ought to become smaller at higher water additions, as it happens in our case. Moreover in nucleation and growth, as the number of nuclei varies exponentially with the supersaturation, one should expect higher solute concentrations to yield a much higher number of nuclei and therefore smaller particles (Dirksen and Ring, 1991). This is in contrast with our results. If we consider the *nucleation-aggregation* mechanism to be the main physical phenomenon governing the formation of nanoparticle by solvent shifting, the experimental evidence we see can be explained by taking into account polymer swelling. As ethanol is fully miscible with shellac and with water, particles made through solvent shifting should contain a fraction of solvent in equilibrium with solvent in continuous phase. The total amount of solvent in particles depends on the partition coefficient, K, and on the total mass fraction of solvent in the dispersion. As the partition coefficient is a thermodynamic constant, its value should be influenced neither by the initial mass fraction of PMMA nor by the initial mean particle diameter. Therefore, the total amount of solvent in particles and so the amount of the polymer swelling should be directly related to f_s; the higher f_s the higher the swelling and so the measured particles size.

More insight on the DLS data can be obtained by plotting the same values in a double log plot (fig. 4.3, insect). As it is ease to see, in each series the mean diameter varied as a power law of shellac mass fraction, $d \sim f_p^{iX}$, (straight line in the log-log plot). All the exponents are close to 1/3 (listed in table 4.1), indicating that the volume per particle is proportional to the concentration of polymer in the initial solution. However, as already reported for PMMA mixture by Aubry et *al* (2009) this trend can be true regardless of whether the dispersions were prepared in the Ouzo or non-Ouzo ranges. Moreover we found a slight (logarithmic) increase of the relative standard deviation calculated from the second cumulant according to eq. 4.7 (not shown), indicating a higher polidispersity of the nanoparticles and a possible transition between the Ouzo region and the nucleation and growth domain.

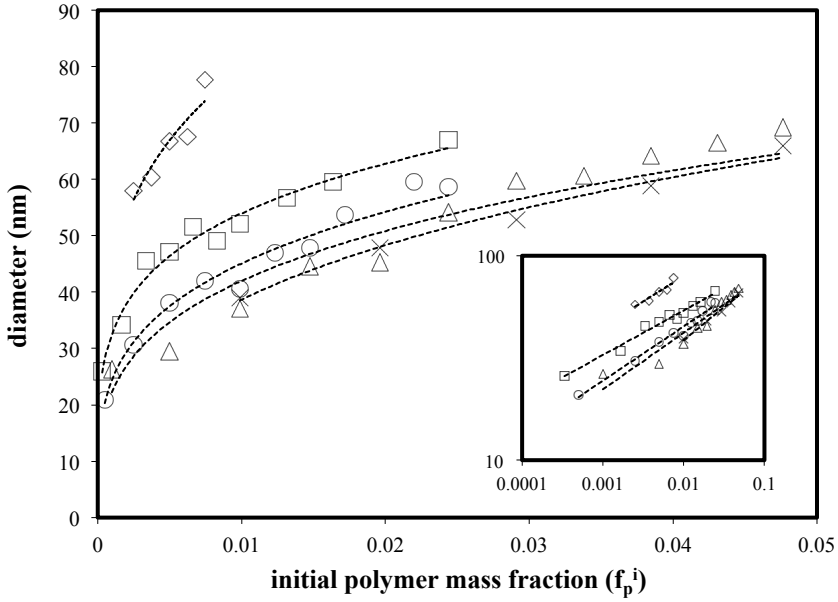

Figure 4.3 Main body: mean particle diameter as functions of the initial mass fraction of shellac in ethanol. Each set of data is for a different final mass fraction of solvent (cross 0.05, triangles 0.1, circles 0.2, squares 0.3, diamonds 0.4). Insect: calculated diameter in a double log plot, showing linearity.

SOLVENT FRACTION	SLOPE	R^2
0.4	0.25	0.91
0.3	0.22	0.95
0.2	0.29	0.95
0.1	0.39	0.99
0.05	0.32	0.98

Table 4.1 slope and best fit coefficient (r^2) obtained from fitting particle size vs initial polymer mass fraction (f_p^i) in log-log scale, for different solvent mass fraction (f_s)

4.3.3. Composition boundaries

Further insight the physical phenomenon governing the formation of nanoparticle can be given by the construction of the ternary phase diagram for shellac/ethanol/water system. Here, we choose to give the diagram in the representation proposed by Vitale and Kantz (2003), where composition are plotted according to the final mass fraction of shellac (horizontal axis) and the mass fraction of solvent (vertical axis). The mass fraction of polymer was so low that a log scale was adopted for x-axis. The equilibrium phase separation boundary of the ternary solutions (binodal line) was determined by titrating with water different solutions of shellac until a dramatic increase of the OD600 was observed (fig 4.4a). The Ouzo boundary was determined using filtration and light scattering. The ratio of the intensity of filtered dispersions to the intensity of raw dispersions (RI_s) was plotted as a function of the final mass fraction of polymer. An example is shown in fig. 4.4b for two samples with different solvent fraction. As expected RI_s is constant and closed to unity at low final mass fraction of shellac, indicating that such compositions were within the Ouzo range and that all particles passed through filters. For dispersion containing bigger particles that that were removed by filtration, the final polymer mass fraction was less than in the raw dispersion, and RI_s decreased.

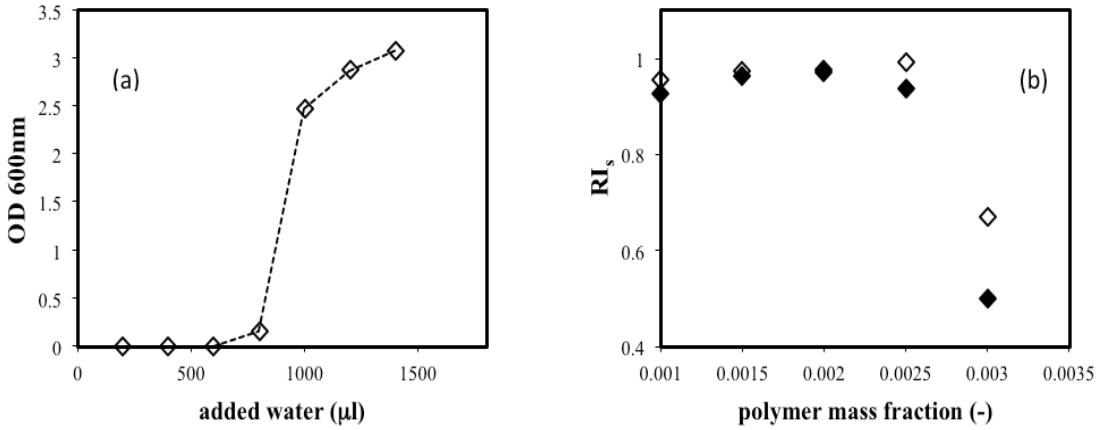

Figure 4.4 (a) Determination of binodal line using titration with water (e.g. 30mg/ml shellac solution) and (b) determination of Ouzo boundary using filtration to remove bigger particles (white circles: ethanol mass fraction 0.1; black diamond: ethanol mass fraction 0.2)

The main features of the obtained phase diagram can be well captured in the graph of fig. 4.5, showing the binodal line together with the Ouzo boundary for the shellac/ethanol/water system, and one important conclusion can be drawn: ouzo boundary goes to higher polymer concentration when the solvent quality get worse. Thus the formation of bigger particles or aggregates seems not to be related to spinodal decomposition.

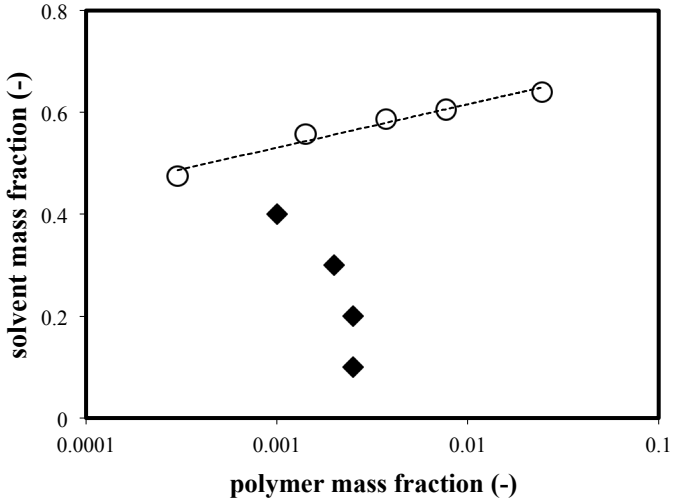

Figure 4.5 Composition boundaries for nanoprecipitation in the shellac/ethanol/water ternary system. White circles: binodal curve. Black diamond: points of the Ouzo boundary.

Moreover, by plotting the experimental points at the Ouzo boundary *versus* the initial rather than the final concentration of polymer as proposed by Stainmesse *et al* (1995), it clearly appears that the initial mass fraction of shellac decreases exponentially with the solvent/water ratio (fig. 4.6). In order to confirm the transition between the Ouzo region and the nucleation and growth domain of the ternary phase diagram, we performed some TEM experiments on two samples at the same mass fraction of solvent (i.e f_s = 0.3) taken before or right after the boundary conditions of fig. 4.5 (f_p = 0.001 and f_p =

0.0025). Fig. 4.7 clearly show that before the Ouzo limit only nanoparticles are produced, whereas at higher concentration of polymer bigger particles and aggregates are seen confirming the existence of a boundary condition for the production of homogeneous and monodisperse nanospheres.

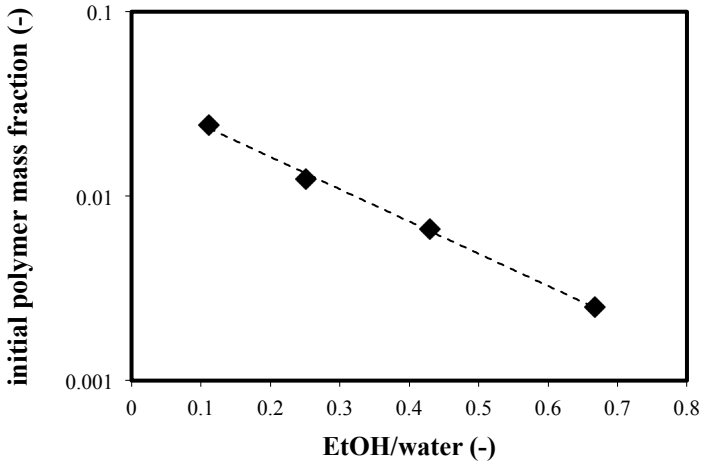

Figure 4.6 Ouzo boundary in the alternative representation, semi log plot. *X* axis: ratio between solvent and non-solvent. *Y* axis: mass fraction of polymer in the initial solution, before adding water

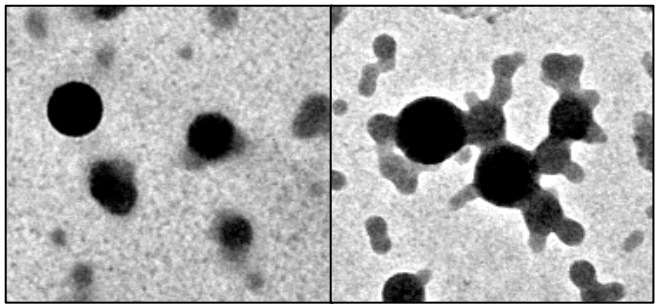

Figure 4.7 TEM photographs of nanoparticles of shellac synthesized in the Ouzo domain (a) and beyond the Ouzo boundary (b)

4.3.4. Depolarized dynamic light scattering

Considering the fact that the Ouzo boundary separates a region in which only nanoparticle are produced from a region of the ternary phase diagram where anisotropic aggregates are formed, we performed depolarize dynamic light scattering measurements (DDLS) measurements first to confirm the boundary points we found by using filtration and DLS.

If the particles are anisotropic in shape, upon irradiation with the polarized electric field of the incident laser beam, the oscillating Maxwell dipole associated with their shape will have a component orthogonal to the incident polarization plane. This will result in a measurable intensity on a detector with a polarizer oriented orthogonal to the incident electric field, resulting in the depolarized scattering intensity. In our experiment we measured the depolarized dynamic scattering intensity at different scattering angles for different dispersion produced at various concentrations of polymer and solvent. The depolarization ratio can be defined as

$$D_p = I_{VH}/I_{ISO} \qquad \textbf{(4.8)}$$

where, I_{VH} is the anisotropic contribution of scattering from a solution containing $<N>$ number of particles and is given by $I_{VH} = <N>(\beta^2/15)$ and the rotation independent isotropic contribution to scattered intensity (I_{ISO}) is $I_{ISO} = <N>\alpha^2$. The parameters $\alpha = (\alpha_{II}+2\alpha_{\perp})/3$ and $\beta = (\alpha_{II}-\alpha_{\perp})$, where the horizontal and perpendicular components of the polarizability are given as α_{II} and $\alpha_{\perp}$ respectively. It follows that

$$I_{VV} = I_{ISO} + (4/3)I_{VH} \qquad \textbf{(4.9)}$$

Since both I_{VV} and I_{VH} are measurable one can determine the depolarization ratio by using the above equations. (Berne and Pecora, 1976)

As an example, figure 4.8 displays D_p as a function of polymer mass fraction (f_p) for sample obtained at mass fraction of solvent equal to 0.1. These results indicate an exponential increase of D_p with increasing f_p. The above mentioned results pointed out that 0.0025 polymer mass fraction likely corresponds to the Ouzo limit, which in figure 4.8 is the first experimental point demonstrating a significantly high anisotropy (~0.5). In general, spherical particles do not exhibit signal in DDLS. This is the case for very low mass fraction of polymer. Increasing the mass fraction of polymer causes a rise in the intensity of the scattered light measured by depolarized dynamic light scattering, suggesting an increase in particle anisotropy. Above 0.0025 of polymer mass fraction, a dramatic enhance of I_{VH} could be explained by assuming formation of highly anisotropic aggregates. Incidentally, we found this concentration limit quite close to the Ouzo boundary determined by using filtration and DLS (see section 4.3.3).

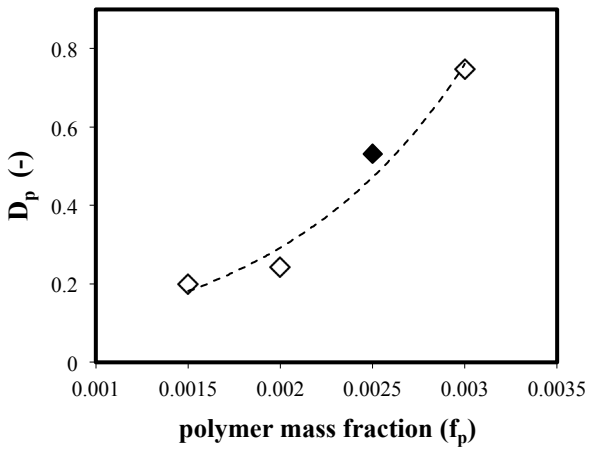

Figure 4.8 Depolarization ratio D_p as a function of the polymer mass fraction (f_p) for dispersion prepared at the same mass fraction of solvent (f_s=0.1). The black diamond corresponds to the first point for which an abrupt increase in the anisotropy is observed, incidentally corrisponding to the Ouzo boundary determined by filtration and polarized dynamic light scatterig.

Therefore, it is interesting to calculate the rotational diffusion coefficient (D_r) for this sample, as well as for the rest of the points located at the Ouzo boundary. Recalling basic theory, for dilute solution the intensity autocorrelation function $(g^2_{VH}-1)^{0.5}$ from DDLS can be written as the product of two discrete exponentially decaying functions, where the slow relaxation mode characterizes translational diffusion while the faster relaxation mode is related to rotational motion and shape fluctuations. Hence, one may

describe the experimental data in terms of a slow (Γ_{slow}) and a fast relaxation rate (Γ_{fast}) according to:

$$\Gamma_{slow}(q,a) = q^2 D_t(a) \qquad \textbf{(4.10)}$$

$$\Gamma_{fast}(q,a) = q^2 D_t(a) + 6D_r(a) \qquad \textbf{(4.11)}$$

being D_t, D_r and a are the translational diffusion coefficient, the rotational diffusion coefficient and the particle radius respectively. Thus, in a plot q^2 vs Γ, D_r can be obtained directly by an extrapolation at $q \to 0$. As an example, figure 4.9 shows the apparent decay rate vs q^2 at 0.1 f_s and 0.0025 shellac mass fraction, and the rotational diffusion coefficient Θ calculated from the intercept is 288 s^{-1}.

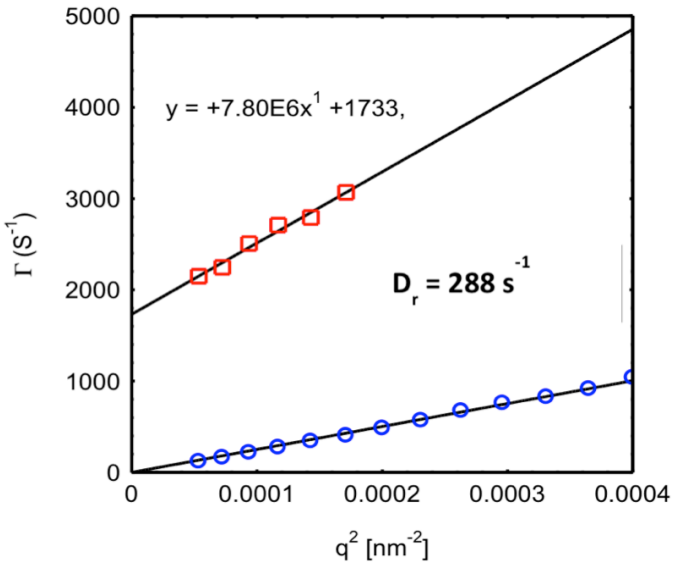

Figure 4.9 Decay rates Γ_{slow} (open circles) and Γ_{fast} (open squares) for nano-dispersion of shellac at the Ouzo boundary (solvent mass fraction 0.1, polymer mass fraction 0.0025)

Calculations of D_r have been performed for all the points at the Ouzo boundary and are here presented in figure 4.10, showing the rotational diffusion coefficient (D_r) on the x axis, the ratio between ethanol and water (f_s/f_w) on the left y axis and the initial mass fraction of polymer (f_p^i) on the right y axis (log-scale). As it is evident, the rotational diffusion coefficient is increasing roughly linearly with increasing the solvent/non solvent ratio. Thus, the better the solvent, the more spherical the particle are. On the contrary, D_r decreases exponentially whit-increasing f_p^i.

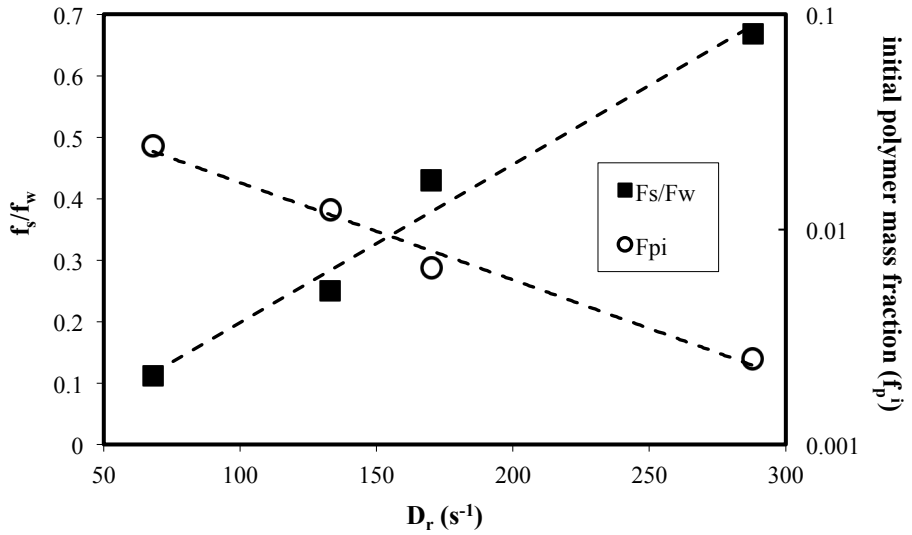

Figure 4.10 Rotational diffusion coefficient (D_r) as a function of the ratio between ethanol and water (f_s/f_w, black squares, left y axis) and of the initial polymer mass fraction (f_p^i, open circles, right y axis)

4.3.5. Future perspectives and preliminary application

The results here presented suggest that the Ouzo region can be well determined directly on the raw dispersion by using 3D depolarized dynamic light scattering. These boundaries separate a region of the phase diagram in which only nanoparticles are seen from another region where bigger aggregates appear. Nanoparticles seems to evolve through a *nucleation-and-aggregation* mechanism but the origin of the transition to the coalescence domain is not yet understood and therefore an *apriori* determination of Ouzo boundaries is not possible. The probability of coalescence could be related to the probability that a localized event such as a loss of surfactant (Exerowa *et al*, 1992) or a curvature inversion (Kabalnov and Wennerström, 1996) will take place somewhere in the surfactant film that separates the droplets. In our experiment we did not use any kind of surfactant during sample preparation. However since ethanol is miscible with water as well as with shellac, it might act as an emulsifier, which influences the dynamics of such systems (Scholten and van der Linden, 2008). Further insight the physical phenomenon governing the Ouzo effect can be obtained through the calculation of the aggregates rotational diffusion coefficient, which displays a well defined dependence on the ratio between solvent and non solvent as well as on the initial polymer mass fraction. A detailed discussion of these aspects, together with the calculation of the aggregates fractal number for the determination of the main mechanism governing particle aggregation (i.e. RLCA or DLCA) from static light scattering data, will be faced in future works.

The practical applications of the results obtained in this part of the thesis have been explored in a series of experiments. These preliminary experiments were aimed at studying the production of highly stable tocopherol (vitamin E) nanoparticles for food applications, by means of the spontaneous emulsification. Briefly, a solution of α-tocopherol in ethanol was mixed with water to a final mass fraction of the vitamin in the mixture of $f_V^f = 0.007$, according to the nanopreciption process already described. Mass fraction of solvent was $f_s = 0.2$. Due to solvent-shifting a spontaneous emulsion is obtained, in the same way as it occurs for shellac in the experiments above described. The vitamin concentration limits within which the Ouzo-effect is feasible were not determined, and we limited our analysis by assuming that at this very diluted concentration α-tocopherol can form spontaneous emulsion (Khayata *et al*, 2012). A second emulsion was obtained at the same vitamin concentrations,

in the presence of shellac at a given mass fraction (f_p^f = 0.0015). This value of concentration was chosen on the basis of the results presented in 4.3.3, i.e., the shellac concentration in the final mixture was such that production of spontaneous nanoparticle is possible.

The emulsion stability was assessed through centrifugation experiments. In this experiments the two emulsions were subjected to high-speed centrifugation (6300g) for different times (from 20 to 120 min). After removing the supernatant, containing mostly separated tocopherol, the vitamin E content of the emulsions was determined in the bulk by spectrophotometric measurements. Fig. 4.11 shows the percentage of tocopherol in the emulsions versus the centrifugation time. The results obtained clearly show an increase in the stability of the shellac-tocopherol emulsions compared to that of the emulsion done in absence of the polymer. Namely, after 20 min, the amount of tocopherol in the shellac-tocopherol emulsion was ≈ 3 times greater than the only-tocopherol one. This ratio does not change by increasing the centrifugation time. Further analyses are required to understand the polymer-vitamin interactions responsible for such an increase in the emulsion stability.

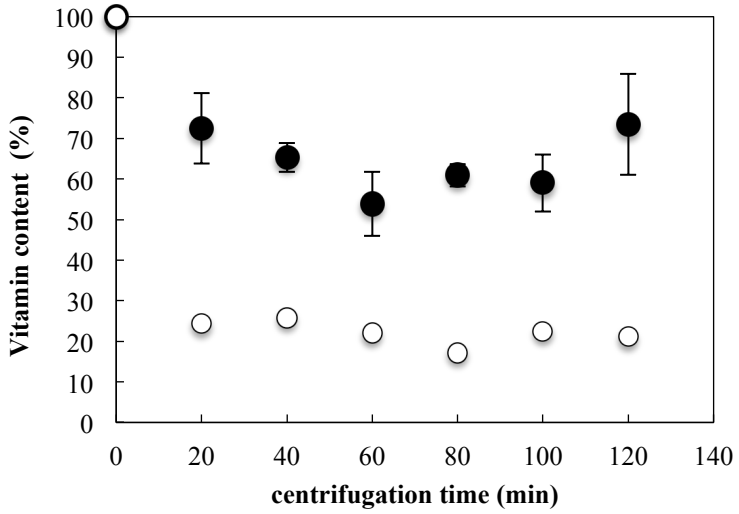

Figure 4.11 Percentage of vitamin E in emulsion after different centrifugation time at 6300g for tocopherol/shellac emulsion (filled circles) and tocopherol emulsion (empty circles)

4.4. REFERENCES

1. Antonietti M, Conrad J & Thunemann A, 1994, Polyelectrolyte-surfactant complexes—a new type of solid mesomorphous material. *Macromolecules* 27, 6007–6011
2. Aubry J, Ganachaud F, Cohen Addad JP, and Cabane B, 2009, Nanoprecipitation of Polymethylmethacrylate by Solvent Shifting: 1.Boundaries. Langmuir (25) 1970-1979.
3. Bally F, Garg DK, Serra CA, Hoarau Y, Anton N, Brochon C, ... & Hadziioannou G., 2012, Improved size-tunable preparation of polymeric nanoparticles by microfluidic nanoprecipitation. *Polymer*.
4. Beck-Broichsitter M, Rytting E, Lebhardt T, Wang X, Kissel T, 2010, Preparation of nanoparticles by solvent displacement for drug delivery: a shift in the "ouzo region" upon drug loading. European Journal of Pharmaceutical Sciences, (41) 244–253.
5. Berne BJ and Pecora R, 1976, Dynamic light scattering. New York Wiley.
6. Bolisetty S, Hoffmanna M, Lekkalaa S, Hellwega Th, Ballauffa M and Harnau L, 2009, Coupling of Rotational Motion with Shape Fluctuations of Core-shell Microgels Having Tunable Softness. Cond-mat.soft, 1-9.
7. Botet R, 2012, The "ouzo effect", recent developments and application to therapeutic drug carrying. Journal of Physics: Conference Series 352 , 012047.
8. Carteau D, Pianet I, Brunerie P, Guillemat B, Bassani DM, 2007, Probing the initial events in the spontaneous emulsification of trans-anethole using dynamic NMR spectroscopy. Langmuir 23(7), 3561–3565.
9. Chu B, 1991. Laser Light Scattering 2e: Basic Principles and Practice. Access Online via Elsevier.
10. Dirksen JA, & Ring TA, 1991, Fundamentals of crystallization: kinetic effects on particle size distributions and morphology. Chemical Engineering Science, 46(10), 2389-2427.
11. Exerowa D, Kashchiev D, & Platikanov D, 1992, Stability and permeability of amphiphile bilayers. Advances in colloid and interface science, 40, 201-256.
12. Ganachaud F and Katz JL, 2005, Nanoparticles and Nanocapsules Created Using the Ouzo Effect: Spontaneous Emulsification as an Alternative to Ultrasonic and High-Shear Devices. ChemPhysChem (6): 209 – 216.
13. Grillo I, 2003, Small-angle neutron scattering study of a world-wide known emulsion: Le Pastis. Colloid Surf., A 225:153–160.
14. Ikkala O & ten Brinke G, 2002, Functional materials based on self-assembly of polymeric supramolecules. *Science* 295:2407–2409
15. Jones RAL 2002 Soft Condensed Matter Oxford University Press
16. Kabalnov A, & Wennerström H, 1996, Macroemulsion stability: The oriented wedge theory revisited. Langmuir, 12(2), 276-292.
17. Khayata N, Abdelwahed W, Chehna MF, Charcosset C, & Fessi H, 2012, Preparation of vitamin E loaded nanocapsules by the nanoprecipitation method: From laboratory scale to large scale using a membrane contactor. International Journal of Pharmaceutics, 423(2), 419-427.
18. LaVan DA, McGuire T & Langer R, 2003, Small-scale systems for in vivo drug delivery. Nature biotechnology, 21(10), 1184-1191.
19. Maret G, 1997, Diffusing-wave spectroscopy. Curr Opin Colloid Interface Sci, (2):251-257.
20. Mezzenga R, Schurtenberger P, Burbidge A and Michel M, 2005. Understanding foods as soft materials. Nat. Mater., 4: 729–740
21. Mitri K, Vauthier, C, Huang, N, Menas A, Ringard-Lefebvre C, Anselmi C, ... & Bouchemal, K, 2012, Scale-up of nanoemulsion produced by emulsification and solvent diffusion. Journal of pharmaceutical sciences, 101(11), 4240-4247.
22. Mora-Huertas CE, Fessi H and Elaissari A, 2011, Influence of process and formulation parameters on the formation of submicron particles by solvent displacement and emulsification–diffusion methods critical comparison. Adv. in Colloid and Interface Sci., (163):

90–122

23. Mosqueira VCF, Legrand P, Pinto-Alphandary H, Puisieux F, & Barratt G, 2000, Poly (D, L-lactide) nanocapsules prepared by a solvent displacement process: Influence of the composition on physicochemical and structural properties. Journal of pharmaceutical sciences 89(5) 614-626.
24. Nisha Pawar, Bohidar HB, 2011, Anisotropic domain growth and complex coacervation in nanoclay-polyelectrolyte solutions. Advances in Colloid and Interface Science, (167):12–23.
25. Noriega-Peláez EK, Mendoza-Muñoz N, Ganem-Quintanar A, & Quintanar-Guerrero D, 2011, Optimization of the emulsification and solvent displacement method for the preparation of solid lipid nanoparticles. Drug Development and Industrial Pharmacy, 37(2), 160-166.
26. Nowakowska J, 1939, The Refractive Indices of Ethyl Alcohol and Water Mixtures. Master's Theses. Paper 668
27. Pecora R, 1985, Dynamic light scattering: applications of photon correlation spectroscopy. Springer, 985:1985.
28. Pusey PN, 1999, Suppression of multiple scattering by photon cross-correlation techniques. Current Opinion in Colloid & Interface Science (4) 177-185.
29. Scholten E, van der Linden E, This H, 2008, The life of an anise-flavored alcoholic beverage: Does its stability cloud or confirm theory?. *Langmuir* (*24*):1701–1706.
30. Sitnikova NL, Sprik R and Wegdam G, 2005, Spontaneously Formed trans-Anethol/Water/Alcohol Emulsions: Mechanism of Formation and Stability. Langmuir (21): 7083-7089.
31. Stainmesse S, Orecchioni A-M, Nakache E, Puisieux F, Fessi H, 1995, Formation and stabilization of a biodegradable polymeric colloidal suspension of nanoparticles. *Colloid Polym. Sci.* (*273)*: 505–511.
32. Vitale SA and Katz JL, 2003, Liquid Droplet Dispersions Formed by Homogeneous Liquid-Liquid Nucleation: “The Ouzo Effect”. Langmuir (199) 4105-4110.

5. CONCLUSION

5 CONCLUSION

Designing and developing new functional food ingredients suitable to deliver a specific functionality during digestion represent one of the most interesting and promising perspectives in the field of food science. An engineering approach to food structure design for the delivering of tailor-made functionality in the manufacturing of bioactive carriers has been developed in the thesis. Micro- and nano-capsules containing a bioactive have been created with optimized functionality and targeted release within the body to maximize its health benefits. An innovative approach has been followed that explores the relationship: material properties-processing-destructurization behavior in the gut. This approach consists in the process engineering for food properties generation, preservation and delivery, relying on the concepts of multiscale structure dynamics and on biophysics-driven strategies for structure design. In this framework, a soft matter approach, integrated in the more general concept of tailor made food, can provide real benefits in understanding food materials structure design at multiple length scales.

In this thesis, we first presented a detailed study of the dynamics of alginate gels, a natural polymer extensively used in the food industry as thickening agent. Our results show that alginate networks, share many features in common with physical colloidal gels. Specifically, the gel displays a complex aging behavior, characterized by a strongly heterogeneous microscopic dynamics involving both local rearrangements persisting over very long time, and collective restructuring effects evidenced by sudden decorrelation bursts. A basic investigation of the macroscopic mechanical response of the gel, both as a function of the applied strain and as a function of deformation time, supports the basic picture derived from the investigation of the microscopic dynamics. In particular, the slow creeping behavior of the gel observed after a burst rapid stress relaxation, which can be attributed to the concurrence of many superpositions of local relaxation modes yielding an overall stretched exponential decay, is consistent with the persistence of a local microscopic diffusive dynamics over long times and with the occurrence of intermittent global rearrangements.

Due to the resulting network arrangement, gels obtained from alginate are suitable to be used as wall material for the production of novel food structures, which are intended as vehicles for controlled release of the carried substance. An aqueous core, enclosed by a well-defined external alginate shell, can be obtained by coextruding the two phases in a concentric laminar flow column, splitting the latter into drops by a mechanical rupturing by the blades of a rapidly rotating fan, and suddenly gelling the external polymer phase before interdiffusion with the internal phase takes place. In the same way alginate microbeads containing a hydrophobic core can be obtained: however, due to differences in surface tension and viscosity with respect to alginate, the nature of the filler phase influences the break up length of the liquid jet exiting the co-extrusion nozzle, requiring the optimization of some key process parameters as a function of the hydrophobicity of the core material. Our results clearly demonstrated the possibility to produce spherical alginate microcapsules with a narrow size distribution and containing either hydrophobic or hydrophilic core. A preliminary quantification of the diffusional behavior of a small hydrophilic vitamin from alginate microbeads shows a good retention of molecule in water at ambient temperature.

The in vitro evaluation of the biophysics aspects of bioactive delivery from the beads, which were manufactured throughout the coextrusion technique, has been successfully investigated by using an *in vitro* simulated small intestine model, which enable analysis of the phenomena occurring in the intestinal tract from an engineering perspective. Alginate microbeads, once subjected at chemical and physical conditions which mimic the human gut, retain their functionality and slowly release the carried bioactive, whereas a burst release is observed in simulated gastric environment. The release at high pH can be modulated by applying an appropriate double coating to the primary shell but unfortunately does not affect the diffusion at low pH. However, alginate microbeads coated with chitosan can be effectively used to protect the viability of encapsulated probiotic from the gastric environment, as clearly demonstrated by luminometric measurements on a modified bioluminescent *Bifidobacterium longum*.

Conclusion

Complex functional ingredient able to respond to stimuli such as pH or temperature can be heterogeneous and designed at multiple length scales. At the smallest length scale, formation of nanoparticles by solvent shifting is a really attractive process: it is spontaneous, mild, reproducible and gives rise to controlled monodisperse emulsion. In this work, we studied the ternary phase diagram for a totally food grade polymer/solvent/non solvent system and we identified the concentration limits for the production of monodisperse nanospheres. Depolarized dynamic light scattering suggest that the transition between the ouzo region and the nucleation and growth domain, where the probability of coalescence increases and larger particle are seen, should be attributed to the loss of particle isotropy with increasing polymer mass fraction.

The main scientific achievements of the thesis may help to cross the bridge toward designed food structuring from a food-engineering and physical–chemical perspective. In the frame of the gastrointestinal investigations a huge amount of further research is still need, due to the non-equilibrium nature of food structure in general and under transient de-structuring conditions of the gastrointestinal tract. Bioactive encapsulation performed under the property-structure-process relationships seems to be a promising way to deliver new products that are healthy.

APPENDIX 1: LIST OF PAPER, ORAL COMMUNICATIONS AND POSTERS

1. Munarin F, Petrini P, Barcellona G, Roversi T, Piazza L, Visai L, Tanzi MC, 2013. Reactive hydroxyapatite fillers for pectin biocomposites. Submitted to Macromolecular Bioscience
2. Piazza L, Roversi T, 2011. Preliminary study on microbeads production by co-extrusion technology. Procedia Food Science 1:1374-1380.
3. Secchi E, Roversi T, Buzzaccaro S, Piazza L, Piazza R, 2012. Biopolymer gels with physical cross-link: gelation kinetics, aging, heterogeneous dynamics, and macroscopic mechanical properties. Soft Matter 9:3931-3944
4. Turroni F, Serafini F, Foroni E, Duranti S, O'Connell Motherway M, Taverniti V, Mangifesta M, Milani C, Viappiani A, Roversi T, Sanchez B, Santoni A, Gioiosa L, Ferrarini A, Delledonne M, Margolles A, Piazza L, Palanza P, Bolchi A, Guglielmetti S, van Sinderen D, Ventura M, 2013. Role of sortase-dependent pili of Bifidobacterium bifidum PRL2010 in modulating bacterium-host interactions. PNAS 110(27)
5. Piazza L, Guglielmetti S, Roversi T, Valsecchi L, 2012. Functional structure processing by co-extrusion in the production of probiotics-enriched microbeads. Proceedings CeFOOD, NoviSad 23-26 May 2012, pp.28
6. Piazza L, Roversi T, 2011. Co-extruded alginate hydrogel beads as cyanocobalamin delivery system. Poster presentation at EFFOST meeting, Berlin, 9-11 November 2011.
7. Roversi T, Hari B, Bakalis S, Piazza L 2012 Flow Induced Delivery Of Healthy Food Function In A Simulated Model Of Small Intestine: Preliminary Evaluation Of Microencapsulated Vitamin B12 Release. Poster presentation at EFFoST meeting, Montpellier 20-23 Nov. 2012
8. Secchi E, Roversi T, Buzzaccaro S, Piazza L, Piazza R, 2012. Gelation kinetics and mechanical properties of alginate, a natural biopolymer for microfluidic encapsulation. Poster presentation at EFFoST meeting, Montpellier 20-23 Nov. 2012
9. Stucchi F, Roversi T, Ferrante A, Piazza L, 2013. Study of aging phenomena and rheological behaviour of cell wall polysaccharides extracted from fresh cut salad. Poster presentation at Biopolymers, Nantes 4-6 December 2013
10. Bertini S, Eisele G, Paganini D, Torri G, Piazza L, Roversi T, Mauri M, and Mauri L, 2010. Agar gels characterization by TDNMR and Rheology measurements. Atti del XII Convegno-Scuola sulla chimica dei carboidrati, 20-23 Giugno 2010, Certosa di Pontignano, Siena; Servizio Editoriale Universitario, Pisa, p.OC 16.
11. Roversi T, 2011. Design and development of tailor made microcapsules for bioactive controlled release. In Proc.s of the 16th Workshop on the Developments in the Italian PhD Research on Food Science, Technology and Biotechnology, Lodi (Italy), 21-23 September, 2011, pp. 357-358.
12. Roversi T, 2012. Delivery behaviour in simulate model of small intestine of coextruded alginate microbeads as carrier for vitamin B12. In Proc.s of the 17th Workshop on the Developments in the Italian PhD Research on Food Science, Technology and Biotechnology, Cesena (Italy), 19-21 September, 2012
13. Roversi T, 2013. Gelazione e caratteristiche strutturali di gel di alginato valutati mediante tecniche reologiche a grandi deformazioni, Oral presentation at Caratterizzazione di Idrogel, TA instruments, 22 aprile 2013
14. Roversi T, 2013. Material engineering for delivery of food functionality. In Proc.s of the 18th Workshop on the Developments in the Italian PhD Research on Food Science, Technology and Biotechnology, Conegliano (Italy), 25-27 September, 2013.